

Generalization of Particle Impact Behavior in Gas Turbine via Non-Dimensional Grouping

Alessio Suman^{1,a,*}, Nicola Casari^{1,b}, Elettra Fabbri^{1,c}, Luca di Mare^{2,d}, Francesco Montomoli^{3,e}, Michele Pinelli^{1,f}

¹ Dipartimento di Ingegneria, Università degli Studi di Ferrara, Ferrara, Italy

² St John's College, University of Oxford, St Giles, Oxford, United Kingdom, OX1 3JP

³ Imperial College London, London, SW7 2AZ

^a alessio.suman@unife.it, ^b nicola.casari@unife.it, ^c elettra.fabbri@unife.it, ^d luca.dimare@eng.ox.ac.uk, ^e f.montomoli@imperial.ac.uk, ^f michele.pinelli@unife.it

ABSTRACT

Fouling in gas turbines is caused by airborne contaminants which, under certain conditions, adhere to aerodynamic surfaces upon impact. The growth of solid deposits causes geometric modifications of the blades in terms of both mean shape and roughness level. The consequences of particle deposition range from performance deterioration to life reduction to complete loss of power.

Due to the importance of the phenomenon, several methods to model particle sticking have been proposed in literature. Most models are based on the idea of a sticking probability, defined as the likelihood a particle has to stick to a surface upon impact. Other models investigate the phenomenon from a deterministic point of view by calculating the energy available before and after the impact. The nature of the materials encountered within this environment does not lend itself to a very precise characterization, consequently, it is difficult to establish the limits of validity of sticking models based on field data or even laboratory scale experiments. As a result, predicting the growth of solid deposits in gas turbines is still a task fraught with difficulty.

In this work, two non-dimensional parameters are defined to describe the interaction between incident particles and a substrate, with particular reference to sticking behavior in a gas turbine. In the first part of the work, historical experimental data on particle adhesion under gas turbine-like conditions are analyzed by means of relevant dimensional quantities (e.g. particle viscosity, surface tension, and kinetic energy). After a dimensional analysis, the data then are classified using non-dimensional groups and a universal threshold for the transition from erosion to deposition and from fragmentation to splashing based on particle properties and impact conditions is identified. The relation between particle kinetic energy/surface energy and the particle temperature normalized by the softening temperature represents the original non-dimensional groups able to represent a basis of a promising adhesion criterion.

Keywords: *gas turbine; particle adhesion; erosion; splashing; non-dimensional group; particle-substrate interaction*

INDEX

1. Introduction
 - 1.1 Contributions
2. Particle sticking mechanisms and models
 - 2.1 Particle sticking models
 - 2.1.1 Critical viscosity method
 - 2.1.2 Critical velocity method
 - 2.1.3 Energy-based model
 - 2.1.4 Predictive sticking models
 - 2.2 Predictive models for particle properties
 - 2.2.1 Particle viscosity models
 - 2.2.2 Particle softening model
 - 2.2.3 Particle surface tension model
 - 2.2.4 Particle density model
3. Experimental data of gas turbine particle deposition
4. Literature data collection
 - 4.1 Experimental test conditions
 - 4.2 Experimental uncertainties
 - 4.3 Chemical composition
 - 4.4 Particle size, temperature and mineral/glass ratio
5. Particle sticking models and viscosity methods: mutual interaction and critical analysis
 - 5.1 Particle viscosity: quantification and model application
 - 5.2 Particle velocity: application of the critical velocity method
 - 5.3 Energy-based model: particle spread factor and overall comparison
 - 5.3.1 Particle surface tension
 - 5.3.2 Particle spread factor analysis

* Corresponding Author

56	5.3.3 Spread factor values
57	5.4 Comparison between critical viscosity and energy-based sticking models
58	5.4.1 Influences of particle composition
59	5.4.2 Critical analysis of the viscosity models
60	6. Dimensional analysis
61	7. Generalization of the particle impact behavior
62	8. Remarks
63	8.1 Limitations and perspectives
64	9. Conclusions
65	References
66	Appendix A
67	A.1 NPL Model
68	A.2 Modified silica ratio model
69	A.3 Slope and intercept model
70	A.4 Urbain's model
71	A.5 RRLG Model
72	A.6 SDS model
73	A.7 GRD model
74	Appendix B
75	Appendix C
76	Appendix D

1. INTRODUCTION

Gas turbines never operate in perfectly clean air. Land-based and offshore units ingest salt and particulate present in the atmosphere at low altitudes. Aircraft engines ingest large amounts of sand during operation in desert environments, or during flight through volcanic ash clouds. Solid particles can also make their way inside a gas turbine through the fuel, e.g. as coal fly ash in units burning pulverized coal. The effect of solid particles on gas turbine components is twofold: the particles can erode the blade surfaces or they can stick to them. In both cases the impact on performance and operability is negative.

The behavior of solid particles impinging on a wall is determined by the flow conditions, properties of the particles and by the temperature. As demonstrated in [1], particle adhesion is not a linear phenomenon for which several contributions affect the final results of particle impact at the same time. Depending on the material, temperature and impact conditions (related to both particle and substrate) the adhesion or rebound is not easily extrapolated by using similar experimental tests or numerical models. Starting from the result collection reported in [1], in the coal combustion field of research, many efforts have been made in estimating and improving the comprehension of deposition and slagging. Material characterization, experimental procedure, and, sometimes, equations model and basic criteria can be borrowed from this research field to the gas turbine field. Starting from these findings, two main conclusions can be drawn. At low temperature, the particles are likely to bounce off the wall and cause damage by erosion. At high temperatures, the particles become soft and can stick to the wall. As a consequence, erosion is the dominant damage mechanism in fans and compressors or in turbines operating at low Turbine Entering Temperature (TET). In this case, the damage is irreversible and is related due to an increase in roughness and to uncontrolled modifications of the shape of the blades, typically around the leading edges. Adhesion is the primary damage mechanism at high temperature and takes place mainly around the first turbine stage in machines operating at high TET – where gas and wall temperature values are the highest. Therefore, surface modification afflicts all parts of a gas turbine: coated and uncoated, cooled and uncooled surfaces all experience shape and surface modification from the baseline [2].

Contaminants are able to stick to blade surfaces in very different ways. The deposits can contaminate multiple stages of the machinery as a consequence of the different type, nature, and path of a single particle. Several experiments are reported in the literature concerning the deposition to hot components. Particle adhesion to hot parts has a number of adverse effects on the operation of the gas turbine. Solid deposits can incapacitate cooling holes – or entire cooling passages if the particles are carried by the cooling air itself – leading to reductions in component life [3]. Furthermore, solid deposits modify the effective shape of the airfoils, their roughness and, most crucially, the capacity of the nozzle vanes. When the capacity of the nozzle vanes is reduced, the compression system is moved to a higher working line and can eventually stall, leading to interruption of power.

Land-based turbines are usually exposed to relatively low concentrations of contaminants over long periods of time and can be protected by suitably designed filters. The main impact on land-based turbines of solid particles in the air or in the fuel impact is normally represented by the loss of performance – permanent or reversible [4], [5], [6], and [7]. Filters cannot be used in aeronautical applications – except in the smallest units. In aircraft engines, damage usually appears through erosion in the compressor and fouling in the turbine. It is known that erosion damage progresses rather slowly whereas fouling in the turbine can lead to loss of power in a matter of seconds, as reported in several encounters with volcanic ash clouds [8], [9] and [10]. A formalization of these phenomena is reported in [11] which define a predictive model for estimating the engine susceptibility to volcanic ash by means of several parameters related to the

sticking and shedding phenomena.

In Figure 1, an example of the turbine section contamination due to different sources is reported. As mentioned, land-based gas turbines are well protected by the filtration system, but, in the case of low-grade fuel operation, the contamination of the first turbine nozzle represents one of the primary causes of the performance losses. In this sense, Figure 1a reports a first nozzle contamination [12] that involves the entire blade surface as well as the cooling holes. Regarding the aircraft engine contamination, the volcanic ash particles affect the turbine nozzles as reported in Figure 1b [9]. The deposits appear more localized with respect to the previous example, but at the same time, these deposits are characterized by a higher hardness due to the solidification process of the semi-molten particles.

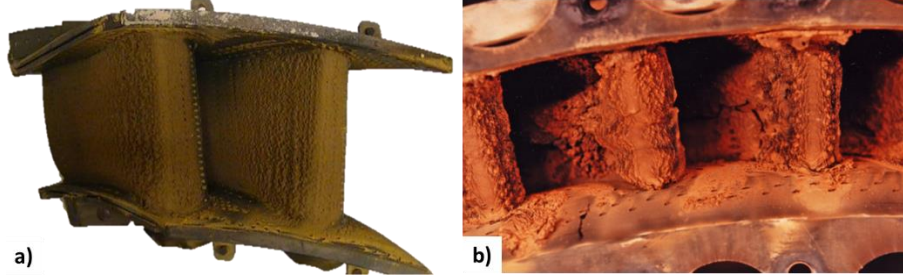


Figure 1 - Gas turbine nozzle contamination: a) land-based power unit in which the contaminants are due to the operation with low-grade fuels (sub-bituminous ash derived from coal mined) [12], and ii) aero engine contamination due to volcanic ash particle [9].

Particle deposition on gas turbine components has attracted much attention because of its practical implications and a large number of experimental studies is available [13] and [14]. These studies cover the whole range of conditions of (i) full scale gas turbine unit, (ii) wind tunnel testing or hot gas facilities using stationary cascades, able to reproduce the same conditions of gas turbine operation and finally, (iii) wind tunnel testing or hot gas facilities using coupon as a particles target. The experimental analyses have been supported by - and have given inspiration to - increasingly realistic mathematical models. These models are widely used in the computational fluid dynamic analysis for the study of this phenomenon.

Two types of model exist according to the approach followed to describe particle sticking. The first model type relies on the definition of a quantity called sticking probability. The sticking probability represents the likelihood a particle has to stick to a substrate (clean surface or pre-deposited layer). This probabilistic approach is required to overcome inaccuracy and the uncertainty of the experimental tests on which these models are based. The sticking probability value may be regarded as the statistically representative outcome of a series of independent experiments carried out under the same conditions. For example, turbulent phenomena may afflict the particle dynamic changing the impact velocity which could assume a different value for every single impact for the same test conditions. In addition, the definition of a probability function may consider the actual variation experienced by the gas turbine in terms of particle size and shape, material compositions, operating conditions and conditions of the blade surface that are difficult-to-be-considered in the laboratory tests.

The second model type is related to the comparison of the properties of a particle and a threshold value which considers the particle dynamics, its material properties and energy available before and after the impact. This deterministic approach can only be used when the conditions of the flow, the substrate and the particles are known in detail.

The validity of the available models could be assessed, in principle, by applying them to the wealth of experimental data published on particle deposition. However, these data cover a very wide range of flow velocities, temperatures, particle materials, and target surfaces. Therefore, they cannot easily be grouped or compared to each other unless suitable non-dimensional quantities are defined. Non-dimensional maps and non-dimensional correlations which describe the behavior of molten or liquid particles are available in literature [15 – 19] and can be used with advantage to study the problem at hand because the solid particles ingested in a gas turbine are heated by the combustor and are thereby softened or completely molten before hitting the walls of the turbine.

From a physical point of view, the conditions for adhesion, rebound or break-up are determined by how much of the initial kinetic energy of the particle is absorbed by the deformation work upon impact and by the adhesion energy with the substrate and how much is still available to remove the particle, or its fragments, from the wall. In addition to these forces, also the surface tension interacts with the particle deformation, and the resulting surface energy is a function of the contact area between the particle and the substrate [15] which is directly related to the particle deformation. These relations are conveniently expressed in terms of the particle Weber, Reynolds and Ohnesorge numbers

$$We = \frac{\rho v^2 d}{\gamma} \text{ where } \rho, \gamma = f(T) \quad (1)$$

$$Re = \frac{\rho v d}{\mu} \text{ where } \rho, \mu = f(T) \quad (2)$$

$$Z = \sqrt{We}/Re \quad (3)$$

where the density ρ , normal impact velocity v , diameter d , surface tension γ , and viscosity μ represent the particle properties and motion prior to the impact [16]. Both the Reynolds and Weber numbers change with temperature because of the temperature dependence of viscosity, surface tension and, to a lesser extent, density.

Using non-dimensional parameters, generalized maps can be formed showing different regimes – stick, rebound, spread, break up, splash - for the interaction between sprays and heated walls [17]. Moreover, it is possible to predict the droplet behaviors like stick, rebound, spread, break-up and splash in terms of only two parameters, one non-dimensional (Weber number) and one dimensional (wall temperature). A similar approach has been adopted to describe the performance of droplets deposition for printing [18]. In this case, by using two non-dimensional parameters (Weber number and Reynolds number), it has been possible to define whether ink droplets splash or not during printing [19].

1.1. Contributions

The aim of the present work is to identify particle deposition regimes in the hot parts of gas turbines in terms of non-dimensional quantities. To this effect, over 70 particle deposition tests reported in the literature are studied. The collected tests are selected because they were conducted using similar materials (silica-based type contaminants, such as silty, coal-like, and volcanic particles) and took place in conditions relevant to deposition on the hot parts of gas turbines. The tests were carried out in a number of configurations, covering full engines, single blades, coupons or blade cooling channels. The tests provide particle sticking results as a function of particle velocity, temperature, dimensions, etc. Only in a few cases, the sticking phenomenon is reported in detail with the quantitative estimation of mass deposits determining the per-order-of-magnitude approach adopted in the present work.

Details about particle size and chemical composition used in each experimental test are listed as well as the flow conditions such as velocity and temperature values. In addition, the target typology and its dimension are reported (if available in the literature) in order to characterize each impact test. Starting from this collection, a critical post-process is carried out by means of dimensional (e.g. particle kinetic energy, temperature, etc.) and non-dimensional groups (e.g. particle Reynolds number, particle Weber number, etc.). With more details, the first part of the present review paper includes the following points:

- collection and comparison of the literature on experimental particle impact tests related to gas turbine fouling;
- application of the most used particle sticking models for gas turbine particle adhesion, highlighting how each model works and where it fails if compared with the actual test results;
- a detailed review of the predictive model for particle viscosity is added and a sensitivity analysis coupling particle characteristics (e.g. chemical composition) and impact conditions (e.g. temperature) with the experimental results is proposed in order to highlight the implications of the use of different sticking models together with particle viscosity models.

In the second part, an innovative approach gives the opportunity to link the present experimental results with some new perspective. The phenomenology reported in literature dating back 30 years is summarized in terms of two non-dimensional parameters representing the ratio between the particle temperature and the glass transition temperature on one hand, and the ratio between the available kinetic energy and the surface energy on the other hand. The non-dimensional map clearly shows a number of different regimes, fitting very well with reported observations in terms of deposition and erosion phenomena. Furthermore, the map shows that the phenomena taking place in gas turbines are amenable to generalizations in different fields of research (e.g. printable fluids). The non-dimensional map proposed by the Authors represents a prediction tool in relation to the particle deposition and erosion phenomena and give a new insight into the gas turbine fouling prediction. The conceptual steps, as well as the overall scenario in which the present work is developed, are reported diagrammatically in Figure 2.

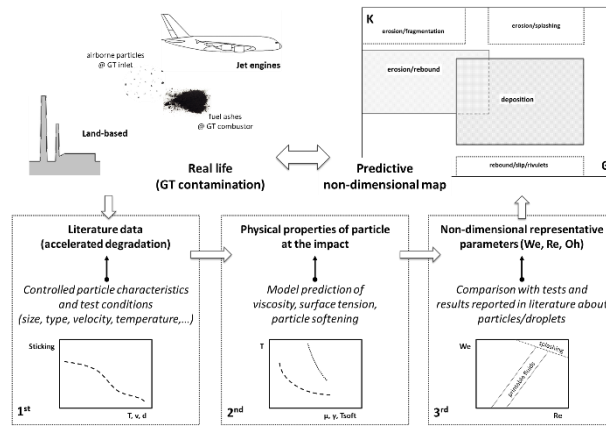


Figure 2 – Conceptual framework: the predictive model of real-life behavior is based on non-dimensional parameters achieved by specifically-designed tests

2. PARTICLE STICKING MECHANISMS AND MODELS

The adhesion of contaminant particles to the blade surfaces is determined by (i) the material of the interacting bodies (particle, surface, third substance and carrying medium), (ii) the surface conditions, (iii) the particle size, (iv) the impact velocity and (v) the impact angle. The conditions under which these contaminants stick to blade surface are still unclear. Over the years, several contributions related to the fouling phenomenon have been proposed and this paragraph aims to summarize the models describing the particle sticking. Three particle sticking models have been considered for the data post-process, which is mainly referred to as the basic criteria, such as particle viscosity, velocity, and energy. Other formulations which are derived from these basic criteria are listed as well, but they are not considered for the data-process.

The present section reports in detail (i) the sticking models used for predicting particle adhesion on hot gas turbine sections and (ii) the predictive models for estimating particle characteristics (viscosity, surface tension and softening).

2.1. Particle sticking models

2.1.1. Critical viscosity model

This model, widely used in the literature, compares particle viscosity to a reference viscosity at which sticking starts. In addition, the model could account for the stickiness of the deposit itself [20]. The sticking probability was assumed to be inversely proportional to viscosity. In terms of sticking probability, viscosity at or below the critical viscosity is assumed to have a sticking probability of unity whereas at other particle temperature, according to the relation

$$P_{\text{visc}} = \mu_c / \mu \quad (4)$$

$$P_{\text{visc}} = \begin{cases} \mu_c / \mu & \mu > \mu_c \\ 1 & \mu \leq \mu_c \end{cases} \quad (5)$$

where P_{visc} is the sticking probability related to the viscosity effect and μ_c is the particle critical viscosity while μ is the viscosity of the particle at its temperature. This model is implemented assuming that the critical viscosity value corresponds to the particle viscosity at the softening temperature (μ_{soft}). Softening temperature is a predetermined temperature value, and it is a function of the particle material that could be calculated/measured according to the standard ASTM – D1857-04 (*Standard test method for fusibility of coal and coke ash*) [21]. This standard definition allows a univocal and reproducible application of the critical viscosity method.

Many authors have applied this method and, in some cases, validated its results with experimental tests [22], [23], [24], [25], [26], [27]. Other contributions have improved the model by introducing a transition across the critical viscosity value [22], and by extending its validity at a lower temperature (lower compared to the melting temperature) [28]. A detailed explanation of these models can be found in the paragraph *Predictive models for particle properties* of the present Chapter.

At a lower temperature, energy losses due to particle-surface impact will determine whether an impacting particle will be able to leave the surface. These energy losses are a function of impact parameters such as the properties of the particle, impact velocity and angle. This last formulation of the model states the probability of sticking should be a function of energy losses during a collision and is calculated from the coefficient of restitution model as

$$P_e = f(e) = e^{-c R} \quad (6)$$

The coefficient of restitution R is therefore considered as an index of the energy dissipated at the impact: the lower it is the higher the dissipative viscous effect of the impact. Its effect is accounted for through an exponential law where the coefficient $c \sim 6.5$. Since the model for the sticking must still depend on the viscosity of the particle (with respect to μ_{soft} considered as the threshold for ideal adhesion), the final formulation of this model is the one reported below:

$$P = \min(P_e + P_{\text{visc}}, 1) \quad (7)$$

Another formulation is related to the definition of the critical value of the viscosity, which could relate the effects of particle softening with the particle kinetic energy. In this case, the definition of the critical viscosity is the following

$$\mu_c = A E_{\text{kin}}^B \quad (8)$$

where A and B are two coefficients able to fit the experimental results related to the specific material. For example, in the case of glass particles [29], $A=5 \cdot 10^{-12}$ and $B=-1.78$.

This model is strongly dependent on the particle material composition. Low-melting elements or mixtures could be responsible for early particle adhesion. For this reason, this model is only suitable when the characterization of the material particle and its behavior according to the temperature is available.

2.1.2. Critical velocity method

This model is based on the comparison between a threshold value of velocity and the particle velocity [30]. Other contributions are related to the representation of the particle-boundary layer interaction. Numerical studies on the interaction between the particle and boundary layers are reported in the literature [31], with greater attention to the effect of turbulence on particle dispersion, deposition on turbine blade surfaces and detachment from the surfaces [32], [33].

As mentioned, the velocity of an impinging particle is one of the parameters that drive the sticking process. If its value is lower than a threshold (critical velocity) the particle sticks to the surface. The threshold value is strongly dependent on the particle material and its mass. The formulation suggested in [30] for the critical velocity uses the following equation

$$v_c^2 = \frac{-1 + \mu^2}{R^2} \frac{2W_A}{m} \quad (9)$$

where W_A is the work of adhesion and R is the coefficient of restitution. According to the formulation of Brach and Dunn [30], the critical velocity is referred to the normal direction with respect to the target surface. The work of adhesion [34] could be expressed as

$$W_A = - \left[\frac{5}{4} \rho \pi^{\frac{9}{2}} (k_1 + k_2) \right]^{\frac{2}{5}} \gamma r^2 |v|^{\frac{4}{5}} \quad (10)$$

$$R = \frac{C}{C + |v|^p} \quad (11)$$

where C and p are constants that can be derived from experimental tests, while the parameters k_1 and k_2 are referred to the substrate and particle characteristics respectively. Assuming the subscript i as a material index (particle or substrate), the parameter k_i is defined according to Young's modulus E_Y and Poisson's ratio ν as

$$k_i = \frac{1 - \nu_i^2}{\pi E_{Y,i}} \quad (12)$$

Also for this model, the particle properties, and in particular its Young's modulus, are sensitive to the temperature and need to be estimated using empirical correlations. This model was applied in the case of gas turbine contamination by ash using the following relation for the particle's Young modulus [35]

$$E_{Y,p} = 120(1589 - T)^3 \quad \text{for } T > 1100 \text{ K} \quad (13)$$

and in the case of coal-particle contamination [36] using

$$E_{Y,p} = 3 \cdot 10^{20} e^{(-0.02365T)} \quad (14)$$

The critical velocity model was applied to study the gas turbine hot section fouling [36], using simplified relations for critical velocity

$$v_c = \left(\frac{2E_Y}{d} \right)^{\frac{10}{7}} \quad (15)$$

based on a composite Young's modulus E_Y obtained as

$$E_Y = 0.51 \left(\frac{5\pi(k_1 + k_2)}{4\rho^{3/4}} \right)^{\frac{2}{5}} \quad (16)$$

by considering the parameters k_1 and k_2 defined in the Eq. (12) for particle and substrate characteristics. Therefore, E_Y represents the material characteristic generated by the pair of particle and substrate.

The application of the present model requires accurate values of the Young modulus of the particle and surface. This procedure is not a standard (contrary to the critical viscosity method for which the definition of the critical viscosity equal to the particle viscosity at the softening temperature allows the results standardization). The lack of universally accepted ways to evaluate material properties may be the reason for discrepancies in predictions obtained (i) in different conditions with the same material or (ii) with different materials for the same test conditions.

A deposition model that includes elastic deformation, plastic deformation, adhesion, and shear removal is reported by Bons et al. [37]. Its predictions were compared to five literature cases: quartz on aluminum, ash on stainless steel, sand on stainless steel, ash on Inconel at high temperature and ash on vane cascade. This model is used in the numerical analysis reported by Prenter et al. [38] and Forsyth et al. [39] after tuning the model parameters. A different model was proposed by Agati et al. [40] for the numerical modeling of particle deposition that occurs in gas turbine hot sections over between 500 K to 1500 K. The transition between these two extreme conditions is modeled through a temperature-driven modification of the mechanical properties of both particles and target surface. A third method is proposed by Yu and Tafti [41] as a modification of the former model [42] and it is based on the relation between particle temperature and yield stress at a high temperature starting from 1000 K. The model prediction was compared against experimental data obtained with sand particles. As mentioned, more details about these models are reported in the paragraph *Predictive models for particle properties* of the present Chapter.

2.1.3. Energy-based model

Energy balance models are based on comparing the available energy just before the impact to the energy dissipated by the particle during its deformation. The model predicts sticking if all the available energy is dissipated to deform the particle and to adhere to the surface. The main parameters are the kinetic energy of the particle, its viscosity and surface tension, and the surface energy or contact angle [43] and [44]. The method can study deposition on an existing layer by a suitable choice of the properties of the substrate and can even be used to obtain the restitution coefficient for use in critical viscosity model calculations [45]. This model takes into account the

particle deformation due to the impact, without considering the behavior of particle viscosity such as non-Newtonian effects or possible sintering effects after particle impact. Figure 3 reports the phases involved in the particle impact phenomenon.

The model is based on the estimation of the parameter E^* that stands for the excess of energy and indicates whether all energy is dissipated during wetting and deformation. The particle will rebound if $E^* > 0$ and it will stick otherwise. The parameter E^* is defined according to [43]:

$$E^* = \frac{25}{172}\xi^2(1 - \cos\theta) + \frac{50}{129}\xi^{-1} - \frac{3}{43}\xi^{2.3}(1 - \cos\theta)^{0.63} - 1 > 0 \quad (17)$$

where θ is the contact angle and ξ is the particle spread factor. The spread factor represents the particle maximum deformation and, if d_{\max} is the maximum footprint particle diameter when the particle hits the surface, the spread factor is defined as

$$\xi = \frac{d_{\max}}{d} \quad (18)$$

Several empirical tests and spread factor quantifications are reported in the literature [46], [47], [48], [49], [50] and [51] and, for this reason, a detailed evaluation of the particle spread factor value predictions will be carried out in the present work.

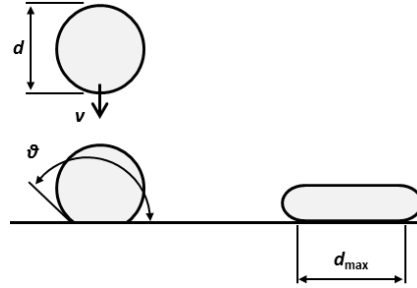


Figure 3 – Particle deformation at the impact: d_{\max} is the maximum footprint particle diameter

As mentioned, the model compares the kinetic energy to the energy dissipated by viscosity and the work done against surface tension to modify the surface area of the particle. These energies are evaluated using semi-empirical correlations. The criterion $E^* > 0$ is determined mainly by the value of the spread factor ξ . This can be appreciated by inspecting Figure 4, where E^* is shown as a function of ξ for different values of θ . In particular, it can be seen that particle adhesion takes place for $\xi > 0.4$ for most values of θ of practical interest. Therefore $\xi = 0.4$ will be used as the threshold value in the present work for particle adhesion.

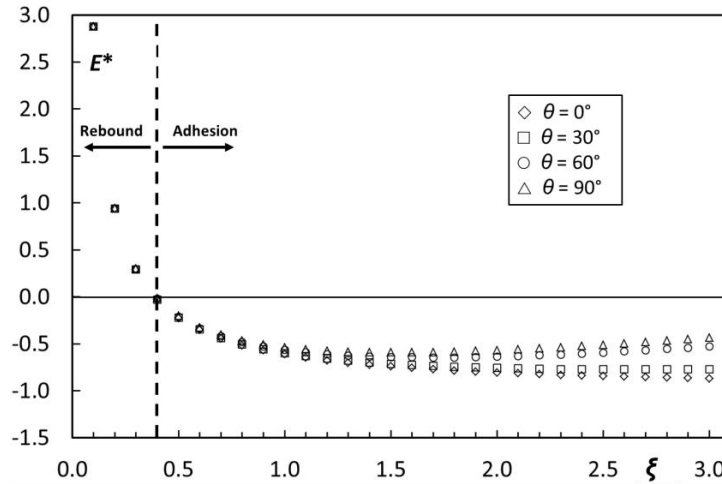


Figure 4 - Sensitivity analysis of the contact angle on E^* calculation

Sticking mechanisms and deposit formation mechanisms are based on the presences of a third substance or second phase at the particle/surface interface [52]. The presence of a third substance is usually invoked at low temperature. An example is the formation of deposits on compressor blades, where particles come into contact with water droplet or oily substances [53]. The third substance could generate favorable conditions for particle sticking especially when the particle is solid and its adhesion is driven only by electrostatic forces. In this case, in fact, the presence of third substance could change the action of capillary forces as well as the effects of the inertia and the correspondent energy dissipation during impact allowing particle sticking. The presence of a second phase is invoked also to model deposition on hot gas turbine sections in which contaminants are softened or completely molten [54]. For adhesion of particles to occur, either they must be semi-molten or a molten phase must be present on the blade surfaces. The low-melting compounds

generated by the increment of the particle temperature act as a bridge between the particle and the blade surface. Therefore, the sticking probability is dependent on a number of characteristics, such as particle temperature, viscosity, surface tension and wettability [55], [56]. In the light of this background, the prediction of particle adhesion is based on a two-step approach. The first step deals with the prediction of the particle/surface properties while the second step deals with the estimation of the sticking probability (or any other measure of adhesion) based on them.

2.1.4. Predictive sticking models

With the reference of basic models presented in the latter paragraphs (critical viscosity, critical velocity, and energy-based models), in this paragraph, different model formulations are reported. In the literature, several predictive sticking models exist starting from the basic ones and tuned according to the experimental results obtained. All of these models were used for estimating the particle deposition in the gas turbine and in agreement with their hypothesis, they could be used for fouling prediction with a certain confidence. In Table 1, these models are listed together with their peculiarities, such as, the basic criterion on which the model is based and the main positive and negative peculiarities.

The analysis proposed by Srinivasachar et al. [29], shows that the particle kinetic energy affects the critical viscosity value at which sticking starts. The experiments have shown, for a single sample of coal, that the critical viscosity value decreases for a specific particle impact velocity and diameter. The sticking efficiency transition as a function of temperature was not as sharp, due to the overlaying effects of ash size and composition distributions. It increases the reliability of the former critical viscosity model. The models proposed by Sreedharan and Tafti [22] and Singh and Tafti [57] are based on the critical viscosity criterion as well, but, in these attempts, the Authors have extended the prediction capability of the model to lower temperature. Hypothesis related to the energy dissipation at the impact imposes to the precise characterization of the particle structural characteristics. The last model based on the critical viscosity criterion is proposed by Jiang et al. [58] and is able to account for the wall temperature effects on the particle sticking capability. The model takes into account ash thermo-physical properties, particle viscosity and metal wall temperature by means of simplified relation and two model constants.

Moving to the critical viscosity criterion, the proposed model involves the mechanical properties of the particles. The model proposed by Agati et al. [40], is based on the critical velocity criterion: the model is developed according to the correlation between temperature and material properties by means of the chemical composition. Temperature based model considers material properties (E and ν) and material composition for a temperature range between 500 K and 1500 K. This interval is modeled through a temperature-driven modification of mechanical properties of particles and target surfaces. The model can also predict the coefficient of restitution for particles bouncing region.

Based on the aim of estimating the coefficient of restitution, four models are developed. In this case, the sticking phenomenon can be detected when the restitution coefficient is null. The model reported in Yu and Tafti [42], takes into account the contact models for elastic, elastic-plastic and plastic compression stages, followed by a recovery model based on the model of Stronge [59]. Then, a new elastic recovery model is proposed with molecular adhesive forces acting on the contact area. The model is more accurate in predicting the coefficient of restitution compared to the Stronge and Jackson-Green [60] models. The model is largely sensitive on the mechanical properties of sand to the grain size. With the reference of this model [42], the Authors have improved the formulation in [41] for modeling the collision of micro-sand particles by means of the adhesion forces, size and temperature dependency of particle mechanical properties. The base model is validated and the proposed temperature-dependent model is validated against experiments on the impact of micro-sand particles for impact velocities at different temperatures. However, it is validated only against experiments that involve sand particles. Bons et al. [37] proposed a physics-based model which includes elastic deformation, plastic deformation, adhesion, and shear removal. The model accounts for fluid shear removal, elastic and plastic deformation, and adhesion. The model is not fully validated in terms of the deposition prediction because of the dependency between temperature and material properties.

A different approach is adopted in [61]. The model proposed by Casari et al. [61], investigates the deposition process under a statistical perspective. This fouling model uses only the energy content of the particles, based on temperature and kinetic energy, to estimate the sticking probability. However, in a similar way of previous models, the model constants and the applicability limits are not checked against experimental results.

After this brief review of the present sticking models, it is clear how the major issue is related to the extension of predictive capability as a function of different particle chemical compositions, mechanical properties etc. Therefore, it is necessary to improve the models in order to extend the prediction capabilities together with the limitation of the use of model constants which are usually specifically tuned for each application.

Table 1 - Predictive sticking models

Basic criterion	Authors	↑ Pros / ↓ Cons
Critical viscosity	Srinivasachar et al [29]	↑ Influence of the kinetic energy on the particle sticking ↓ Critical viscosity values related only to a single coal sample
	Sreedharan and Tafti [22]	↑ Accounts for the particle softening effects ↓ Only representative of molten particles
	Singh and Tafti [57]	↑ Accounts for the energy absorbed by the particle at the impact ↓ Detailed characterization of the temperature-material characteristics relations
	Jiang et al. [58]	↑ Influence of the wall temperature on the particle sticking ↓ Model equations and constant do not account for the particle kinetic energy
Critical velocity	Agati et al. [40]	↑ Extended range of temperature ↓ Detailed characterization of the temperature-material characteristics relations
	Yu and Tafti [42]	↑ Accounting for the elastic/plastic deformation ↓ Sensitive to the on the mechanical properties of sand to the grain size.
	Bons et al. [37]	↑ Accounting for the elastic/plastic deformation, adhesion and shear removal ↓ Tuned by case-dependent coefficients
	Yu and Tafti [41]	↑ Temperature dependency on the yield stress for sand particles ↓ Sensitive to the on the mechanical properties of sand to the grain size.
Activation energy	Casari et al. [61]	↑ General approach based on an energy content comparison ↓ Lack of validation of the model constants and applicability limits

2.2. Predictive models for particle properties

Different predictive models used for particle characteristics such as viscosity, surface tension, softening and density are reported. The formulations reported in the following sections are useful for the subsequent data post-process based on literature experimental data. The particle deposition on hot gas turbine section experiments was carried out using similar materials that affect the power unit in the actual operating conditions such as sandy, volcanic and coal-type particles. All of these contaminants belong to the class of material called silica-based and are characterized by well-known interaction between their constitutive ions. Silica melts are based on the strong covalent bonding between silicon and oxygen forming a network structure. The glassy silica network can accommodate many different cations. Three main categories exist, depending on the interaction of cations and network: (i) glass formers (Si^{4+} , Ti^{4+} , P^{5+}) which form the basic anionic polymer unit, (ii) modifiers (Ca^{2+} , Mg^{2+} , Fe^{2+} , K^+ , Na^+) which disrupt the polymeric chains by bonding with oxygen and terminating chains, and (iii) amphoteric (Al^{3+} , Fe^{3+} , B^{3+}) which act either as glass formers or as modifiers. Modifier ions disrupt the glass structure and thus tend to lower viscosity. Amphoteric ions can act as glass formers when they combine with modifiers ions which balance their charge, thus forming stable metal-oxygen anion groups that can fit into the silicate network. If insufficient modifier ions are present in the glass, amphoteric cations (Al^{3+} and Fe^{3+}) can act as modifier ions [62].

2.2.1. Particle viscosity models

Several test methods exist to measure silica melts viscosity: rotating crucible, rotating bob, falling body, oscillating plate, oscillating viscometer and Static Light Scattering (SLS) [63]. The methods contain provisions to guarantee uniform temperature zone during the measuring processes. Each method has its applicability range, confidence band and requires additional data (such as density and surface tension). The rheological behavior of silica melts [64] can be assess using standard test methods, according to ASTM D 2196-15 [65], which are able to evaluate whether the slag has transitioned from Newtonian to non-Newtonian flow at the measurement temperature. Unfortunately, these test methods are defined for a specific range of shear rate ($0.1 - 50$) s^{-1} and developed for measuring the rheological properties of the liquid phase only.

Although the widespread use of rotational test methods for the assessment of rheological properties of non-Newtonian flows, several oscillatory tests can also be used to examine all kinds of viscoelastic materials from low viscosity materials to melts and dispersions. The rheological behavior of both viscous and elastic portion can be investigated by using these tests which allow the determination of the values of dynamic rheological properties, such as complex shear modulus (G^*), shear storage modulus (G') and shear loss modulus (G''). In particular, G^* can be supposed as the rigidity of material, while G' is the deformation energy stored by the material during the test and it describes the elastic behavior of the material. The G'' modulus represents the viscous behavior of the material and the deformation energy employed and then dissipated due to frictional forces that occur during the test. Moreover, another important rheological parameter is the loss factor or damping factor ($\tan\delta$) that is calculated as the quotient of the loss and the storage modulus and it represents the ratio between the viscous and the elastic portion of the viscoelastic deformation behavior. This parameter is useful for the evaluation of tacky behavior of the material and, more specifically, the presence or the absence of stringiness characteristics. In

particular, values of $\tan\delta$ lower than one and storage modulus (G') greater than shear modulus (G'') are typical characteristics of viscoelastic gels or solid materials [66].

Oscillatory tests can be performed at different conditions in which specific parameters, such as frequency, amplitude, and temperature, can be kept at a constant value or can be free to vary. For example, dynamic mechanical analysis (DMA) test provides that frequency and amplitude, together with dynamic-mechanical shear conditions are kept at a constant value, while in dynamic-mechanical thermoanalysis (DMTA) tests, the only variable parameter is the temperature. In this latter case, this test provides information about the influence of temperature on physical properties of the material, such as specific structural modifications. According to ISO 6721-10 [67], an oscillatory rheometer with parallel-plate geometry is used to determine the dynamic rheological properties of polymer melts with complex shear viscosity values up to ~ 10 MPa·s. Widespread measuring systems can be used to perform oscillatory tests, such as a concentric cylinder, cone-and-plate, and the aforementioned parallel-plate systems. For the sake of brevity, in this review, the measuring systems have been named in a brief list. For an up-to-date overview of rheological tests and a meticulous summary of typical measuring systems please refer to [66].

Each material has its own temperature-dependent characteristics, furthermore, each particle is subjected by different temperature-history in a gas turbine flow path. For this reason, the aim of the present analysis is to compare the experimental data with dimensional and non-dimensional parameters using the available data reported in the literature.

Over the past century, several equations have been proposed relating the viscosity of arbitrary melts to temperature-dependent characteristics and to specific composition constants [68]. Most of these are proposed for predicting material viscosity for specific material composition and sometimes, their validity is limited to a certain viscosity ranges. In the present review, seven (7) methods are considered. They are based on data extrapolation from temperature-viscosity trends of coal and volcanic samples similar to those responsible for gas turbine hot section fouling. In addition, all of the selected methods are able to predict the particle viscosity based on the composition and temperature. Each method is applied considering its limits according to the particle composition, beyond of the absolute value of the predicted viscosity [69], [70], [71], [72], [73], [74] and [75]. In this way, each method can be included or excluded a priori only based on the particle composition useful for automated calculation or routine easy-to-be-implemented in numerical simulations.

The considered models are based on different correlations obtained considering different physical-chemical criteria. The S^2 [70] and Watt-Fereday (WF) [71] postulate that the viscosity depends on temperature following Arrhenius' law. This corresponds to a description of the flow of silicates in terms of transition probability and vacancy distribution in the structural lattice. The NPL model by Mills and Sridhar [69] is also based on the Arrhenius equation used to describe the temperature dependence of slag viscosity and correlates the slag composition to the optical basicity of the material. In 1962, Weymann [76] proposed another equation resulting from the same deduction considered for the Arrhenius model with the addition of an extra temperature-dependent parameter. This model demonstrated a valid correlation with experimental data and a successful description of the relationship between viscosity and temperature. The models that are based on Weymann equation [76] are Sreedharan and Tafti [72] (S&T), Riboud et al. [73] (RRLG) and Streeter et al. [74] (SDS). Another equation that links the viscosity with temperature was independently proposed by Vogel [77], Fulcher [78] and Tamman and Hesse [79] in the 1920s and it is the base of the model presented by Giordano et al. [75] (GRD). In this case, a third adjustable composition parameter is introduced into the equation to improve the performance of the model and to better emphasize the dependence of temperature on silicate melts viscosity. This model is specifically realized for predicting temperature-viscosity trends of volcanic ashes.

All model coefficients, constitutive equations, and applicability limits are reported in Appendix A divided according to the model. In addition, the accuracy of the model coefficients and the confidence band related to each model are described in details.

2.2.2. Particle softening model

In addition to the particle viscosity, another basic particle characteristic is the particle softening temperature. This property is the key value for calculating particle adhesion according to the critical viscosity method. In order to post-process the literature data related to the particle deposition on hot gas turbine sections, the calculation of the present quantity is required.

For the estimation of the softening temperature, three main approaches exist. The first one is related to a visual method described in the standard procedure of ASTM – D1857-04 (*Standard test method for fusibility of coal and coke ash*) [21], the second one is carried out with a ThermoMechanical Analysis (TMA) approach while the third one is related to a thermal analysis by means of Differential Scanning Calorimetry (DSC) approach. The setup of these different methods has been carried out over the years due to the controversial question related to the deformation temperature. In the literature, in fact, it has been emphasized that the initial deformation temperature is not the temperature at which the ash melting begins, and many coal ashes have been found to start melting at temperatures far below the initial deformation temperatures [80]. Therefore, in this section, the three approaches are briefly described.

In accordance with ASTM – D1857-04 (*Standard test method for fusibility of coal and coke ash*) [21], the softening temperature (ST) is defined as the temperature at which triangular pyramid prepared from the material (see sketch n°1 in Figure 5) has fused down to a spherical particle which is characterized by the height equal to the width at the base (see sketch n°3 in Figure 5). The softening temperature has been accepted as the critical temperature which is commonly referenced in the evaluation of the characteristics of coal ash [81]. The ash fusion test (AFT) is considered the most widely used procedure for determining the temperature at which the different

stages of the ash transformations (softening, melting and flow) take place in order to assess the deposition characteristics of the material [82]. The fusion temperature values are determined by heating a prepared sample of molded coal in a gas-fired or electric furnace conforming to [21]. The deformation of the molded ash cone is monitored during the increase of temperature and, according to Figure 5, the four (4) critical temperature points (fluid – FT; hemispherical – HT; initial deformation – IT; softening – ST) are determined. Moreover, the response of the sample to thermal treatment is generally quantified by optical pyrometer or thermocouple. An alternative approach for the evaluation of the four (4) critical temperature values, applied to volcanic ash samples, consists in the use of thermogravimetry and differential scanning calorimetry (DSC) [83] and [84]. Mechanically, the evolution of characteristic temperature and the geometrical transformations of the cone define the ability of the sample to sinter, to stick or to spread and wet the surface [85]. Nevertheless, the standard test [21] can be susceptible to subjective assessment because of the visual evaluation of critical temperature points [86]. The standard procedure is recognized as not a very precise method failing the prediction of the fusibility temperature by over 40 K [87] as a function of the amphoteric content. In addition, it was found that the deformation temperature is not the temperature at which initial melting begins as normally perceived and the hemisphere temperature is below the liquidus temperature.

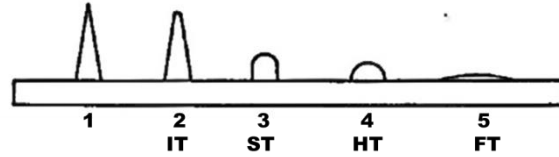


Figure 5 – Critical temperature points taken from ASTM – D1857-04 [21]

The TMA methodology evaluates the progressive shrinkage of ash and it is suitable for characterizing the sintering and melting behavior at temperatures lower than the standard method. In addition, the precision of this technique is greater than the standard one, reducing the inaccuracy due to the measurement method. However, this accurate methodology cannot be applied to ashes from biomass combustion [80] and in this case, the use of the DSC technique appears the best solution. This methodology is based on the evaluation of any mass changes by means of the comparison between the ash behavior against the reference material. With this procedure, any deviation in terms of energy corresponds to an evaporation or melting process with an accurate estimation of the most ash fusibility temperature values.

Despite the background of conventional techniques for determining the transformation temperature, the evaluation of the critical temperature values from the chemical composition can be a difficult task because of the unknown correlation between the interacting factors. In the present paper, starting from the particle characteristics reported in the literature, empirical relations to compute the particle softening temperature as a function of the composition proposed by Yin et al. [88] were used. This model is much easier and direct than other statistical methods through the possibility to omit the mathematical correlation between the variables. In addition, the aim of the present study is to compare the experimental literature data and, for this reason, particle softening temperature has to be computed only by the use of the particle chemical composition. According to particle composition, different relations are proposed.

When the content of SiO_2 is less than or equal to 60 %, and the content of Al_2O_3 is larger than 30 %

$$T_{\text{soft}} = 69.94\text{SiO}_2 + 71.01\text{Al}_2\text{O}_3 + 65.23\text{Fe}_2\text{O}_3 + 12.16\text{CaO} + 68.31\text{MgO} + 67.19a - 5485.7 \quad (19)$$

when the content of SiO_2 is less than or equal to 60 %, the content of Al_2O_3 is less than or equal to 30 % and the content of Fe_2O_3 is less than or equal to 15 %

$$T_{\text{soft}} = 92.55\text{SiO}_2 + 97.83\text{Al}_2\text{O}_3 + 84.52\text{Fe}_2\text{O}_3 + 83.67\text{CaO} + 81.04\text{MgO} + 91.92a - 7891 \quad (20)$$

when the content of SiO_2 is less than or equal to 60 %, and that of Al_2O_3 is less than or equal to 30 %, and that of Fe_2O_3 is larger than 15 %

$$T_{\text{soft}} = 1531 - 3.01\text{SiO}_2 + 5.08\text{Al}_2\text{O}_3 - 8.02\text{Fe}_2\text{O}_3 - 9.69\text{CaO} - 5.86\text{MgO} - 3.99a \quad (21)$$

and finally, when the content of SiO_2 is larger than 60 %

$$T_{\text{soft}} = 10.75\text{SiO}_2 + 13.03\text{Al}_2\text{O}_3 - 5.28\text{Fe}_2\text{O}_3 - 5.88\text{CaO} - 10.28\text{MgO} - 3.75a + 453 \quad (22)$$

The constant a is defined according to the weight fraction wt% of each component as

$$a = 100 - (\text{SiO}_2 + \text{Al}_2\text{O}_3 + \text{Fe}_2\text{O}_3 + \text{CaO} + \text{MgO}) \quad (23)$$

2.2.3. Particle surface tension model

The third particle characteristic useful for applying the particle sticking methods is the particle surface tension. In the literature, several contributions are related to the measurement of surface tension values of slags and silicate melts [89], [90], [91], [92], [93], [94], [95] and [96]. Ternary or more complex slags, as well as coal ashes, are taken into consideration. These analyses are mainly focused on the estimation of the temperature effects on the surface tension values. Even if, these contributions report very detailed slags and ashes characterizations, both in terms of chemical composition and surface tension values, they are mainly focused on the high-temperature values at which these materials are characterized by the liquid phase. For this reason, the actual slag and ash characterization cannot be

applied to the present study, due to the different temperature ranges at which gas turbine operates (lower temperature values than the slag/ash characterization). Therefore, in the present work, the particle surface tension is calculated using a chemical-temperature dependent correlation based on the principle that the surface tension can be expressed as a linear function of the composition [97]

$$\gamma = \sum (\gamma_i m_i) \quad (24)$$

where γ is the surface tension corresponding to each oxide i and m is its molar fraction. The surface tension of each oxide is taken from literature correlations [98], [99]. Table 2 reports the equation of the relation $\gamma = f(T)$ used in the present analysis. The contribution of potassium oxide and titanium dioxide are not considered.

Table 2 - Surface tension [mN/m] of single oxide

Component	$\gamma = f(T)$ [mN/m]
SiO ₂	243.2+0.0031 T [K]
CaO	791-0.0935 T [K]
Al ₂ O ₃	1024-0.177 T [K]
MgO	1770-0.636 T [K]
Na ₂ O	438-0.116 T [K]
Fe ₂ O ₃	504-0.0984 T [K]

By means of this approach, the different chemical composition can be considered in the estimation of particle surface tension. In addition, with the use of the linear function, the particle surface tension is computed according to the precise correlation between temperature and surface tension of every single oxide.

2.2.4. Particle density model

Several models for density calculation have been provided through the years [100], [101] and [102]. The possibility to calculate the particle density starting from the chemical composition give the possibility to overpass the experimental characterization, even if, the approximation related to the use of a general correlation may affect the validity of the results. However, the measurement and/or the calculation of the particle density is usually used for the estimation of the particle mass that is, based on the present literature, less important than other particle characteristics such as viscosity, softening temperature, and surface tension. One of the most common methods is proposed by Bottinga et al. [103], based on the sum of the contribution of all components except Al₂O₃ and the other due to the contribution of Al₂O₃. This distinction is due to the different approach used in literature to estimate the apparent partial volume fraction of the aluminum silicate. With this model, the densities, ρ , of molten slags from can be obtained by the following two equations

$$V_m = \sum (X_i V_i^0) + X_{Al_2O_3} V_{Al_2O_3}^0 \quad (25)$$

$$\rho = \frac{M}{V_m} \quad (26)$$

where the sum of Eq. (25) is taken over all oxide components except the aluminum trioxide. In the Eq. (25) X is mole fraction of component i , while V^0 terms represent the apparent partial volume of slag constituents. They are constant and derived independently from an analysis of volume-composition relations in alumina-free silicate liquids. In Eq. (26), M represents the sum of the molar weight for the given slag. The apparent partial molar volumes of SiO₂ and Al₂O₃ are polynomial functions of composition in the density model proposed by Mills and Keen [104] for multicomponent slags. Based on [103], the Authors adjust the partial molar volume values (V^0) achieving certain success in calculated data with an uncertainty of 2 %. Different model constants provided by [103] and [104] for calculating V^0 of various slag constituents are listed in Table 3. In the present work, the apparent partial volume of slag constituents reported [104] are used.

Table 3 – Recommended values for apparent partial molar volume V^0 of slag constituents

Component	V^0 at 1673 K [103] [cm ³ /mol]	V^0 at 1773 K [104] [cm ³ /mol]
SiO ₂	26.75	19.55 + 7.966 X_{SiO_2}
TiO ₂	22.45	24.0
Al ₂ O ₃	-	28.31 + 32 - 31.45 $X_{Al_2O_3}^2$
Fe ₂ O ₃	44.40	38.4

MgO	12.32	16.1
CaO	16.59	20.7
MnO	14.13	15.6
Na ₂ O	29.03	33.0
K ₂ O	46.30	51.8

3. EXPERIMENTAL DATA OF GAS TURBINE PARTICLE DEPOSITION

Deposition tests in conditions representative of the hot parts of a gas turbine have been conducted over the years with a number of different materials. The tests involve five principal types of particles [105]: sand, ash, coal, bituminous coal, and lignite.

Sand is defined as mineral particles of diameter 2 mm to micronized powder. In the gas turbine field of research, sandy particles are usually referred to Arizona Road Dust (ARD) silty samples. This sandy powder takes inspiration from the standard powder of ISO 12103-1 (A1, A2 A3, and A4) [106], but the size and chemical composition of particle used in the deposition tests could be different from the standard one due to the mixing, filtration, sieving, and processes applied before the tests.

Ash comprises all pyroclastic particles or fragments ejected from a volcano, irrespective of size, shape or composition. The term is usually applied to an air-fall material characterized by a characteristics diameter less than 2 mm.

Coal is a carbon-rich mineral deposit formed from the remains of fossil plants. The process of coalification results in the production of coals of different ranks such as bituminous coal, lignite, and anthracite. Each rank marks a reduction in the percentage of volatiles and moisture and an increase in the percentage of carbon. According to this definition, ASTM standard [107] proposed a detailed coal classification based on the content of carbon, volatile matter and calorific limits. Unfortunately, this classification is not completely useful to understand the physical characteristics of the contaminants involved in gas turbine degradation. Physical characteristics such as viscosity and surface tension are dependent on the chemical composition and structure (e.g. crystalline or amorphous) of the contaminants. In addition, it is important to note that the chemical composition of slag and its correspondent original coal ash could be different. As reported by Streeter et al. [74], slags chemical composition could change due to the depletion of iron oxides species or to the enhancement in alumina content during heating/melting processes. At the same time, high-temperature values generate the volatilization of the sodium oxide that could change the slag viscosity. These behaviors enhance the difficulties related to the characterization and classification of the contaminants that affect hot sections.

Particle deposition is investigated in order to understand turbine section contamination and the interaction between cooling holes and particle deposition. Accelerated tests are frequently used to recreate the actual gas turbine condition using in-house experimental test bench. For example, accelerated deposition testing is realized within 4 hours which cover 10,000 hours of actual gas turbine operation [108]. Sometimes, in order to study specific problems, deposition tests are conducted using a coupon instead of gas turbine cascade [109], [110], [111], [112], [113], [114], [115], [116], [117], [118], [119], [120], [121], [122], [123] and [124]. In this type of test, the particle deposition occurs on specifically-designed target, usually characterized by simplified geometry in order to guarantee a certain flow and temperature fields. In this case, the experimental procedure allows the proper correlation between particle impact conditions and deposition phenomenon based on the criterion that, all of the injected particles are characterized by the same impact conditions such as temperature, velocity, and incoming angle. In addition, given the simplified geometry of the coupon, detailed evaluation of several peculiarities such as (i) surface roughness of the deposited layer, (ii) effects of the cooling hole array, (iii) deposits thickness and (iv) influence of the substrate temperature on the particle sticking capability can be easily carried out. In Figure 6 an example of this evaluation is reported. In particular, Figure 6a shows the evaluation of deposit surface roughness, Figure 6b depicts the influence of the presence of cooling holes on the particle deposition pattern and, finally, Figure 6c reports an evaluation of the deposit thickness by means of a three-dimensional detection carried out with a laser scanner.

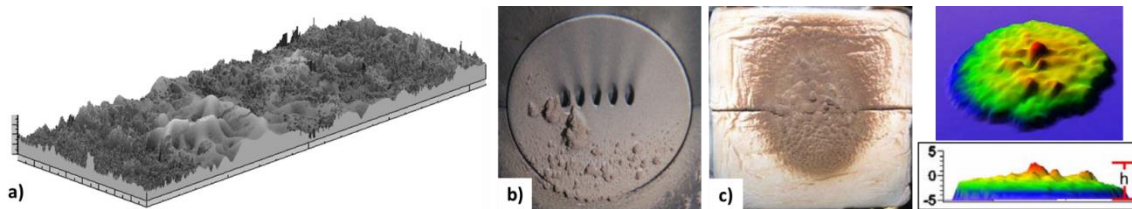


Figure 6 - Experimental particle deposition tests carried out on coupons: a) evaluation of the surface roughness [114], b) effects of the cooling hole array [119] and c) measurement of the deposit thickness by means of the three-dimensional reconstruction based on laser scanner detection [120]

Earliest contributions are related to deposits due to fuel contamination. Several studies can be found in literature [125], [126], [127], [128], [129], [130], [131], [132], [133], [134] and [135] but no specific details about particle sticking probability is reported, or the

chemical compositions is too different from the silica-based materials [136]. Analytical schemes were developed for extracting sticking coefficients from the measured weight gain data, particle size spectrum, and particle density and composition [56]. The influence of the particle temperature was one of the first studies reported in the literature [137]. The particle temperature determines the appearance of different composites with different characteristics. For example, in the temperature interval (800 – 1800) K, the multi-component solution comprises oxides, sulfates, silicates, and aluminosilicates. Below 1100 K, low-melting alkali sulfate solutions are the predominant components, whereas above about 1500 K, molten oxides constitute most of the liquid phase. At high temperature, vapor deposition driven by thermophoresis force becomes important. Differences in deposits were encountered for pressure and suction sides where diffusion phenomenon works as a leading actor [138] and [139].

At the same time, the first studies on the effects of volcanic ash on aero-engines were published. Tests with different power unit using a unique facility able to generate realistic environmental conditions of particle-laden clouds under controlled laboratory conditions are carried out [140], [141] and [142]. The results show the variation of the power unit performance during the test (a few minutes) highlighting the deterioration over a small period. Evaluations of blade erosion and deposition patterns are also proposed. This type of studies are not widespread in literature and only in the last years, new studies have been proposed related to simply particle deposition [143], [144] and [145], cooling holes blockage [146], [147] and internal cooling hole clogging [148]. Cooling holes clogging represent the most detrimental phenomenon that occurs in gas turbine hot section, especially for aero-engines. Figure 7 reports literature experimental results showing the occupied area due to particle adhesion inside the cooling hole. More recently, Shinozaki et al. [149] and Naraparaju et al. [150] use a micro gas turbine for studying volcanic ash adhesion at different load and for different blade coating materials, respectively.



Figure 7 – Internal cooling hole clogging [148]: deposition in first four cooling holes of HD45 running at 1310 K

With the increase in usage of gas turbines for power generation and given that natural gas resources continue to be depleted, alternative types of fuel have been tested. Examples of alternative fuels are coal-derived synthetic fuels. Coal-derived fuels could contain traces of ash and other contaminants that can deposit on vane and turbine surfaces. Experimental tests and numerical analyses are devoted to the comprehension of the effects provided by bituminous and sub-bituminous particles on the gas turbine nozzle [151]. Several studies were realized in order to increase the effects of these contaminants on gas turbine hot section fouling, especially in the presence of film cooling. Different types of ash (e.g. coal bituminous, lignite, etc.) have been used for performing particle deposition on a gas turbine nozzle [12], [26] and [152]. Such tests allow the proper analysis of the flow dynamic behavior in the particle impact and adhesion phenomena, giving the possibility to realize the same flow conditions of the actual application. By contrast, the complexity of the flow structure and the effects of geometric features that characterize an actual gas turbine nozzle could represent an obstacle in the definition of general rules and trends related to particle sticking. In Figure 8 the comparison between the deposits pattern without and with film cooling using bituminous ash is reported. The effect of cooling holes on particles deposition pattern is still under investigation. Experimental tests [153], also run with high gas temperature [154], attempt to improve the comprehension of particle deposition.

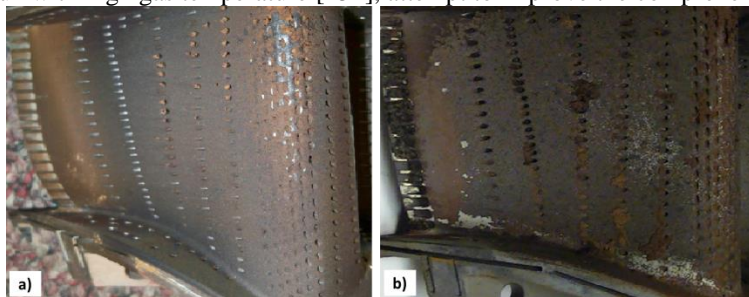


Figure 8 – Comparison of coal bituminous particle tests (a) film cooling (b) non-film cooling [12]

Other specific contributions can be found in relation to the effects of the electrostatic charge on particle deposition [155] and [156], the assessment of the thermophoresis force on the particle deposition in the gas turbine engine secondary air system [157], the investigation of sintering process of the deposits [158], and the influence of the deposit on the heat transfer and the influence of the free-stream turbulence on the particle deposition [159]. The deposits thickness influences the heat transfer and, through experimental tests, it is possible to correlate the thickness and the heat transfer over the operating time [160].

Finally, some attempts to use a sort of thermal similitude for studying particle adhesion were proposed [161], [162], [163], and [164]. These experimental tests were based on the similarities between melting ash and wax/PVC particles. Latter materials have lower values of melting temperature and, using thermal scaling techniques, the deposition pattern could be assumed as representative of actual gas turbine particle deposition.

4. LITERATURE DATA COLLECTION

The experimental results related to particle deposition on cascade and/or coupon reported in the literature, are obtained with different (i) material (ii) size and (iii) working conditions such as velocity and temperature. These different working conditions imply several difficulties in comparing deposition results obtained from different experimental tests. Different material compositions determine, for example, different values of particle viscosity even if the tests are carried out at the same particle temperature. The same phenomenon affects also the surface tension value (closely related to the surface energy), that, in addition with the viscosity, drives the adhesion phenomena at the particle/surface interface [34]. On the other hand, differences in impact velocity and particle dimension values determine different impact mechanisms and particle deformation related for example to the particle kinetic energy.

In the light of these considerations, in this paragraph, all the experimental results related to particle deposition on the hot gas turbine section are summarized. Starting from the information reported in every single work, particle composition and temperature are used to calculate viscosity and surface tension based on the relations available in literature and reported earlier. Coupling these values with particle velocity, density, and dimension, the calculation of the particle adhesion according to the analytical models (critical viscosity, critical velocity, and energy-based models) are performed, highlighting pro and cons of each method. Special attention is given to the particle viscosity which is considered the most important parameter for judging the particle adhesion or rebound phenomena.

4.1. Experimental test conditions

Tables 4 – 6 report the experimental data available in literature related to particle deposition in gas turbine hot sections for silty, volcanic and coal particles, respectively. Each material is indicated with the same name used in the respective reference. In the case of more than one contribution that uses the same material, with different test conditions, a progressive number is adopted. For each test (grouped according to the reference), the particle characteristics such as dimension and density are reported. The particle dimension indicates the variability range or the mean mass diameter used in each test (if provided). Unfortunately, detailed data on other interesting parameters such as d_{50} and d_{75} , which represents the diameters for which the 50 % and 75 % of the particles measured are less than the stated size, are not reported.

The test conditions are also indicated and, in absence of detailed information, particle velocity is assumed equal to the gas velocity and particle temperature is assumed equal to the gas temperature. Fixed value or the indicated variability range is also specified. Regarding the velocity, in the case of test realized on a full-scale gas turbine, a representative particle impact velocity of 100 m/s is chosen because no-data related to this variable is reported [141] and [142].

Finally, Tables 4 – 6 report also the type of target, tg , used in the experimental tests, with a reference of:

- T, the test is realized on a full-scale gas turbine;
- B, the test is realized on wind tunnel provided with cascade or single blade target;
- C, the test is realized using a coupon;
- I, the test is realized in order to discover particle deposition inside the internal cooling hole.

All of this information (dimension, density, velocity, and temperature) provide the first overview of the experimental contribution related to particle deposition and fouling on gas turbine hot sections. Particle velocities span from 15 m/s to 350 m/s while the temperature values range from 850 K to 1900 K, approximately. Wind tunnel tests allow the best control in terms of test parameters but, at the same time, could imply certain limits related, especially to a maximum temperature value.

Starting from this detailed information, the particle Stokes number and the particle relaxation time can be calculated. In Appendix B data about the geometrical features of the target for each experimental test are reported. Particle Stokes number and particle relaxation time are listed in relation to the airflow characteristics calculated assuming pure air as a carrier gas with characteristics calculated according to CoolProp library [165].

4.2. Experimental uncertainties

The uncertainty related to the experimental test conditions and at in turn, the accuracy of the particle deposition results, are not always reported in literature even if a considerable number of tests indicate the experimental uncertainty [12], [26], [56], [108], [111], [112], [115], [116], [118], [119], [120], [122], [148], [152], [153] and [159]. The difficulties are especially related to the not-clear correlation between the uncertainties related to test conditions like flow velocity and temperature and mass deposits or sticking

coefficients. Measurement uncertainties have to be considered different from the variability of the test conditions even if, both of them determine the amount of deposits. The present data collection allows the definition of a sort of tolerance band of the experimental data reported in the present review.

Given the sticking model relations which are based on the particle characteristics strongly related to the temperature, one of the most important uncertainties related to the experimental results is that which characterizes the temperature measurements. Uncertainties related to the temperature values are estimated equal to 0.11 % [148], 1.3 % [116] and 2 % [12], [26], [152], and [159]. These values have to be correlated with the actual temperature in order to highlight the influence of the measurement uncertainty on the particle characteristic and thus, on their sticking capability. According to the aforementioned percentage values, the uncertainty in terms of Kelvin become equal to 1 K [148], 19 K [116], and 27 K [12], [26], [152], and [159]. Given the high temperature at which the tests were carried out (up to 1500 K), these uncertainty values appear in line with those reported in literature even if, according to the analysis reported in the following paragraphs, a slight deviation could be determined between the sticking prediction provided by the models and the actual results of the experimental tests.

In the same way of the temperature measurement, even the uncertainties related to the mass flow rate are useful to improve the comprehension of the experimental results. In particular, these uncertainty values could be used to estimate the uncertainty in the particle impact velocity. For the collected data, these uncertainty are estimated to be equal to about 0.80 % [148] and 4 % [12], [26], [115], and [159]. According to the percentage values, the uncertainty of the mass flow rates in [148] is equal to 0.0074 g/s, while in [12], [26], [115], and [159], the maximum uncertainty value is equal to 0.015 kg/s.

Regarding the uncertainty of the particle concentration used to contaminate the main air flow, data are not commonly reported. Only in [108] and [115] the accuracy in the particle contamination is reported and is equal to 6 ppmw (parts per million weight). Other uncertainties are related to the geometry and position of the target [120], [122], in the capture efficiency evaluation [118], [119] and mass measurements [116]. Proper methods for uncertainty estimation are adopted in [148] by applying [166] and [152], [12] using the procedure reported in [167]. In other cases, the uncertainties were estimated by duplicating the tests as reported in [112] and [119].

In relation with the variability of the tests condition during the deposition tests, the variability of the flow temperature is between 3 K [159] (for a tested flow temperature of 1353 K), 6 K [12] (for a tested flow temperature in the range of 1314 K – 1385 K) and 5 K in [153] (for a tested flow temperature of 866 K). Regarding the variability of the mass flow rate, in [159] is declared equal to 0.005 kg/s (that corresponds to the 2.8 % and 1.4 % for a tested mass flow rate values of 0.181 kg/s and 0.363 kg/s, respectively) while in [12] is declared equal to 0.01 kg/s (that corresponds to the 1.8 % and 2.7 % for a tested mass flow rate values of 0.557 kg/s and 0.365 kg/s, respectively). Other inaccuracies are especially related to the effects of radiation on the flow temperature measures [56], [111] and [116].

Data collection covers about thirty (30) years of particle deposition tests, realized using several different facilities and instrumentations. The amount of data, their variability, and their different nature give the possibility to discover the widest view of particle deposition on the gas turbine hot section. The present analysis is based on the data available in open literature, and the data post-process reported in the following paragraph allows the comprehension of the basic phenomena using per-order-of-magnitude variations.

Table 4 – Silty particle deposition data. Material composition in term of weight fraction

	Authors	Material	d [μm]	ρ [kg/m^3]	v [m/s]	T [K]	TT	Na ₂ O	K ₂ O	CaO	MgO	SiO ₂	Al ₂ O ₃	TiO ₂	Fe ₂ O ₃
2017	Barker <i>et al.</i> [123]	ARD ⁺	10–35	2560	80	1373	C	2.3	3.3	3.8	1.3	72.8	10.8	0.3	5.3
	Boulanger <i>et al.</i> [124]	ARD 2 ⁺	20–40	2560	70	1273–1373	C	2.3	3.3	3.8	1.3	72.8	10.8	0.3	5.3
	Whitaker <i>et al.</i> [147]	ARD 3 ⁺	0–10	2560	40	920–1262 ^Δ	I	2.3	3.3	3.8	1.3	72.8	10.8	0.3	5.3
2016	Boulanger <i>et al.</i> [122]	ARD 4 ⁺	20–40	2560	70	1273–1373	C	2.3	3.3	3.8	1.3	72.8	10.8	0.3	5.3
	Whitaker <i>et al.</i> [153]	ARD 5 ^{*,*}	0–20	2560	21	866 [◊]	I	0.0	0.0	3.3	0.0	84.8	9.9	0.0	2.1
	Lundgreen <i>et al.</i> [154]	ARD 6 ^{*,*}	0–5	2560	70	1363–1623	B	0.0	0.0	3.0	0.0	85.0	10.0	0.0	2.0

⁺ The particle diameters used in these tests could be different from the standard ones reported in the ISO 12103-1 (A1, A2 A3, and A4) [106] due to filtration, sieving, and processes applied by the Authors

^{*} ARD 5 and ARD 6 have different chemical compositions with respect to ARD, ARD 2, ARD 3 and ARD 4

^Δ Temperature values refer to the surface wall temperature. Gas temperature was set equal to 866 K

[◻] Temperature values refer to the surface wall temperature. Gas temperature was set in the range (800 – 900) K

[◊] Temperature values were set in the range (700 – 866) K but particle deposition was founded for the highest temperature value (866 K)

Table 5 – Volcanic ash particle deposition data. Material composition in term of weight fraction

	Authors	Material	d [μm]	ρ [kg/m^3]	v [m/s]	T [K]	TT	Na ₂ O	K ₂ O	CaO	MgO	SiO ₂	Al ₂ O ₃	TiO ₂	Fe ₂ O ₃
2018	Naraparaju <i>et al.</i> [150]	EYJA	0.5–10	849	200	1773	T	3.6	2.7	1.6	1.3	78.6	11.3	0.3	0.7
2017	Giehl <i>et al.</i> [145]	Basalt	5–125	2800	15	1373–1773	C	3.0	0.5	10.2	5.9	52.0	13.0	2.8	12.4
		Andesite	5–125	2600	15	1373–1773	C	3.7	0.7	8.8	5.6	53.9	18.7	1.0	7.4
		Dacite	5–125	2700	15	1373–1773	C	4.4	2.4	3.7	0.8	63.7	13.5	0.8	7.8

2016	Wylie <i>et al.</i> [148]	Rhyolite	5–125	2500	15	1373–1773	C	6.4	2.4	2.9	1.0	73.4	11.9	0.9	2.8	
		EYJA 2 °	4.8–34.9	849	80	1163–1293 [□]	I	2.0	2.0	4.6	0.0	51.3	10.9	1.4	9.5	
		Chaiten VA	4.8–34.9	849	80	1163–1293 [□]	I	2.9	2.9	1.6	0.0	73.9	14.0	0.2	1.6	
	Dean <i>et al.</i> [144]	Laki [×]	5–50	2400	106	1043–1295	C	6.4	0.3	6.3	8.3	52.6	18.8	1.3	6.1	
		Hekla ^{2×}	5–50	1500	106	1043–1295	C	7.3	1.2	2.0	1.4	67.4	18.1	0.0	2.6	
		Eldgja ^{3×}	5–50	1900	106	1043–1295	C	6.9	0.3	6.2	7.1	50.3	19.7	2.4	7.3	
		Askja ^{4×}	5–50	1400	106	1043–1295	C	5.6	1.5	1.7	1.8	71.9	15.5	0.0	2.0	
	Taltavull <i>et al.</i> [143]	Laki 2 ^{5×}	10–70	2400	91	1043	C	1.2	0.1	7.8	3.1	47.2	11.6	3.7	25.2	
		Laki 3 ^{5×}	10–70	2400	106	1160	C	1.2	0.1	7.8	3.1	47.2	11.6	3.7	25.2	
		Laki 4 ^{5×}	10–70	2400	127	1295	C	1.2	0.1	7.8	3.1	47.2	11.6	3.7	25.2	
	‘13	Shinozaki <i>et al.</i> [149]	Laki 5	20–100	2400	365	1343	T	1.2	0.1	7.8	3.1	47.2	11.6	3.7	25.2
	‘96	Dunn <i>et al.</i> [142]	St Helens	23	2700	100	1283–1558	T	4.5	1.6	4.5	1.6	63.2	16.4	0.6	4.1
			Twin Mountain	73	2730	100	1283–1558	T	0.5	4.2	10.6	1.5	50.3	13.2	1.9	15.3
	‘93	Kim <i>et al.</i> [141]	St Helens 2	23	2700	100	1394–1494	T	4.5	1.6	4.5	1.6	63.2	16.4	0.6	4.1

° EYJA 2 has different chemical compositions with respect to EYJA

× The chemical composition in terms of oxide weight fraction was derived starting from the element count % reported in [144] (Si 17.5 %, Al 7.1 %, Na 3.4 %, Ca 3.2 %, Mg 3.6 %, Ti 0.6 %, K 0.2 % and Fe 3.4 %)

2× The chemical composition in terms of oxide weight fraction was derived starting from the element count % reported in [144] (Si 21.4 %, Al 6.5 %, Na 3.7 %, Ca 1.0 %, Mg 0.6 %, Ti 0.0 %, K 0.7 % and Fe 1.4 %)

3× The chemical composition in terms of oxide weight fraction was derived starting from the element count % reported in [144] (Si 16.0 %, Al 7.1 %, Na 3.5 %, Ca 3.0 %, Mg 2.9 %, Ti 1.0 %, K 0.2 % and Fe 3.9 %)

4× The chemical composition in terms of oxide weight fraction was derived starting from the element count % reported in [144] (Si 23.6 %, Al 5.8 %, Na 2.9 %, Ca 0.9 %, Mg 0.8 %, Ti 0.0 %, K 0.9 % and Fe 1.1 %)

5× The chemical composition in terms of oxide weight fraction was derived starting from the element count % reported in [143] and [149] and it is different from the Laki composition reported in [144] (Si 24.0 %, Al 6.7 %, Na 1.0 %, Ca 6.1 %, Mg 2.0 %, Ti 2.4 %, K 0.1 % and Fe 21.3 %)

Table 6 – Coal particle deposition data. Material composition in term of weight fraction

	Authors	Material	d [μm]	ρ [kg/m ³]	v [m/s]	T [K]	TT	Na ₂ O	K ₂ O	CaO	MgO	SiO ₂	Al ₂ O ₃	TiO ₂	Fe ₂ O ₃
‘16	Laycock and Fletcher [121]	JBPS A	4	2330	200	1523–1673	C	2.5	0.9	5.1	1.6	63.6	17.3	1.1	4.2
‘15	Whitaker <i>et al.</i> [159]	JBPS B	4.63; 6.48	2320	70	1353	B	3.7	1.6	9.4	1.7	49.9	11.5	3.0	14.5
‘14	Prenter <i>et al.</i> [26]	JBPS B	6.48	2320	70	1353	B	3.7	1.6	9.4	1.7	49.9	11.5	3.0	14.5
2013	Casaday <i>et al.</i> [151]	JBPS B 2	11.6	2320	79	1366	B	3.7	1.6	9.4	1.7	49.9	11.5	3.0	14.5
	Laycock and Fletcher [120], [168]	JBPP **	3; 13	1980	200	1523	C	3.9	1.7	9.9	1.8	52.4	12.1	3.1	15.2
2012	Webb <i>et al.</i> [12]	Lignite	12.5	2818 [∘]	70	1314–1371	B	0.8	1.0	31.7	3.6	32.8	14.2	2.6	9.8
		Bituminous	14.1	1980	70	1339–1366	B	0.3	2.0	2.3	0.6	25.3	11.0	1.9	52.7
		PRB	18.3	2989 [∘]	70	1315–1385	B	1.8	0.5	42.2	6.9	22.1	10.5	2.2	6.1
		JBPS B 3	12.5	2320	70	1317–1343	B	3.7	1.6	9.4	1.7	49.9	11.5	3.0	14.5
	Ai <i>et al.</i> [119]	Coal (bit.)	13.4	1980	170	1456	C	6.9	2.6	8.7	3.6	47.4	17.8	1.6	6.4
	Ai <i>et al.</i> [118]	Coal (bit.) 2	16	1980	180	1453	C	6.9	2.6	8.7	3.6	47.4	17.8	1.6	6.4
‘11	Ai <i>et al.</i> [117]	Coal (bit.) 3	4, 13.4	1980	170	1453	C	6.9	2.6	8.7	3.6	47.4	17.8	1.6	6.4
‘10	Smith <i>et al.</i> [152]	Bituminous mean14	14	1980	70	1181–1272	B	0.0	2.5	2.9	0.0	32.9	20.3	0.0	40.6
2008	Crosby <i>et al.</i> [116]	Coal (bit.) 4	3.1–16	1980	170	1133–1456	C	6.9	2.6	8.7	3.6	47.4	17.8	1.6	6.4
		Petcoke	6.3	2900	170	1133–1456	C	4.3	2.5	7.5	2.2	38.3	14.5	0.8	22.9
	Wammack <i>et al.</i> [115]	BYU SEM	16	2500	220	1423	C	0.0	7.3	13.7	0.0	60.2	4.5	0.0	10.7
2007	Bons <i>et al.</i> [114]	Coal (bit.) 5	13.3	1980	200	1423	C	6.9	2.6	8.7	3.6	47.4	17.8	1.6	6.4
		Petcoke 2	33.0	2900	200	1423	C	4.3	2.5	7.5	2.2	38.3	14.5	0.8	22.9
		Straw	17.6	1680	200	1423	C	1.7	23.4	7.8	2.5	48.4	1.8	0.0	5.0
		Sawdust	19.7	960	200	1423	C	5.9	10.7	42.9	12.4	11.6	5.1	1.3	1.0
‘05	Jensen <i>et al.</i> [108]	BYU SEM	16	2500	220	1423	C	0.0	7.3	13.7	0.0	60.2	4.5	0.0	10.7
1992	Richards <i>et al.</i> [112]	Arkwright	0–40	1980	300	1373	C	0.9	1.2	5.8	1.3	48.1	25.1	1.3	11.0
		Blue Gem	0–40	1980	300	1373	C	1.5	0.5	7.0	2.5	16.9	22.8	2.0	29.6
		Arkwright 2	0–20	1980	300	1573	C	0.9	1.2	5.8	1.3	48.1	25.1	1.3	11.0
		Blue Gem 2	0–20	1980	300	1573	C	1.5	0.5	7.0	2.5	16.9	22.8	2.0	29.6
199	Anderson <i>et al.</i> [111]	Arkwright	0–40	1980	300	1373	C	0.9	1.2	5.8	1.3	48.1	25.1	1.3	11.0

		Blue Gem	0–40	1980	300	1373	C	1.5	0.5	7.0	2.5	16.9	22.8	2.0	29.6
		Arkwright 2	0–20	1980	300	1573	C	0.9	1.2	5.8	1.3	48.1	25.1	1.3	11.0
		Blue Gem 2	0–20	1980	300	1573	C	1.5	0.5	7.0	2.5	16.9	22.8	2.0	29.6
	Wenglarz and Fox [132], [133]	Ash-fuel 1	10.2	1900	150	1253–1373	C	0.6	1.2	3.8	0.0	12.0	14.2	0.8	20.4
		Ash-fuel 2	8.5	1900	150	1253–1373	C	0.7	1.0	3.4	0.0	11.5	13.9	0.8	21.9
		Ash-fuel 3	14.5	1900	150	1253–1373	C	1.0	0.9	4.7	0.1	7.5	10.9	1.0	23.1
1989	Ahluwalia <i>et al.</i> [56]	Ash-fuel 1	10.2	1900	150	1253–1373	C	0.6	1.2	3.8	0.0	12.0	14.2	0.8	20.4
		Ash-fuel 2	8.5	1900	150	1253–1373	C	0.7	1.0	3.4	0.0	11.5	13.9	0.8	21.9
		Ash-fuel 3	14.5	1900	150	1253–1373	C	1.0	0.9	4.7	0.1	7.5	10.9	1.0	23.1
1988	Ross <i>et al.</i> [110]	Arkwright3	20	1980	100	1400–1500▼	C	0.9	1.2	5.8	1.3	48.1	25.1	1.3	11.0
		Kentucky	20	1980	100	1400–1500▼	C	9.5	0.3	1.3	0.6	25.5	15.9	7.8	32.4
		Spring Montana	20	1980	100	1400–1500▼	C	13.1	0.1	26.5	6.5	18.6	13.5	1.3	4.7
		North Dakota	20	1980	100	1400–1500▼	C	8.3	0.3	22.9	6.7	20.1	11.2	0.5	13.2
1987	Spiro <i>et al.</i> [131]	AMAX	0–15	1900	100	1366►	B	6.7	5.8	3.2	0.0	17.9	11.5	2.9	37.6
		Otisca coal	0–11.5	1900	100	1366►	B	0.5	0.5	11.6	0.0	16.1	23.2	1.1	28.2
	Wenglarz [129]	Ash-fuel 1	10.2	1900	150	1253–1373	C	0.6	1.2	3.8	0.0	12.0	14.2	0.8	20.4
		Ash-fuel 2	8.5	1900	150	1253–1373	C	0.7	1.0	3.4	0.0	11.5	13.9	0.8	21.9
		Ash-fuel 3	14.5	1900	150	1253–1373	C	1.0	0.9	4.7	0.1	7.5	10.9	1.0	23.1
	Kimura <i>et al.</i> [130]	Otisca coal	0–11.5	1900	100	1366	B	0.5	0.5	11.6	0.0	16.1	23.2	1.1	28.2
1984	Raj and Moskowitz [156]	Coal	0–6	1900	244	1144–1422	B	2.2	2.8	0.3	1.1	28.9	29.4	1.7	25.6
		Pittsburg	7	2500	53	1590	C	0.9	1.2	5.8	1.2	47.9	25.0	1.3	10.9
	Anderson <i>et al.</i> [109]	Pittsburg 2	7	2500	149	1590	C	0.9	1.2	5.8	1.2	47.9	25.0	1.3	10.9
		Pittsburg 3	7	2500	215	1590	C	0.9	1.2	5.8	1.2	47.9	25.0	1.3	10.9
*83	Raj [155]	Coal 2	0–6	1900	244	1700–1922	B	2.2	2.8	0.3	1.1	28.9	29.4	1.7	25.6

** The details about the composition are based on the erratum [168]. The powder belongs to the Jim Bridger Power Plant as well as the tests named JBPS A, JBPS B, 1, 2 and 3 but has a slightly different chemical composition. The weight percent values reported in the table were calculated starting from the following molar percentages (SiO₂ 60.2 %, Al₂O₃ 8.17 %, Na₂O 4.3 %, CaO 12.2 %, MgO 3.1 %, TiO₂ 2.7 %, K₂O 1.2 % and Fe₂O₃ 6.6 %).

▼ Temperature range obtained as a function of the distance between nozzle and target.

► Maximum firing temperature

◊ Estimated with Eqs. (25-26)

4.3. Chemical composition

The particle behavior depends on the relationship between particle viscosity and temperature and this is strongly dependent on the chemical composition. Tables 4 – 6 report the chemical composition as a weight fraction of sodium oxide Na₂O, potassium oxide K₂O, calcium oxide CaO, magnesium oxide MgO, silicon dioxide SiO₂, aluminum oxide Al₂O₃, titanium dioxide TiO₂, and iron oxide Fe₂O₃. Obviously, these oxides do not cover the entire composition for each material but these components characterize each ash, powder, and particle determining their physical characteristics.

This wide compositional range is related to the process formation of the ash or powder and might include particles formed from new materials as well as those derived by the fragmentation of pre-existing components which are subjected to degradation or combustion processes. In this context, Srinivasachar *et al.* [29] have carried out combustion and deposition experiments with coal (San Miguel Texas lignite) to assess critical viscosity hypothesis for deposition processes. These experiments have highlighted that final ash composition is independent of combustion conditions and the analysis of individual combustion ash particle have shown that there are negligible interactions between the particles which are characterized by similar final chemical composition. In light of the above, bulk composition can thus provide an overall indication of each particle behavior and its relation between viscosity, temperature, and chemical composition. However, a certain degree of non-uniformity could be represented by the initial formation of liquid phase due to the low temperature eutectic during the particle heating, such as the combination between sodium oxide with silica and aluminum dioxides, that generates a liquid fraction starting from 1200 K. Similar findings are reported in [169], where the presence of sodium sulfate generates a condensed phase that increases the particle sticking capability. This sort of inhomogeneity represents the first phase of particle softening process, that represents one of the most important parameters for estimating the particle adhesion capability. A graphical description of this occurrence can be realized by means of the ternary plot. Figure 9 depicts two different ternary plots according to the triplets Al₂O₃-SiO₂-CaO and SiO₂-MgO-Fe₂O₃ with the indication of the liquidus curves [170] together with the correspondent temperature value. The liquidus temperature can be compared with the temperature value at which the deposition test is carried out. The deposition tests are reported by means of different markers based on the chemical composition reported in Tables 4 – 6. A higher content of silica dioxide corresponds to higher liquidus temperature, and in turn, the deposition test is carried out when particles are not melted

yet. Another element of information that can be drawn, is related to the effects of each oxide on the particle behavior. For example, for the majority of the considered tests reported in Tables 4 – 6, the presence of iron dioxide does not influence the liquidus temperature that can be assumed equal to 1673 K due to the higher presence of silica dioxide. In addition, it can be highlighted that the ash composition of several tested coals occurs in mullite phase field. Mullite is the predominant phase of coal ash which is formed due to kaolinite and other clays decomposition during combustion [171].

With this qualitative data representation (due to the approximation of this data post-process based on only three oxides) it is clear how the correlation between particle composition and temperature could determine different phenomena during the impact process. The different amount of oxide content in each test increase the complexity of the result comparison process and thus, each test condition has to be considered as fundamental information coupled with the particle chemical composition.

The final consideration is related to the literature data. The material characterization is often reported but sometimes it is not complete or, in the worst cases, completely absent. Material characterization is fundamental for calculating physical properties such as viscosity and surface tension which are the most important parameter in the particle adhesion phenomenon. For this reason, in this work, two characterizations related to the volcanic rock, are taken from literature. In details, the composition of Twin Mountain basaltic rock [172] and St. Helens rock [173] are taken from literature. For completeness, in Appendix C, the compositions in term of molar fraction values are also reported.

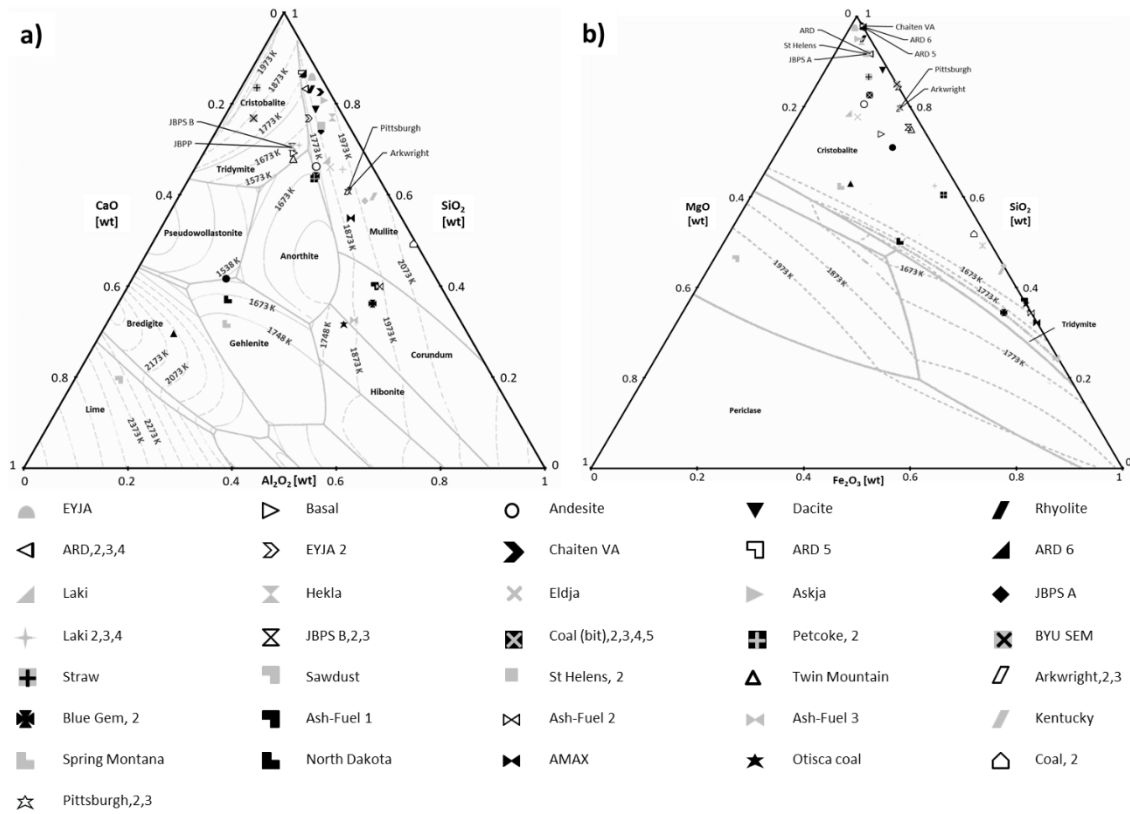


Figure 9 – Ternary diagrams with liquidus curves of the triplets: a) Al_2O_3 - SiO_2 - CaO , and b) SiO_2 - MgO - Fe_2O_3

4.4. Particle size, temperature and mineral/glass ratio

With the reference of the data reported in Tables 4 – 6, it is clear how each test is characterized by several peculiarities, as well as different particle size and temperature. This evidence introduces some critical aspect into the determination of a proper framework under which a useful comparison can be carried out.

According to the contamination source, three families can be recognized such as silty, coal and volcanic particles even if, only the volcanic ash particles, are created by instantaneous and, in many cases, explosive processes. For these reasons, in the literature, detailed analyses are reported in relation to their dimension and material structure. Volcanic ashes are characterized by different fractions of crystals and amorphous solids (juvenile fragments) created during explosive volcanism phenomena. Specific volcanic events (phreatomagmatic eruptions, pyroclastic density currents, and explosive eruptions) determine variations in terms of crystals/volcanic glasses fractions and changes in chemical compositions. The intrinsic structural nature of the ash, comprised of fine fragments of

magmatic glasses, magmatic crystals, and other lithic materials, influences the temperature-dependent material characteristics causing, for example, significant modification in sintering and/or melting conditions of ash particles. This wide variability in chemical and physical ash characteristics makes it difficult to evaluate the behavior of volcanic ash and the proper characterization of the material structure is often tedious due to the structurally complex nature of ash components. Regarding the coal-like particles, a description of the generation of ash particles is reported in [169]. Large particles are formed by the mechanism of coalescence, while fine particles are the result of vaporization and the subsequent condensation of volatile inorganic elements. This implies that a certain degree of inhomogeneity in terms of size and composition can be found after the combustor, but, no detailed analyses are available in this sense, especially related to the combustion process in a gas turbine.

A lack of contaminant characterization in terms of temperature-dependent material characteristics implies hypotheses and unavoidable inaccuracies that should be the main reason for pushing new strategies and tests procedures forward. For example, in volcanic ash analysis, the relation between ash composition and melting temperature (and in turn, ash viscosity) is very difficult to predict in detail [143]. Other contributions [83], [85], and [174], show the influence of the heating rate on the evolution of the wettability and spreading of volcanic ash. More specifically, the wetting efficiency of volcanic ash is dependent on particle size and particle temperature together with mineral/glass ratio [95] and [145]. As reported by [143], these factors are related to the adhesion rate for normal surface incidence.

Regarding the dimension, as mentioned before, non-precise data are reported but, some general consideration can be drawn. It is clear that the adhesion rate is more influenced by a larger particle because its weight is comparable to that of several smaller particles (e.g. one 50 μm particle weighs the same as a thousand 5 μm particles). Particle size also affects the rate at which the particle temperature achieves the substrate temperature: fragments with smaller diameters are capable of reaching more quickly the substrate temperature compared to larger particles and this is at the base of the theoretical effect of heat transfer to different particle sizes [95] and [96]. In this context, the mineral/glass content of the ash can play a key role in the deposition rate. When glass transition temperature is reached, most of the amorphous (glassy) particles are expected to rapidly become very soft promoting the particle adhesion phenomenon. Finally, the mechanical properties are related also to the particle diameter. As reported in [175], the particle Young modulus may increase when particles are smaller. In particular, in [175] an exponential dependence of the particle Young modulus on the grain size is reported due to the fact that, when the particle is small, the material structure is less affected by inhomogeneity and defects.

All of these effects affect the experimental results carried out over the years and, in turn, influence the present data post-process. By contrast, given the number of tests which involve several materials, particle sizes and test conditions, can be concluded that the present data post-process can be considered robust against these effects within a certain tolerance band, allowing the comprehension of the particle deposition phenomenon based on per order of magnitude considerations.

5. PARTICLE STICKING MODELS AND VISCOSITY METHODS: MUTUAL INTERACTION AND CRITICAL ANALYSIS

The previous analysis has shown that the deposition tests listed in Tables 4 – 6 are carried out with temperature values lower than liquidus temperature and, thus, they are characterized by semi-molten particles which impact on a solid surface. For this reason, the measurement of the particles viscosity is not straightforward and, it implies several difficulties. Figure 10 shows the iso-viscosity contour plot based on the ternary plots of the triplet Al_2O_3 - SiO_2 - CaO and gives the possibility to compare the collected data with the viscosity values measured at 1773 K [170]. The regions not covered by the iso-viscosity lines are due to the lack of literature data and, in some instances the presence of solid matter (higher content of silica dioxide). Despite the fact that this qualitative representation is not useful for carrying out the analysis of the deposition process (the temperature value is constant and higher than the experimental particle temperature), it gives the opportunity to highlight how the particle chemical composition influences the particle impact behavior. By a slight modification of mass fraction oxide content, the particle viscosity changes by an order of magnitude for the same temperature value.

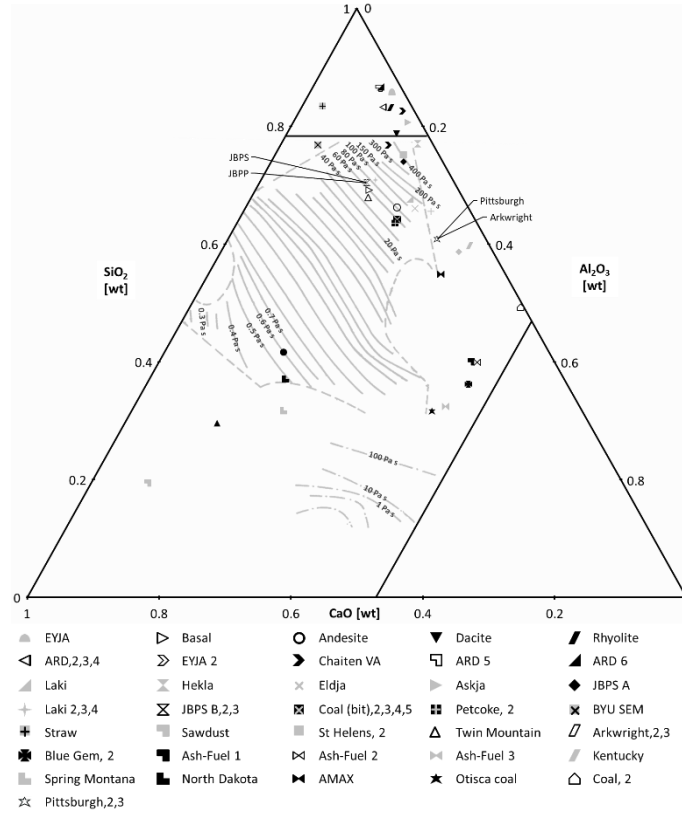


Figure 10 – Iso-viscosity [Pa s] contour of CaO-Al₂O₃-SiO₂ at 1773 K

5.1. Particle viscosity: quantification and model application

Based on the chemical composition of the material, in this section, the particle viscosity is calculated as a function of the temperature. Using the listed models (NPL [69], S² [70], WF [71], S&T [72], RRLG [73], SDS [74] and GRD [75]) it is possible to calculate the viscosity values as a function of the material composition and temperature. This allows the comparison between different tests (carried out with different materials and temperature) in terms of viscosity. The viscosity values are calculated for all materials reported in Tables 4 – 6 following the models reported.

As mentioned, based upon the viscosity model analysis (reported in details in Appendix A) the NPL model works with all the considered materials due to the absence of specific applicability limits (in terms of chemical composition) allowing for the comparison among the deposition tests without restrictions. Due to this, for the cross-comparison between the viscosity model reported in the following paragraph, the NPL model represents a sort of reference giving the chance to compare several models (applied according to their applicability limits) with respect to the same reference values. For each analysis, all the viscosity models which are suitable (in terms of particle composition) for the analysis are used, in order to improve the completeness of the present data post-process.

Based on viscosity calculation and by applying the critical viscosity method, it is possible to define the capability of each particle to adhere to the surface, by comparing the instantaneous particle viscosity and the critical viscosity value. The critical viscosity values could be calculated using one of the reported viscosity models, where the particle temperature corresponds to the softening temperature T_{soft} . According to Eqs (19 – 23), the particle softening temperature is calculated according to the materials compositions. Even if in some instances the particle softening temperature is reported, in order to compare all tests under the same conditions, the particle softening temperature is calculated for all tests. Table 7 shows the softening temperature for all materials listed in Tables 4 – 6.

Therefore, starting from the particle characteristics, it is now possible to compare the viscosity ratio (μ/μ_c) trends at the critical condition related to the sticking model. Figure 11 reports the variation of the particle viscosity ratio (μ/μ_c) as a function of the temperature, according to the NPL model, while Figure 12 reports the viscosity prediction according to the different models (S² [70], WF [71], S&T [72], RRLG [73], SDS [74] and GRD [75]). Each model is applied within its validity limits. According to the critical viscosity method, two regions for each material can be defined according to the viscosity ratio (μ/μ_c) identifying the sticky and rebound conditions. As can be seen in Figure 11, experimental tests are mainly conducted in the sticky regions excluding a few cases in which the results of test conditions lie inside the rebound region due to the lower particle temperature of deposition tests. State the analysis of Figure 11 and Figure 12, it is clearly visible the immense variability in the viscosity obtained for the same substance from different

models and also that, using such widely different values will result in contrasting predictions if different sticking models are applied. For the sake of completeness, the viscosity values as a function of the particle temperature are reported in Appendix D, with the use of similar plots of Figure 11 and Figure 12. Appendix D reports several data related to the material type and contaminant sources used for the materials listed in Tables 4 – 6 and, in addition, the critical viscosity value is shown for each test as a function of the viscosity model.

Table 7 – Values of particle softening temperature obtained according to Eqs (19 – 23) compared with literature (if available)

Material	T_{soft} [K] Eqs (19–23)	T_{soft} [K] (literature)	Material	T_{soft} [K] Eqs (19–23)	T_{soft} [K] (literature)	Material	T_{soft} [K] Eqs (19–23)	T_{soft} [K] (literature)
EYJA	1445	-	JBPS A	1329	-	Twin Mountain	1176	-
Basalt	1170	-	Laki 2, 3, 4, 5	1132	873 973	Arkwright, 2, 3	1337	1589
Andesite	1257	-	JBPS B, 2, 3	1197	1422*	Blue Gem, 2	1191	1581
Dacite	1284	-	JBPP	1172	1500	Ash-fuel 1	1169	-
Rhyolite	1387	-	Lignite	1032	-	Ash-fuel 2	1162	-
ARD, 2, 3, 4	1337	-	Bituminous	1030	-	Ash-fuel 3	1118	-
EYJA 2	1305	1123 – 1323	PRB	909	-	Kentucky	1162	-
Chaiten VA	1446	1123 – 1323	Coal (bitum.), 2, 3, 4, 5	1278	1278**	Spring Montana	1068	-
ARD 5	1465	-	Bituminous mean14	1030	-	North Dakota	1021	-
ARD 6	1471	-	Petcoke, 2	1162	-	AMAX	1084	-
Laki	1258	923	BYU SEM	1071	-	Otisca coal	1179	-
Hekla	1394	1023	Straw	1213	-	Coal, 2	1320	-
Eldgja	1341	973	Sawdust	842	-	Pittsburgh, 2, 3	1337	1589
Askja	1161	973	St Helens, 2	1323	-			

*called critical sticking temperature

**estimated by [120] by using Yi et al.'s model [88])

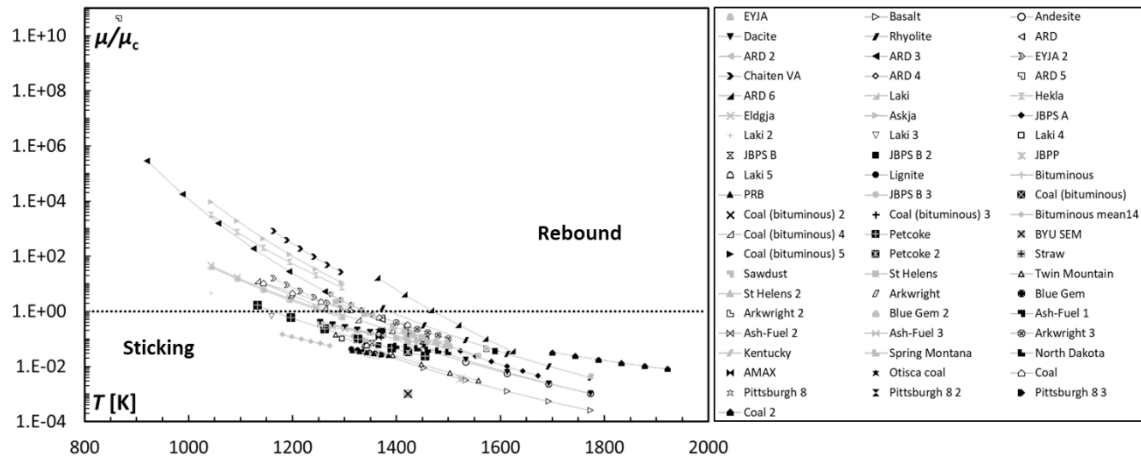


Figure 11 – Critical viscosity method (rebound and sticking regions are divided by the dashed line) calculated according to the NPL model

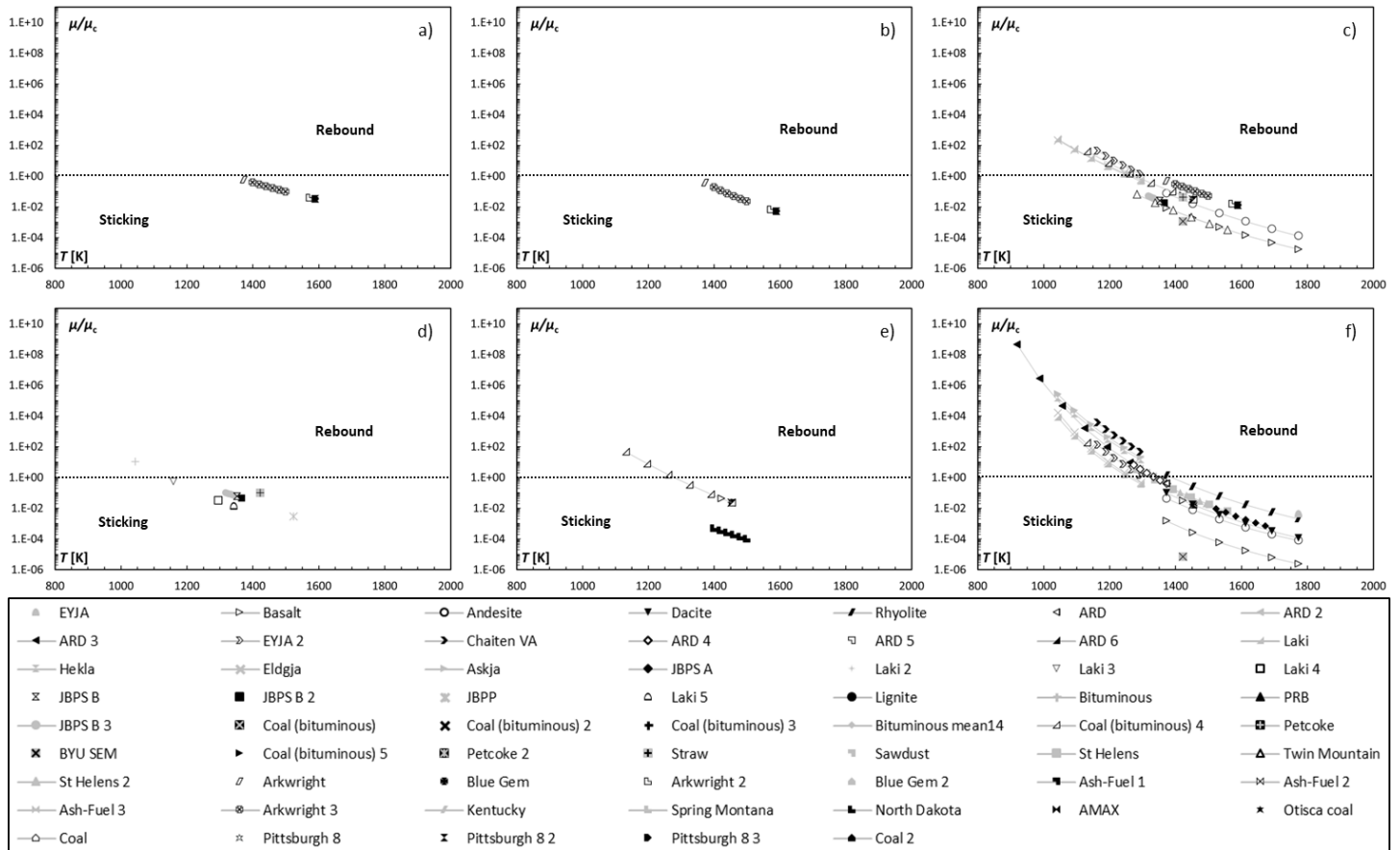


Figure 12 – Critical viscosity method (rebound and sticking regions are divided by the dashed line: a) S^2 , b) WF, c) S&T, d) RRLG, e) SDS and f) GRD

In details, the following analysis reports a distinction between the tests according to the viscosity method. At the same time, the softening temperature is calculated with the same aforementioned model proposed by Yin et al. [88]. The first analysis, reported in Figure 13 and Figure 14, shows silty and coal particle tests respectively. The marker shape indicates the test while the color indicates the viscosity method. In this case, silty particle tests mainly belong to the rebound region, while coal particle tests are located in the sticky region even if, some of these tests are conducted with the same temperature as silty tests. This difference is due to the different relationship between particle viscosity and temperature generated by the different chemical compositions. As reported by [84], differences in chemical composition must be taken into account and the similarities between different particle impact tests have to be drawn considering these differences. Therefore, the use of ARD particles instead of coal particles for carrying out experimental tests in laboratory test facilities could generate several mismatches with respect to the actual applications. Figure 13 and Figure 14 show, in addition, the different viscosity ratio (μ/μ_c) predictions provided by the viscosity methods. The variations between the NPL model and the GRD and S&T models increase towards lower temperature. In addition, the NPL predictions appear more close to the critical value ($\mu/\mu_c=1$) than other models. Considering the comparison reported in Figure 15, it can be noted that predictions are not aligned with the straight dashed line (provided as a reference for the reader), but the trends change according to the tests and according to the viscosity ratio μ/μ_c . For high values of viscosity ratio, NPL and GRD model predictions (see Figure 15a) are very different (several orders of magnitude), while, across the critical point (see Figure 15a and b), the predictions appear similar even if characterized by different slopes. A detailed description of the relations between the viscosity method, sticking model and particle characteristics will report in the following sections.

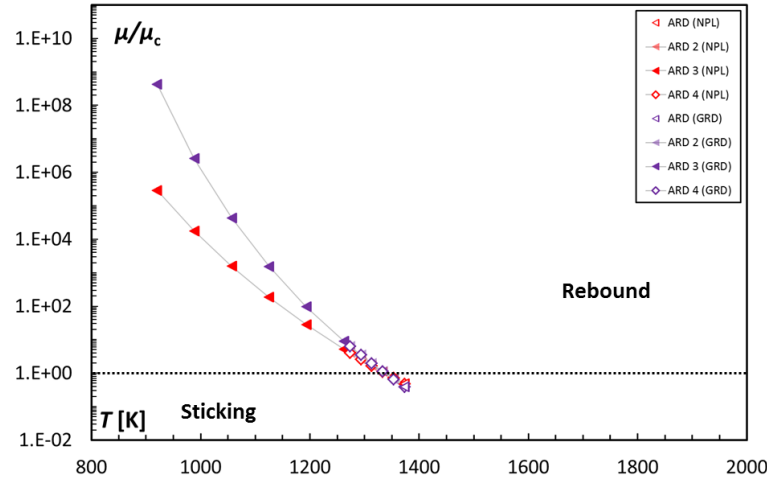


Figure 13 – Critical viscosity method for silty particles (four tests with ARD) calculated according to the NPL and GRD models

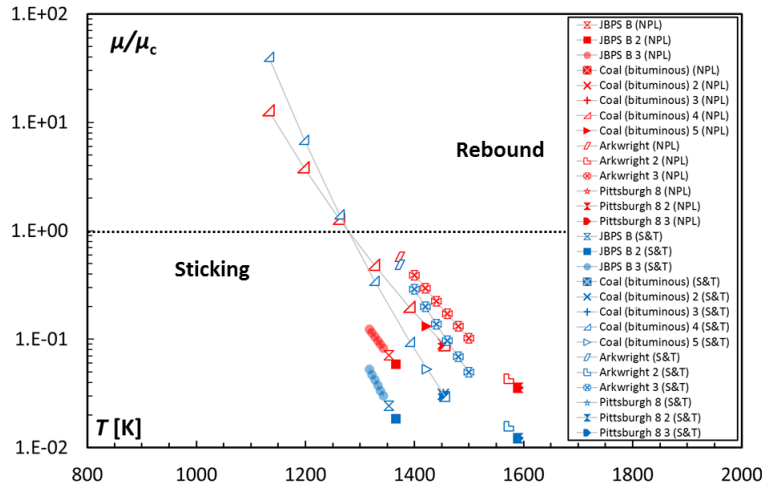


Figure 14 – Critical viscosity method for coal particles (three tests with JPBS B, JBPP, five tests with Coal (bituminous), three tests with Arkwright and three tests with Pittsburg particles) calculated according to the NPL and S&T models

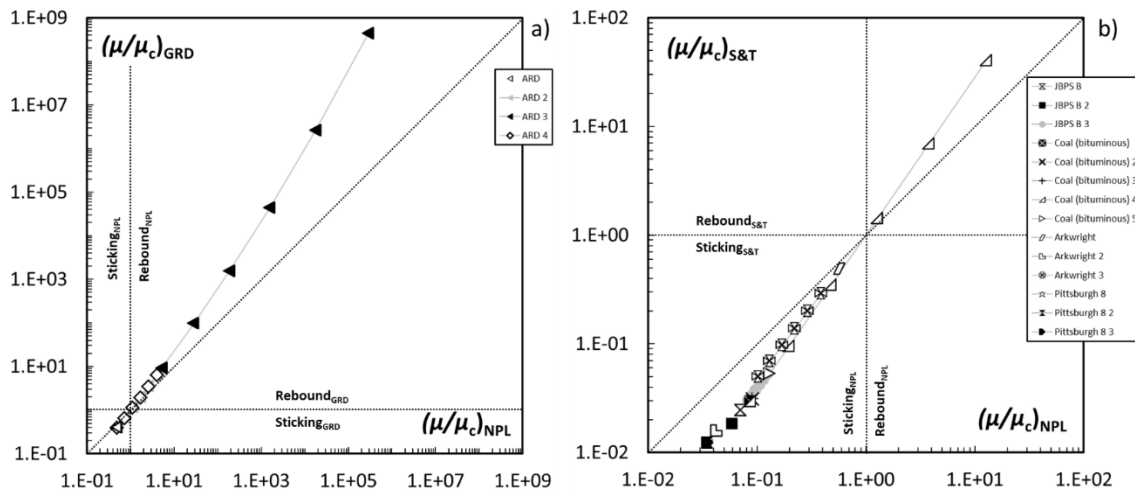


Figure 15 – Comparison of the critical viscosity ratio (μ/μ_c): a) NPL and GRD models for silty particles and b) NPL and S&T models for coal particles. The straight dashed line allows the data comparison

Given that there have been a considerable number of tests of volcanic ash deposition, a dedicated analysis is carried out. The viscosity method proposed by Giordano *et al.* [75] is expressly based on several volcanic ash samples (see Appendix A for completeness) and, in this section, it will be compared with the more general method proposed by Mills and Sridhar [69].

According to the chemical classification proposed in [176], Figure 16 reports the Total Alkali-Silica (TAS) diagram with the superimposition of the fourteen (14) volcanic ashes considered in this review. The TAS classification can be used to categorized volcanic rocks based upon the relationships between the alkali and the silica contents. This distinction, that represents the relative proportions of alkalis and silica which are fundamental for an easier determination of the volcanic mineralogy based on the chemical composition. This classification was firstly reported in [176] with the endorsement of the International Union of Geological Sciences (Subcommission of the Systematics of Igneous Rocks).

Tests can be classified according to six (6) different categories called basalt, basaltic-andesite, dacite, rhyolite, basaltic trachy-andesite, and trachydacite. These subalkaline series are characterized by a lower amount of alkali and a progressive increase in silica dioxide content and are included in the GRD model limits.

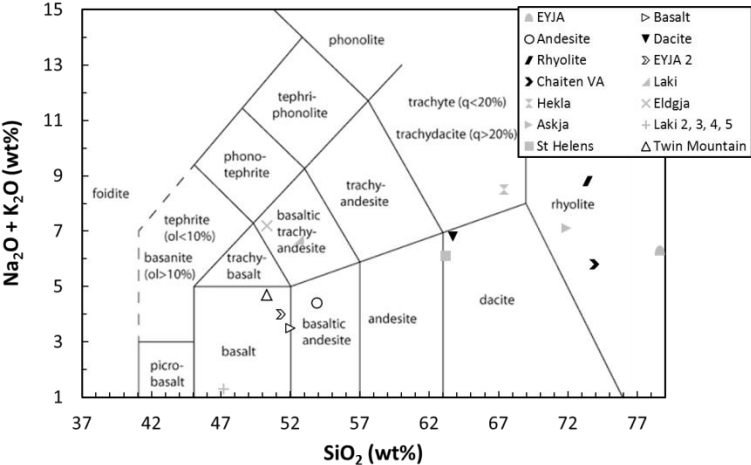


Figure 16 – Classification of volcanic tests according to the TAS diagram

Figure 17 reports the viscosity ratio as a function of the temperature for volcanic ashes using the GRD and NPL models. Thirteen (13) tests out of seventeen (18) are shown. Laki 2, 3, 4 and 5 and Twin Mountain tests are characterized by a particle composition out of the validity range indicated by Giordano *et al.* [75]. In a different way of coal particles, about half of these tests belong to the sticky region. As mentioned above, by using different viscosity prediction models, the viscosity ratio (μ/μ_c) can vary noticeably, but the mutual variation between NPL and GRD methods appears very similar to those reported for silty and coal particles (see Figure 13 and Figure 14). This means that even if the GRD model is based only on volcanic ash materials (by means of a data regression, as reported in Appendix A), it performs similar prediction, in comparison with the NPL model, even for the material derived from different sources (silty and coal particles).

Figure 18 shows the comparison between the critical viscosity ratio calculated according to the NPL and the GRD viscosity models. Sticking and rebound regions are superimposed onto the graph dividing the two regions as a function of the viscosity model. The comparison highlights how the choice of the viscosity model affects the particle adhesion prediction. It can be noted that predictions are not aligned with the straight dashed line (provided as a reference for the reader), but the trends change according to the tests and according to the viscosity ratio μ/μ_c . This evidence has to be matched with the trends reported in Figure 17: by changing the test temperature by 50 K, the particle viscosity may change by an order of magnitude and, by considering the different relation between viscosity and temperature, this could imply different predictions in terms of a particle sticking or rebound.

This analysis shows how important the correct estimation of particle temperature is, as well as the choice of the viscosity and sticking models in the prediction of particle adhesion.

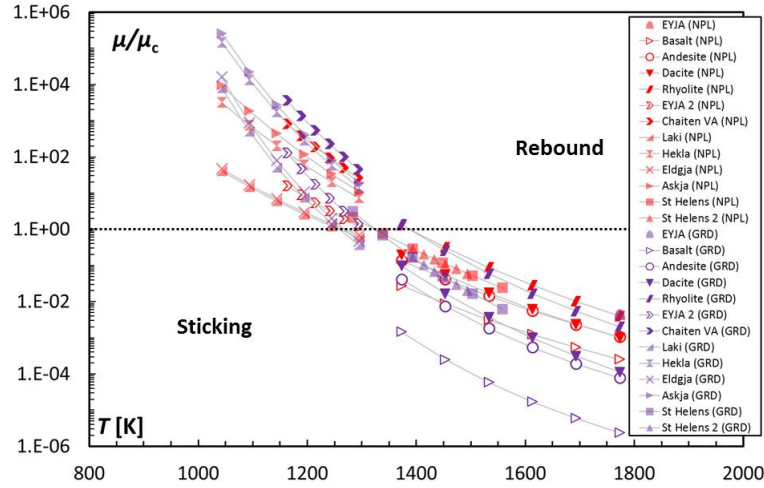


Figure 17 – Critical viscosity method for volcanic ash particles calculated according to the NPL and GRD models

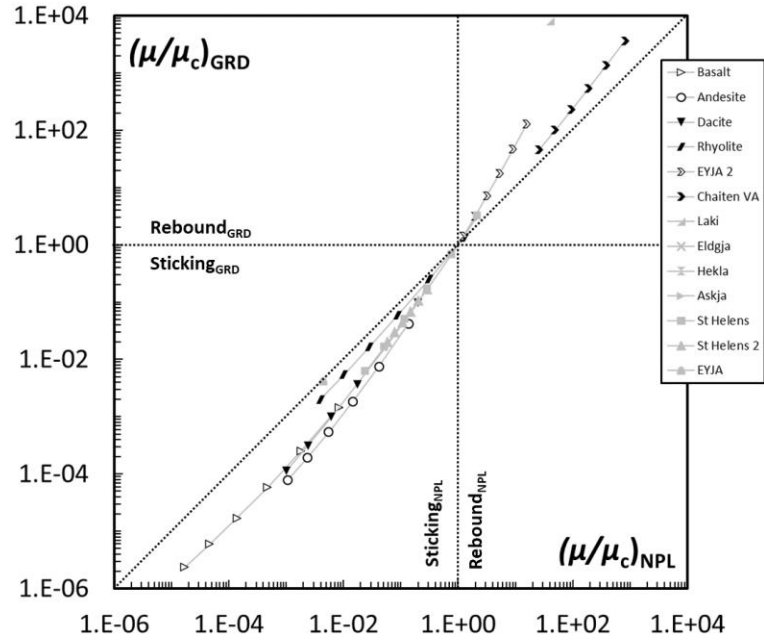


Figure 18 – Comparison of the critical viscosity ratio (μ/μ_c) calculated according to the NPL and GRD viscosity models where straight dashed line allows the data comparison

5.2. Particle velocity: application of the critical velocity method

In line with the viscosity analysis, it is possible to apply the critical velocity method defining the rebound/adhesion regions. This analysis is carried out using Eq. (16) for the calculation of the Young modulus and using Eq. (15) as a reference. This relation is used in literature for both ash contaminants [36] and JBPS B 2 particles [23]. The Young modulus of the surface is set equal to 200 GPa, while the Poisson coefficient is equal to 0.3 for both particle and surface. The Young modulus for the particle is calculated according to Eq. (14) that is suitable for coal-ash contamination. Figure 19 shows the comparison between a representative test (JBPS B 2) condition at $v = 79$ m/s and the consequent critical velocity. The dashed line in the picture is representative of the particle velocity used in the tests and the critical velocity is reported as a function of temperature and diameter. In this case, the overall range of particle diameter (2 – 20) μm , instead of the mass mean average diameter equal to 11.6 μm has been considered. In the same way, temperature values in the range of 1273 K – 1373 K instead of single temperature value equal to 1366 K have been considered for the analysis. This assumption is based on the experimental evaluations reported in [151]. The Authors in [151] reported the temperature map across the vane, showing a non-uniform temperature pattern. If the particle velocity is lower than the critical velocity value, the particle is able to stick to a surface.

Taking into consideration the critical velocity trends, for a given particle diameter, the particle velocity ranges for which the particle is able to stick increases according to temperature values. This trend is related to Young modulus variation with temperature (see Eq.

14). Analogous results can be obtained by fixing particle temperature and decreasing particle diameter. In this case, the critical velocity value is inversely proportional to the particle diameter (see Eq. 15).

As can be predicted by the critical velocity model, particle adhesion occurs in the case of smaller diameter and higher temperature values. In this case, according to the critical velocity model, several experimental conditions lie outside the adhesion region. In this case, the actual non-uniform temperature pattern, instead of the single value taken as the reference for this test, shows how for a single adhesion test, different predictions may occur as a function of the local flow conditions.

Critical velocity model takes into account particle diameter while the classic formulation of the critical viscosity model accounts only for the particle temperature and its composition. In literature, several analyses show that increasing particle diameter the average sticking coefficient decreases, probably due to a not-complete particle heating during the experimental tests [150]. Analytical observations have highlighted the influence of surface temperature [34]. In particular, in presence of blade cooling, the sticking coefficient decreases due to the increment of the Young modulus (molten particle starts to solidify).

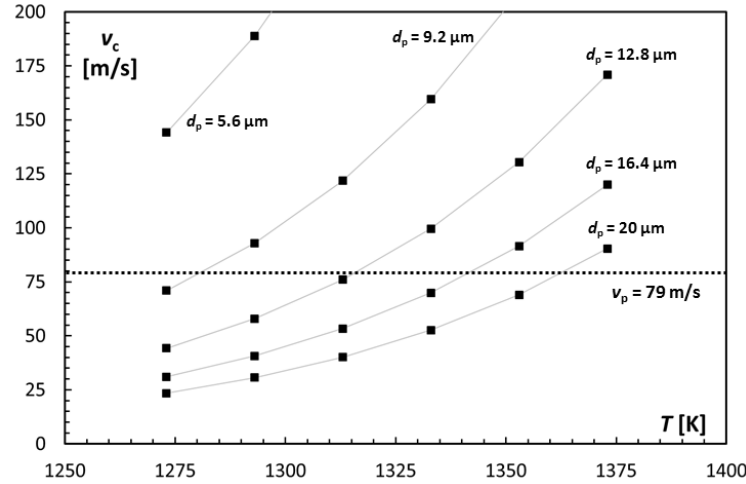


Figure 19 – Application of the critical velocity method for JBPS B 2. Sticky conditions refer to the case when particle velocity v_p is lower than the critical velocity value

5.3. Energy-based model: particle spread factor and overall comparison

The last analysis related to particle adhesion/rebound using literature sticking model refers to the energy-based model. This model is based on the estimation of particle deformation during the impact and its correspondent energy balance between the dissipative and conservative forces. The peculiarity of this approach is related to the estimation of particle deformation as a consequence of the impact. Beyond the target characteristics (such as elasticity, hardness, surface roughness, etc.), one of the major challenges is represented by the identification of the particle condition (such as solid particle, liquid particle or semi-molten particle) upon impact. As reported in the literature [177] the deformation process is strongly dependent to the particle/droplet viscosity and surface tension.

5.3.1 Particle surface tension

Figure 20 reports the variation of the particle surface tension as a function of the temperature according to the material reported in Tables 4 – 6. Therefore, each trend includes the particle surface tension variation due to the composition and temperature, while, each dot provides the particle surface tension value fixing both temperature and composition when that material is tested at a fixed temperature. The particle surface tension values are estimated in agreement with Eq. (24) and the model coefficient collected in Table 2. In the same fashion as seen for viscosity, particle surface tension values decrease according to the temperature even if, the variation over the temperature range is lower. The majority of data are comprised within 0.35 N/m to 0.45 N/m.

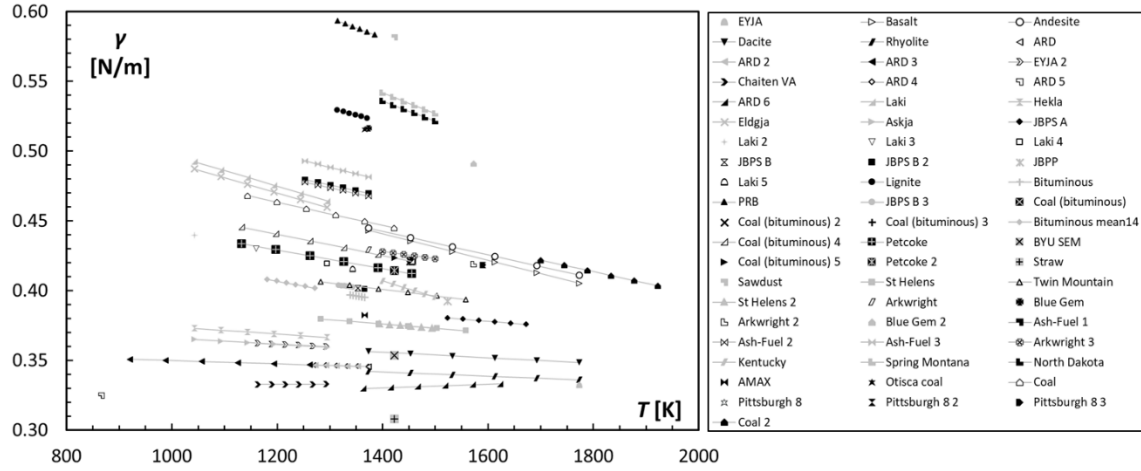


Figure 20 – Particle surface tension as a function of particle temperature

5.3.2 Particle spread factor analysis

Several types of research are devoted to model the particle/droplet deformation process by means of the non-linear relationship between non-dimensional numbers such as We and Re and the contact angle realized on the target. As demonstrated by Kleinhans et al. [43] relationship derived from droplet impact [50] could be used for representing semi-molten particle impact, successfully. In particular, in [43], the sticking behavior of soda lime glass particles are well represented using the non-linear equation reported in [50] obtained for water mixture with a viscosity value in the range (1–100) mPa s. Starting from this result, in this section, a collection of the relationships able to model the particle deformation process are reported. In order to give an overall overview how these models tackle the problem of semi-molten particle impact, six (6) relationships are used to calculate the particle spread factor for three (3) representative tests taken from Tables 4 – 6, named ARD 2 (sandy particle), Eldgja (volcanic particle) and Coal (bituminous) 4 (coal particle) are considered.

Spread correlations available in the literature refer to the different type of fluid/semi-molten substances and, as reported in [177] are characterized by some limitations. Most of these are related to the difficulties of scaling the complex interactions of liquid properties, surface wettability, dynamic contact angle and liquid velocity implying several difficulties to extend the validity beyond the fluid tested. Unfortunately, all the models available in the literature are based on studies of droplet impact having viscosity values lower than that involved in the present study. For example, very low viscosity fluid (3.9e-5 Pa s) was used by Jones [46] taken inspiration from the Madejski's model [178] characterized by higher viscosity value (about 1 Pa s). Other models as Pasandideh-Fard et al. [47] and Ukiwe and Kwok [48] are based on experimental results obtained with droplet water. Similar fluid viscosity (n-heptane) is adopted also by Chandra and Avedisian [49] while, fluids with higher viscosity values, are used by Mao et al. [50] (fluid viscosity equal to 100 mPa s) and Sheller and Bousfield [51] (fluid viscosity equal to 300 mPa s). Table 8 shows the non-linear equations used for calculating particle spread factor for the three (3) considered experimental tests. As reported, each equation depends on non-dimensional numbers (particle Reynolds and/or Weber numbers) and, in some cases, on the contact angle θ assumed equal to $\pi/2$ in the present study.

Table 8 – Non-linear equations for particle/droplet spread factor calculation

Author	Equation	Characteristics of liquid
Jones [46]	$\xi = \left(\frac{4}{3} \text{Re}^{0.25} \right)^{0.5} \quad (27)$	Viscosity equal to 3.9e-5 Pa s
Pasandideh-Fard et al. [47]	$\xi = \left(\frac{\text{We} + 12}{3(1 - \cos\theta) + 4\text{We} \text{Re}^{-0.5}} \right)^{0.5} \quad (28)$	Water
Ukiwe and Kwok [48]	$(\text{We} + 12)\xi = 8 + (3(1 - \cos\theta) + 4\text{We} \text{Re}^{-0.5})\xi^3 \quad (29)$	Water
Chandra and Avedisian [49]	$\frac{3\text{We}}{2\text{Re}} \xi^4 + (1 - \cos\theta)\xi^2 - \left(\frac{1}{3} \text{We} + 4 \right) = 0 \quad (30)$	N-heptane
Mao et al. [50]	$\left(\frac{1 - \cos\theta}{4} + 0.2 \frac{\text{We}^{0.83}}{\text{Re}^{0.33}} \right) \xi^3 - \left(\frac{\text{We}}{12} + 1 \right) \xi + \frac{2}{3} = 0 \quad (31)$	Viscosity up to 100 mPa s
Sheller and Bousfield [51]	$\xi = 0.91(\text{Re} \text{We}^{0.5})^{0.133} \quad (32)$	Viscosity up to 300 mPa s

According to the relations reported in Table 8, Figure 21 and Figure 22 show the spread factor trend as a function of particle diameter and particle viscosity, respectively. In order to simplify the analysis, particle viscosity is calculated according to the NPL model, only. Each figure reports the results obtained for the three considered tests (ARD 2, Eldgja and Coal (bituminous) 4). Taken into consideration Figure 21, trends appear very similar for particle diameter higher than 20 μm , even if, the spread factor values are widespread. In the case of smaller diameter, the trend provided by Jones [46] deviates significantly with respect to the other. Therefore, in the case of small particle diameter, data dispersion is greater and the prediction of particle spread factor become more affected by the selection of the spread factor model.

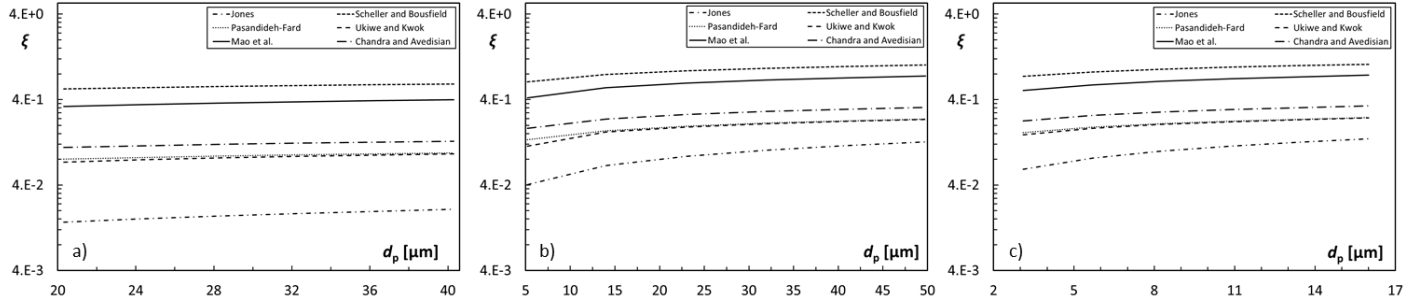


Figure 21 – Particle diameter sensitivity analysis: a) ARD 2, b) Eldgja, and c) Coal (bituminous) 4

Similar evidence can be found by considering the sensitivity analysis reported in Figure 22. In this case, spread factor values are shown as a function of the particle viscosity values, and, it is visible that for lower particle viscosity, the model predictions of particle spread factor values are very close to each other (see Figure 22c, for example). Moving towards higher viscosity values, the data appear very dispersed highlighting the variation of the slope among the models (see Figure 22a). The trends ξ/μ appear very different from each other and it is in the opposite way than that reported in Figure 21, where, the ξ/d trends show very similar slopes. This result derives from the relationship between particle spread factor and the non-dimensional numbers Re and We (see Table 8). Particle viscosity contributes only to the particle Reynolds number while particle diameter contributes in both characteristic numbers (Re and We). This implies that, from a particle deformation estimation point of view, the variation of particle viscosity is more detrimental than particle diameter. Taking into consideration the analyses reported in Figure 21 and Figure 22, trends can be identified and correlated with the droplet characteristics used for obtaining model equations (Eqs 27 – 32), reported in Table 8). Models based on liquid droplet characterized by lower viscosity (Jones [46], Pasandideh-Far et al. [47] and Ukiwe and Kwok [48]) predict lower particle spread factor values than the other models, which are obtained with higher droplet viscosity.

The energy-based models are built on the definition of a particle spread factor threshold value ($\xi=0.4$ for the present work, see Figure 4 for the full explanation), and with the reference of particle sticking phenomenon, different spread factor models give a different prediction of particle deformation for the same particle in the same impact conditions. According to the energy-based model, for a particle spread factor ξ equal or less than 0.4, particle sticks to the surface, otherwise, it bounces. On the basis of these analyses, the model prediction of particle spread factor plays a key role when particle sticking prediction is based on the estimation of the energy dissipation provided by the particle deformation during the impact. Therefore, with this approach, particle sticking prediction is affected by (i) the model assumptions related to the spread factor equation and, taking into consideration also the estimation of particle viscosity and surface tension, (ii) the models used for estimating the particle characteristics upon the impact.

In the following sections, the model of Mao et al. [50] is taken as a reference for analyzing the literature results, comparing the spread factor values with a threshold value ($\xi=0.4$). As reported by Kleihnas et al. [43], Mao et al.'s [50] model is able to well-recognized particle sticking in the case of high viscous substance (e.g. soda lime glass particle).

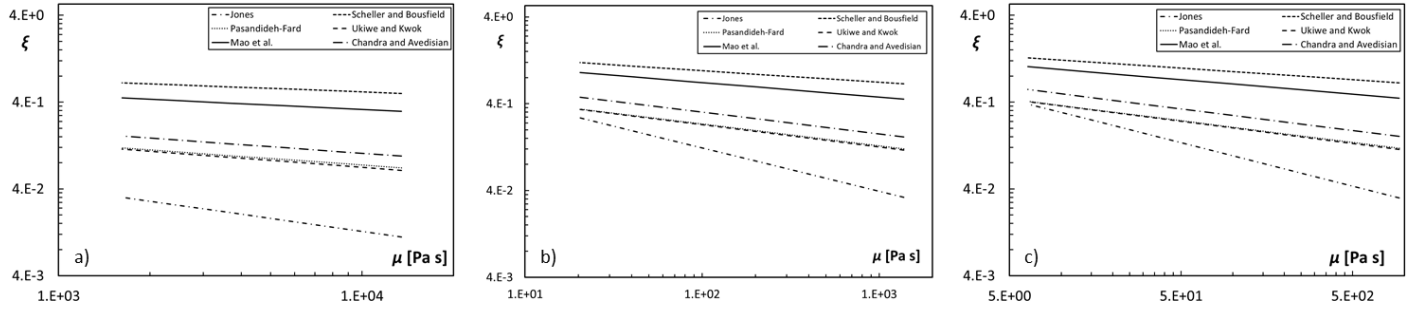


Figure 22 – Particle viscosity sensitivity analysis: a) ARD 2, b) Eldgja, and c) Coal (bituminous) 4

5.3.3 Spread factor values

Starting from the particle Reynolds number and particle Weber number and using Eq. (31) it is possible to calculate the correspondent spread factor for each deposition test. To perform this, the particle surface tension has to be calculated according to the Eq. (24) with the reference of Table 2. Based on the derived particle surface tension values, Figure 23 reports a three-dimensional variation of the spread factor as a function of We and Re for a representative fixed value of contact angle [50] equal to 90° . In Figure 23, red and black dots represent all the data reported in Tables 4 – 6. The threshold value of the spread factor ($\zeta = 0.4$) is marked with a white line that divided the grey region from the pale-grey region. The grey region represents the sticking region ($\zeta \geq 0.4$) in which the red dots represent the energy-based model prediction in agreement with the literature deposition tests, while the pale-grey region represents the rebound region ($\zeta < 0.4$) in which the black dots represents the energy-based model prediction in disagreement with the literature deposition tests. Therefore, some deposition tests belong to the rebound region instead of the sticky region. In this case, particle diameter, velocity, and temperature are the main contributors in the to spread factor values. The three-dimensional surface We-Re- ζ shows, in correspondence of lower values of particle Weber number, a curvature variation due to the roots of the cubic relation reported in Eq. (31).

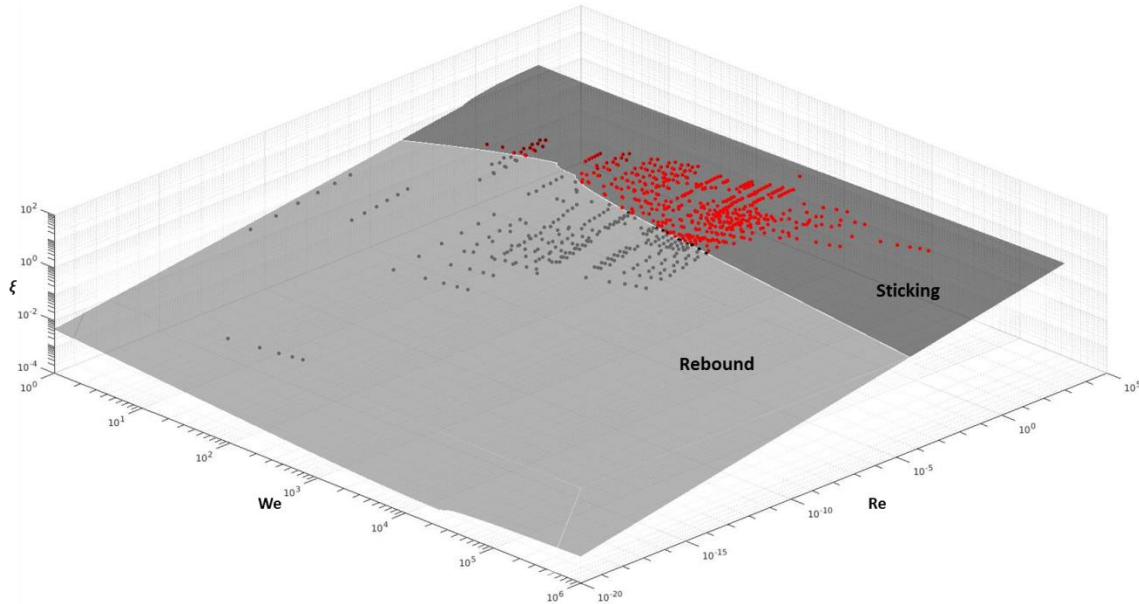


Figure 23 – Application of the energy-based model. Sticky conditions refer to the case when particle spread factor ζ is higher than 0.4. Particle viscosity is calculated according to the NPL model

5.4 Comparison between critical viscosity and energy-based sticking models

The comparison proposed in Figure 24 is related to the critical viscosity method and the energy-based model calculated according to the NPL viscosity model. Trends are related to a fixed particle diameter and particle temperature variation (if present) that implies the contemporary variation of particle viscosity and spread factor values. The trend lines report the variation of particle spread as a function of the viscosity for a fixed particle diameter. In some cases, experimental tests are conducted with a certain particle diameter dispersion with a constant temperature value. In this case, no trend-lines are depicted because no-relation between particle spread and particle viscosity depend on the diameter.

The data summarized in Figure 24 are subdivided according to two lines: the vertical line divides rebound/adhesion regions according to critical viscosity method while the horizontal line divides rebound/adhesion regions according to energy-based model.

From the comparison, it is clear the difference in the particle sticking prediction related to these models. From the present subdivision, two regions could be clearly detected according to the two models. The adhesion region is recognized using the simultaneous conditions of $\mu/\mu_c < 1$ and $\xi \geq 0.4$ for which both methods predict adhesion as a result of the particle impact. The other region, characterized by $\mu/\mu_c > 1$ and $\xi < 0.4$, is the region of particle rebound. For the other two combinations ($\mu/\mu_c > 1$; $\xi \geq 0.4$ and $\mu/\mu_c < 1$; $\xi < 0.4$) the two models are in disagreement, showing opposite predictions. It can be remarked that all data collected in Tables 4 – 6 refer to experimental tests showing particle adhesion.

The overall analysis of the $(\mu/\mu_c ; \xi)$ trends is reported in Figure 25 where the viscosity ratio and the spread factor values are calculated according to the other six viscosity models considered (S^2 [70], WF [71], S&T [72], RRLG [73], SDS [74] and GRD [75]). As highlighted, different viscosity models predict different results (see for example the test called Arkwright and Arkwright 3 with the reference of Table 6) that could differ from sticking to rebound results (see the predictions of S^2 and WF).

Therefore, the analyses reported in Figure 24 and Figure 25 show the effects of the viscosity model on the particle sticking probability as a function of particle composition. For example, looking at the ARD tests, three different compositions (ARD, 2, 3, 4 with respect to ARD 5 and ARD 6 tests, for details see Table 4,) characterized by a high value of silica dioxide comprises in the range of (72.8 – 85.0) wt% are available for the comparison. In addition, due to the preparation processes (e.g. filtration), different particle diameter ranges characterize the literature value. Several tests belong to the rebound region for which both sticking models fail the prediction. In particular, even if the ARD and ARD 6 tests are conducted with the same particle temperature 1373 K and 1363 K respectively, the viscosity ratio is one order of magnitude different. The ARD 6 particles are characterized by a higher silica dioxide content that reflects in higher softening temperature (see Table 7).

This mismatch between the actual experimental results and the model prediction can be explained with two reasons: (i) the sticking models are not able to represent all of the ARD deposition tests and/or (ii) for a specific test, the deposits are generated by a certain combination of particle diameter, temperature, and velocity. Therefore, even if the particle impact tests give particle adhesion, this results could be generated by a small portion of powder (in term of diameter) or by specific flow conditions (in term of temperature). In the next sections, a detailed analysis of their mutual interaction is proposed according to material composition.

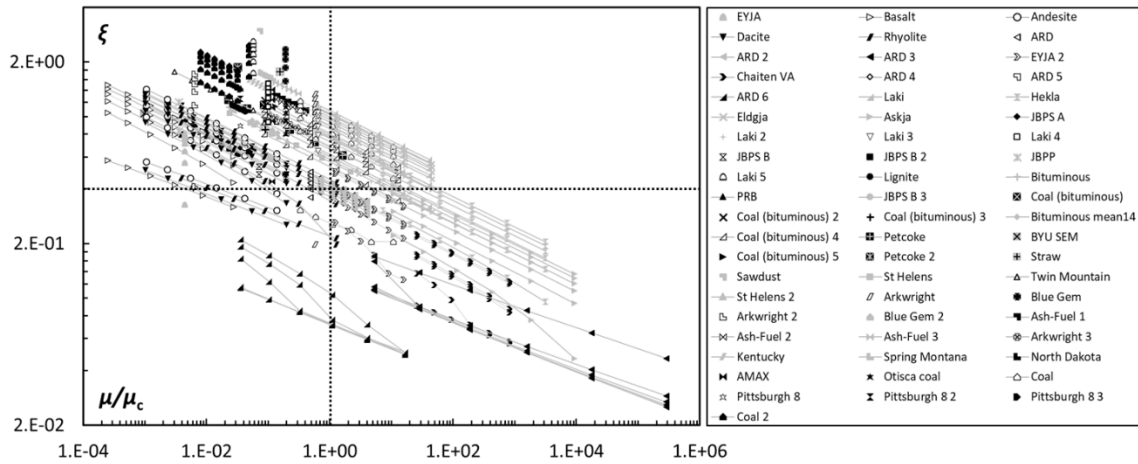


Figure 24 – Model comparison critical viscosity/energy-based (data obtained using the NPL model). The vertical line divides rebound/adhesion regions according to critical viscosity method while the horizontal line divides rebound/adhesion regions according to energy-based model (for easier visualization of the chart, ARD 5 tests (characterized by $\mu/\mu_c = 4.1 \times 10^{16}$ and $\xi = 0.010 - 0.004$) are not shown)

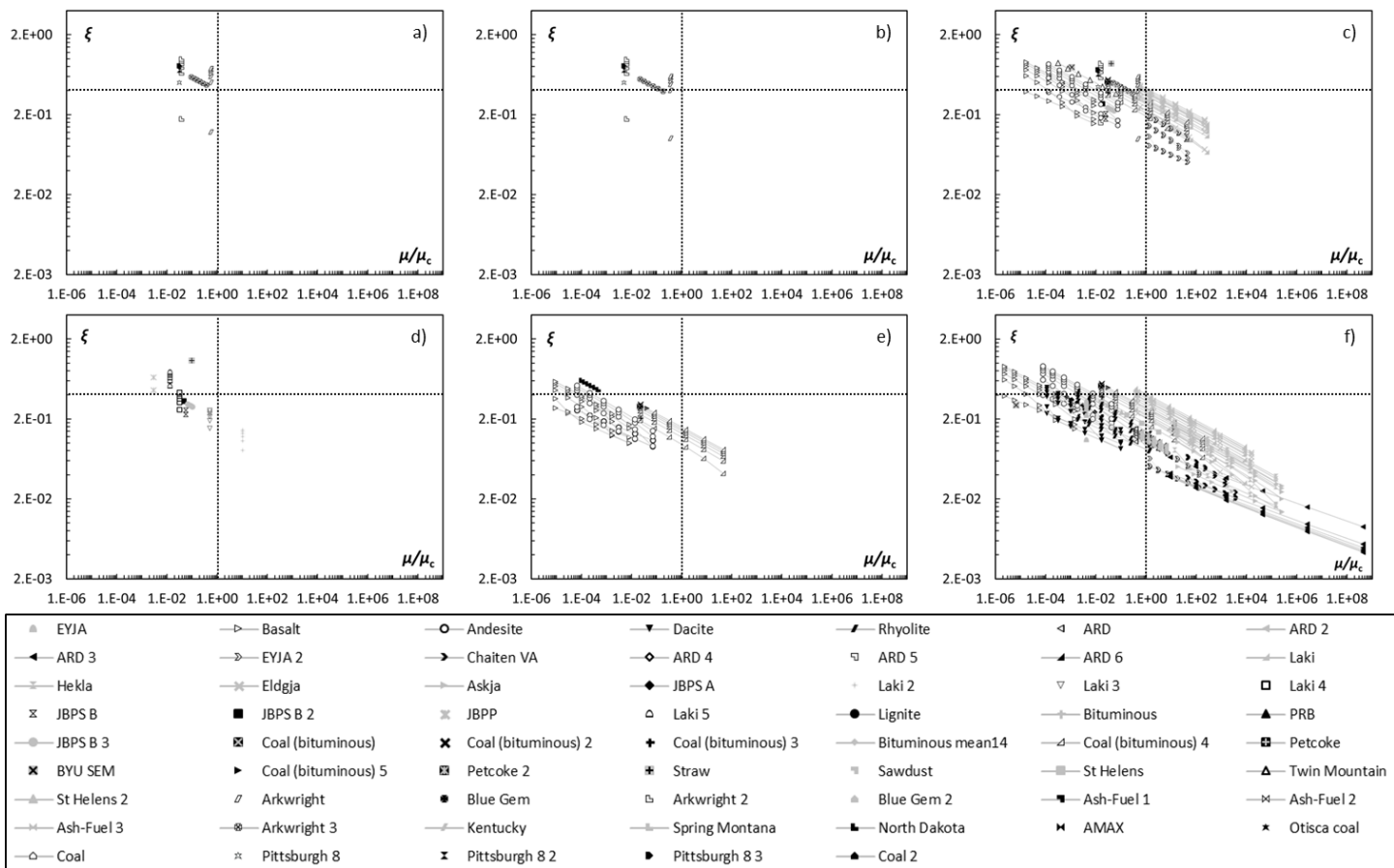


Figure 25 – Model comparison critical viscosity/energy-based: a) S^2 , b) WF, c) S&T, d) RRLG, e) SDS and f) GRD. The vertical line divides rebound/adhesion regions according to the critical viscosity method while the horizontal line divides rebound/adhesion regions according to energy-based model

5.4.1 Influences of particle composition

In this section, several specific analyses are realized considering volcanic ash and coal-like tests. Volcanic ashes are characterized by a lower content of silica dioxide than ARD, allowing the application of three viscosity models (NPL, S&T, and GRD) matching the ash composition and the applicability limits.

Figure 26a reports a detailed analysis of Basalt and Andesite tests according to NPL, S&T, SDS, and GRD viscosity models. The marker shape indicates the test while the color indicates the viscosity method. According to the volcanic ash classification, basalt and andesite are characterized by a different content of silica dioxide. With this comparison, clearly visible is the effects of the viscosity model on the sticking/rebound prediction. The NPL method gives higher values of particle spread factor, but at the same time, provides a viscosity ratio (μ/μ_c) prediction closer to the threshold $\mu/\mu_c = 1$. The SDS model provides the lowest values of particle spread factor determining conflicting predictions in the case of energy-based sticking model.

In Figure 26b, Laki tests are reported. The NPL model determines closer viscosity ratio value to the threshold ($\mu/\mu_c = 1$) in the sticking region but, the effect affects also the rebound region. Considering the data distribution according to the abscissa, the viscosity ratio values provided by the NPL model are the most squeezed to $\mu/\mu_c = 1$. This behavior is related to the formulation of the viscosity-temperature relation. Taking into consideration the formulas reported for each model (see Table A3 in Appendix A), the viscosity values are based on specific and not univocal data extrapolation.

Moving to the coal-like particle tests, Figure 27 considers Coal (bituminous) and North Dakota tests. These materials are characterized by the different content of silica dioxide and calcium oxide: Coal (bituminous) particles have about 50 %wt of SiO_2 and 9.5 %wt of CaO while North Dakota particles have about 20 %wt of SiO_2 and 23 %wt of CaO. As can be seen from the graph, similar effects on the viscosity ratio and spread factor values are generated by the viscosity models. The NPL formulation determines a viscosity ratio (μ/μ_c) prediction closer to the threshold $\mu/\mu_c = 1$ for the same test condition. This effect is more visible in the case of North Dakota test characterized by a lower amount of SiO_2 and a higher amount of CaO. Given that the present analysis, for a particle material similar to North Dakota, the SDS model appears more suitable for calculating particle adhesion according to the critical viscosity method. Opposite results can be obtained with the reference of the energy-based method. North Dakota tests appear closer to the threshold value

($\zeta = 0.4$) if the particle viscosity is calculated with the SDS model.

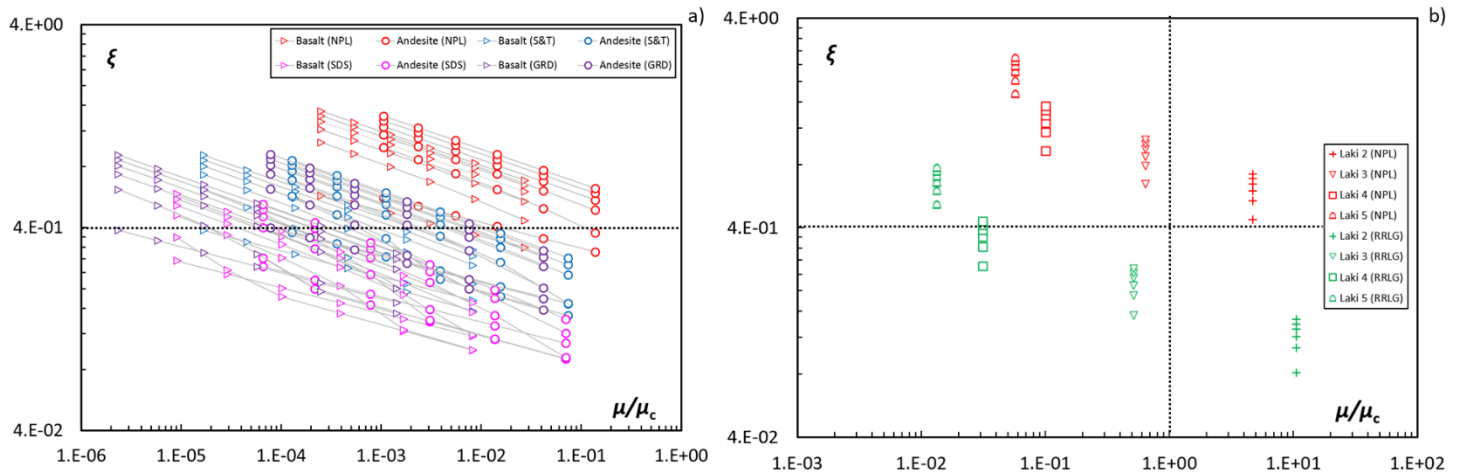


Figure 26 – Model comparison critical viscosity/energy-based for volcanic ash tests: a) Basalt and Andesite with NPL, S&T, SDS, and GRD viscosity models and b) Laki 2, 3, 4, 5 with NPL and RRLG models

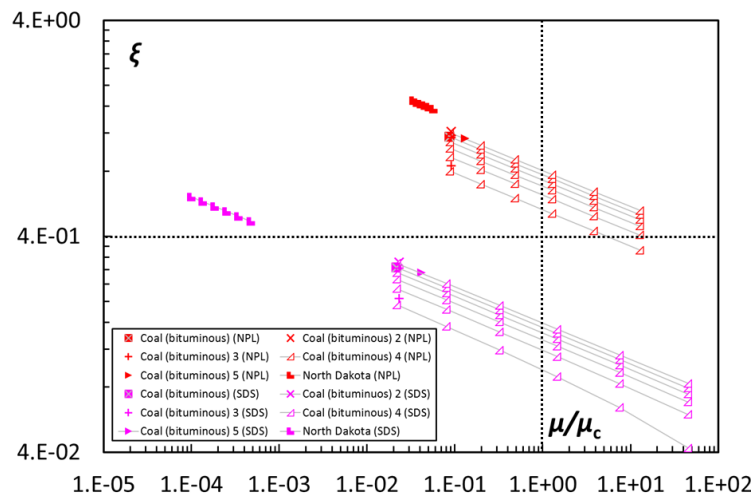


Figure 27 – Model comparison critical viscosity/energy-based for Coal (bituminous), 2, 3, 4, 5 and North Dakota tests (NPL and SDS viscosity models) characterized by a different content of silica dioxide and calcium oxide

5.4.2 Critical analysis of the viscosity models

Figure 28 reports a sensitivity analysis of the relation viscosity-temperature provided by the seven (7) models considered in the present analysis. In order to improve the readability of the graph, a logarithmic scale is used for the ordinate axis. Each trend refers to the relationship between temperature and a normalized viscosity value (M) obtained considering the magnitude of the model's constants. As highlighted by the trends, each model is characterized by a different slope and thus, different sensitivity to the temperature. NPL and S^2 models are less sensitive to a temperature variation while other models (e.g. WF and GRD) show a strong dependence to the temperature value. By increasing the temperature value of two (2) times, the normalized viscosity values increase by thirty (30) orders of magnitude.

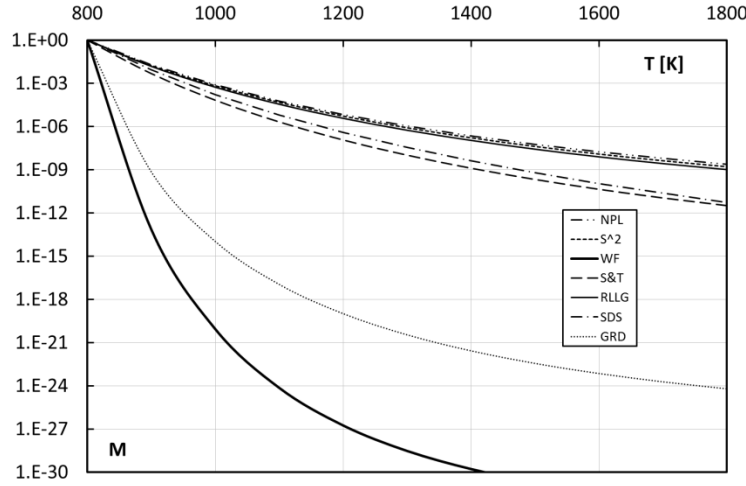


Figure 28 – Sensitivity analysis of viscosity models

This analysis shows the implication of particle temperature estimation or measurement as well as the interaction between viscosity and sticking models in the prediction of particle adhesion and/or rebound. Summarizing the outcomes of the analysis, Table 9 reports the model equations, the basis on that each model is based and, in addition, the dependences of model coefficients to the particle chemical composition. This information, together with the sensitivity analysis reported in this work, could be useful for the proper selection of the viscosity model. Beyond the NPL model, that is based on the optical basicity, the other methods are based on a specific material, that could be used as a reference for the proper application of the model. For example, the RRLG model is more suitable for slags instead of GRD, that is more appropriate for volcanic ashes. Other considerations can be done taking into consideration the model equation. The strong correlation between viscosity and temperature is different among the models, as reported in Figure 28, and, for this reason, models characterized by steeper viscosity-to-temperature trends are more suitable for the cases in which the particle experience higher temperature gradient (such as gas turbine nozzle equipped with cooling holes). As reported in Table 7, each model has a different temperature-viscosity relation. Quadratic dependency (see WF model) or linear (see GRD) show a greater variation of the viscosity for the same temperature variation.

Regarding the particle chemical composition, each model is characterized by different model coefficients which depend on the oxides contents. In Table 9, a qualitative description of the influence of particle chemical composition on the viscosity-temperature trends are reported for each viscosity model. Peculiarities can be noticed for the RRLG method, that is not related to the silica dioxide content, but only to the calcium and magnesium oxides and for the S² and WF where aluminum trioxide and magnesium oxide are not considered, respectively.

With this first model overview, it is clear how the selection of the proper viscosity model has to be related to the chemical composition of the particle and to the source of the given contaminant. In Appendix A, all model equations and coefficients are reported with the correspondent applicability limits and uncertainty.

In conclusion, if the sticking model is based on the energy dissipation, the viscosity model prediction is fundamental in order to estimate the proper energy dissipation. In this case, a viscosity model that predicts lower viscosity values, for the same particle characteristics, is suitable for predicting the particle adhesion with a wider confidence band. Besides the dedicated experimental test that represents the greatest method used to discern the actual result, it could be useful to find a new method, based on the present evidence, able to represent the combined effects related to particle deformation and its material characteristics.

Table 9 – Viscosity models: equations, basis, and dependencies

Model	Constitutive equations and basis	Dependences of model coefficients to the particle chemical composition (↑ increase viscosity value while ↓ decrease viscosity value for the same temperature)
NPL [69]	$\ln \mu = \ln A_{\text{NPL}} + \frac{B_{\text{NPL}}}{T} \quad (33)$ <p>Based on optical basicity values</p>	The optical basicity was estimated taking into consideration the mutual interaction between silica dioxide and aluminum trioxide as a function of the calcium and magnesium oxides
S ² [70]	$\log \mu = 4.468 \left(\frac{\zeta}{100} \right)^2 + 1.265 \frac{10^4}{T} - 8.44 \quad (34)$	The model is only based on glass former and modifiers Aluminum trioxide content is not taken into account directly.

	Data regression based on sixty-two (62) samples of slags	Silica dioxide ($\hat{\uparrow}$) works against calcium and magnesium oxides ($\hat{\downarrow}$)
WF [71]	$\log \mu = \frac{m_{WF} 10^7}{(T - 423)^2} + c_{WF} \quad (35)$ Data regression based on one hundred and thirteen (113) ashes samples	Silica dioxide and aluminum trioxide act together ($\hat{\uparrow}$). Only the calcium oxide is considered as modifier Magnesium oxide content is not taken into account
S&T [72]	$\log \left(\frac{\mu}{T} \right) = A_{S\&T} + \frac{10^3 B_{S\&T}}{T} \quad (36)$ Based on Non-Bridging Oxygen (NBO) values	The content of silica dioxide is dominant mitigated by the contents of aluminum trioxide and calcium oxide.
RRLG [73]	$\log \left(\frac{\mu}{T} \right) = A_{RRLG} + \frac{10^3 B_{RRLG}}{T} \quad (37)$ Checked against twenty-two (22) industrial continuous casting slag	The silica dioxide is not taken into account in the model coefficients. The viscosity value is dominated by the content of calcium and magnesium oxide ($\hat{\uparrow}$) that works against the aluminum trioxide ($\hat{\downarrow}$)
SDS [74]	$\ln \left(\frac{\mu}{T} \right) = \ln A_U + \frac{10^3 B_U}{T} - \Delta \quad (38)$ Checked against seventeen (17) coal slags	Similar to S&T
GRD [75]	$\ln \mu = \ln A_{GRD} + \frac{B_{GRD}}{T - C_{GRD}} \quad (39)$ Calibrated by means of 1774 pairs of temperature-viscosity volcanic ashes silicate melts	Silica dioxide and titanium oxide ($\hat{\uparrow}$) work against the content of calcium oxide and aluminum trioxide ($\hat{\downarrow}$)

6. DIMENSIONAL ANALYSIS

Given the literature data related to different research fields, the analysis of non-dimensional numbers characterizing the physic of the present phenomenon may represent valid support for improving the comprehension of the particle impact behavior. Starting from the particle characteristics involved in the three sticking models considered in the present review, the Buckingham Pi Theorem [179] is applied. The relationships between the particle sticking capability and several particle characteristics by means of non-dimensional groups are reported in the first part of the present section. From the results and the literature models reported above (critical viscosity, critical velocity, and energy-based models), six (6) independent variables are identified. The set of independent variables is reported in Table 10 where they are express in terms of its fundamental dimensions.

Table 10 – Pi Theorem: set of independent variables

#	Independent variables	Symbols	{kg m s}
1	Particle density	ρ_p	{kg m ⁻³ }
2	Particle diameter	d_p	{m}
3	Particle velocity	V	{m s ⁻¹ }
4	Dynamic viscosity	μ	{kg m ⁻¹ s ⁻¹ }
5	Surface tension	γ	{kg s ⁻² }
6	Young modulus	E	{kg m ⁻¹ s ⁻² }

As can be seen from Table 10 particle temperature is not included in the set of independent variables. The effect of the temperature on the particle sticking phenomenon is included in the viscosity and Young modulus variation.

The first non-dimensional group neglects the surface tension (capillary forces) contribution and considers the effect of the particle temperature by particle Young modulus and particle viscosity

$$\Pi_1 = \rho_p d_p^2 \mu^{-2} E^1 = (\rho_p d_p \mu^{-2}) (d_p E) \quad (40)$$

where the dimensional group ($d_p E$) characterizes the critical viscosity model while the first term can be processed and expressed as a function of non-dimensional number Z (see Eq. 3)

$$\Pi_1 = (d_p E) 1/(\gamma Z^2) \quad (41)$$

demonstrating how the surface tension, and thus, the capillary force has to be included in the particle sticking analysis.

The second group is obtained by considering particle viscosity the only structural characteristic that influences the particle sticking behavior

$$\Pi_2 = \rho_p^{-2} d_p^{-2} V^{-3} \mu^1 \gamma^1 = (\rho_p^{-1} d_p^{-1} V^{-1} \mu^1)(\rho_p^{-1} d_p^{-1} V^{-2} \gamma^1) \quad (42)$$

where the two non-dimensional groups correspond to the particle Reynolds number and particle Weber number

$$\Pi_2 = 1/(\text{Re We}) \quad (43)$$

Therefore, excluding the particle Young Modulus, particle Reynolds number and particle Weber number appear suitable for representing the particle sticking behavior.

Thanks to the data related to particle dimension, density, viscosity and surface tension it is possible to calculate the particle Reynolds number and the particle Weber number, defined according to Eqs (1, 2) supposing that the particle velocity is equal to the gas velocity. Therefore, starting from the literature data reported in Tables 4 – 6, and the computation of the viscosity and surface tension, Figure 29 reports the logarithmic chart with the relationship of particle Reynolds number and particle Weber number. As mentioned, the calculation is performed using the viscosity values obtained with the NPL model. The overall analysis of the We-Re trends is reported in Figure 30 where the particle Reynolds numbers are calculated according to the six (6) viscosity models considered (S² [70], WF [71], S&T [72], RRLG [73], SDS [74] and GRD [75]). The regions related to the printable fluids [19] are also reported.

The trends related to the mono-parametric variation of particle diameter, velocity and temperature are traced. In several cases, the experimental tests are carried out using a powder sample characterized by specific size distribution. For this reason, the data are aligned with the particle-diameter trend. The variation of the temperature determines the variation of particles properties like viscosity and surface tension. The test named ARD 5 is characterized by the lowest temperature (see Table 4) and for this reason, the particle Reynolds number assumes the lowest values. For the sake of clarity, this test is not reported in Figure 36.

Following the conceptual framework reported in Figure 2, non-dimensional numbers allow the generalization of the present data and the comparison between the present results with those obtained in other fields of research. Comparing the We-Re regions involved in the gas turbine particle adhesion with the We-Re regions related to the analysis of printable fluids [19], see Figure 29, some similarities can be noticed. The interactions between individual drops and the substrate as well as between adjacent drops are important in defining the resolution and accuracy of the printing process. The accuracy of the printing process is limited by the issues related to the droplet spread and/or overlap processes of adjacent drops. In particular, no-data related to gas turbine conditions belong to the region called *Satellite droplets*, in which the primary drop is accompanied by a large number of satellite droplets, but almost all data belonging to the region called *Too viscous*.

According to the literature findings [19], the majority of the gas turbine fouling data have shown little tendency to create satellite droplets and splashing. This means that, for these experimental test conditions, particles are very viscous and their deformation during the impact is too low to break themselves up. In this condition and considering the chemical composition of a particle that characterizes the fouling phenomenon, the adhesion could be promoted by low-melting substances which performed a sort of glue action at the impact region [55], [87], [137]. Given this, particle sticking models have to consider the different interaction between particle and substrate according to the chemical composition of the particle, especially when the impact conditions imply the modification of the surface interaction.

A particular condition named *onset splashing* is also highlighted and for which qualitative cross-validation with the hot section fouling tests can be done. For the majority of the collected tests, no evidence related to deposition under splashing conditions is reported. However, it is possible to extrapolate some considerations looking at the appearance of the deposits. In a general way, the splashing process is a rebound condition characterized by a particle deformation and breakup able to generate several smaller particles. Taking into consideration the tests carried out in [143] for volcanic ash particles, the comparison between Laki 2 and Laki 4 tests shows the particle impact behavior very similar to those characterizing the splashing phenomenon. Figure 32 reports the appearance of the deposited particle for the Laki 2 and Laki 4 tests with their correspondent detailed view. These two tests are characterized by the same particle diameter, but different impact velocity and temperature values. Laki 4 test is carried out with higher temperature and impact velocity values than Laki 2 test.

Laki 4 test is clearly characterized by a very high particle deformation: the deposited layer appears thinner and the splat process of the particle higher than those reported in the case of Laki 2 test. With the reference of Figure 29, Laki 4 test belongs to the *onset splashing* region while Laki 2 test belongs to the *too viscous* region confirming the experimental findings. In addition to the shape of the deposited layer, it is possible to note the presence of several smaller particles that surround the bigger one in the case of Laki 4 test. Higher impact velocity (that leads with higher Weber number) and higher temperature (that means lower viscosity and then higher Reynolds number) determine a more favorable condition for particle splashing.

Finally, an interesting aspect is related to the limit of particle Weber number. As reported by [19], for the condition $We < 4$, the energy is insufficient to generate suitable droplet for the printing process. This means that the sticking process does not take place and in fact, considering the We-Re plane reported in Figure 29, only two test conditions, related to the smallest particle diameter, of the tests named ARD 3 and ARD 5 belong to this region. According to the literature review reported in [4], these tests are carried out for studying the sticking phenomenon in cooling holes, and they are characterized by the lowest temperature values. In the light of these test

conditions, the sticking phenomena detected by the Authors for these tests, are probably related to the influence of external parameter, as for example, flow structures.

Similarities with the printable fluids highlight the possibility to use non-dimensional numbers to generalized particular experimental tests (i.e. gas turbine particle deposition) findings possible original explanations of such phenomena. In this analysis, specific information obtained a priori about splashing phenomena, could be useful for settings the best experimental test avoiding inaccuracy or misinterpretation of the results. With the reference of that background, a more general approach is reported in the following, in order to give a general post-process (not only based on printable fluids field of research) applied to the hot section fouling phenomenon.

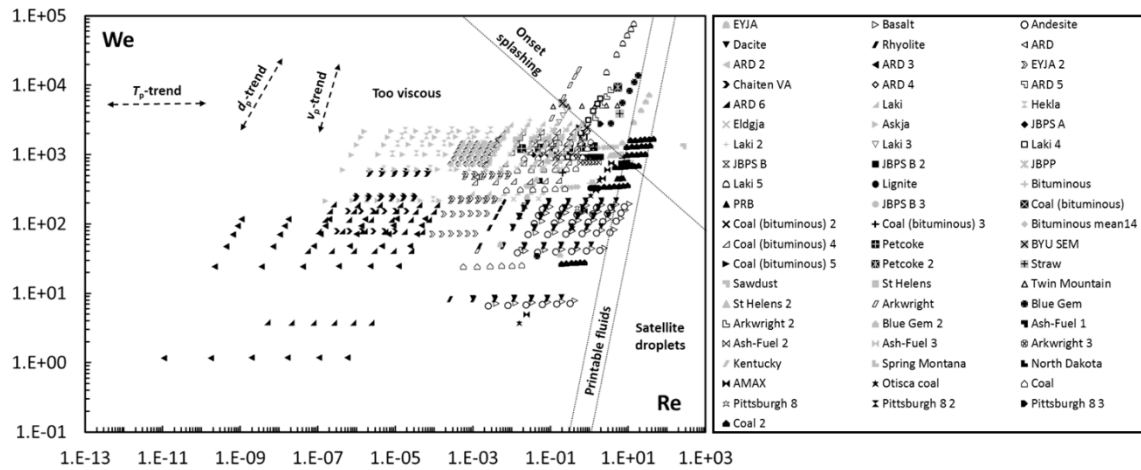


Figure 29 – Particle Weber number as a function of the particle Reynolds number (particle viscosity values were obtained using the NPL model) where for an easier visualization of the chart, ARD 5 tests (characterized by $Re = 6.8e-18 - 1.4e-16$ and $We = 3.5e-1 - 70$) is not shown: a) traced trends refer to the variation of particle diameter, particle velocity, and particle temperature, while $We-Re$ regions related to the analysis of printable fluids [19] are superimposed

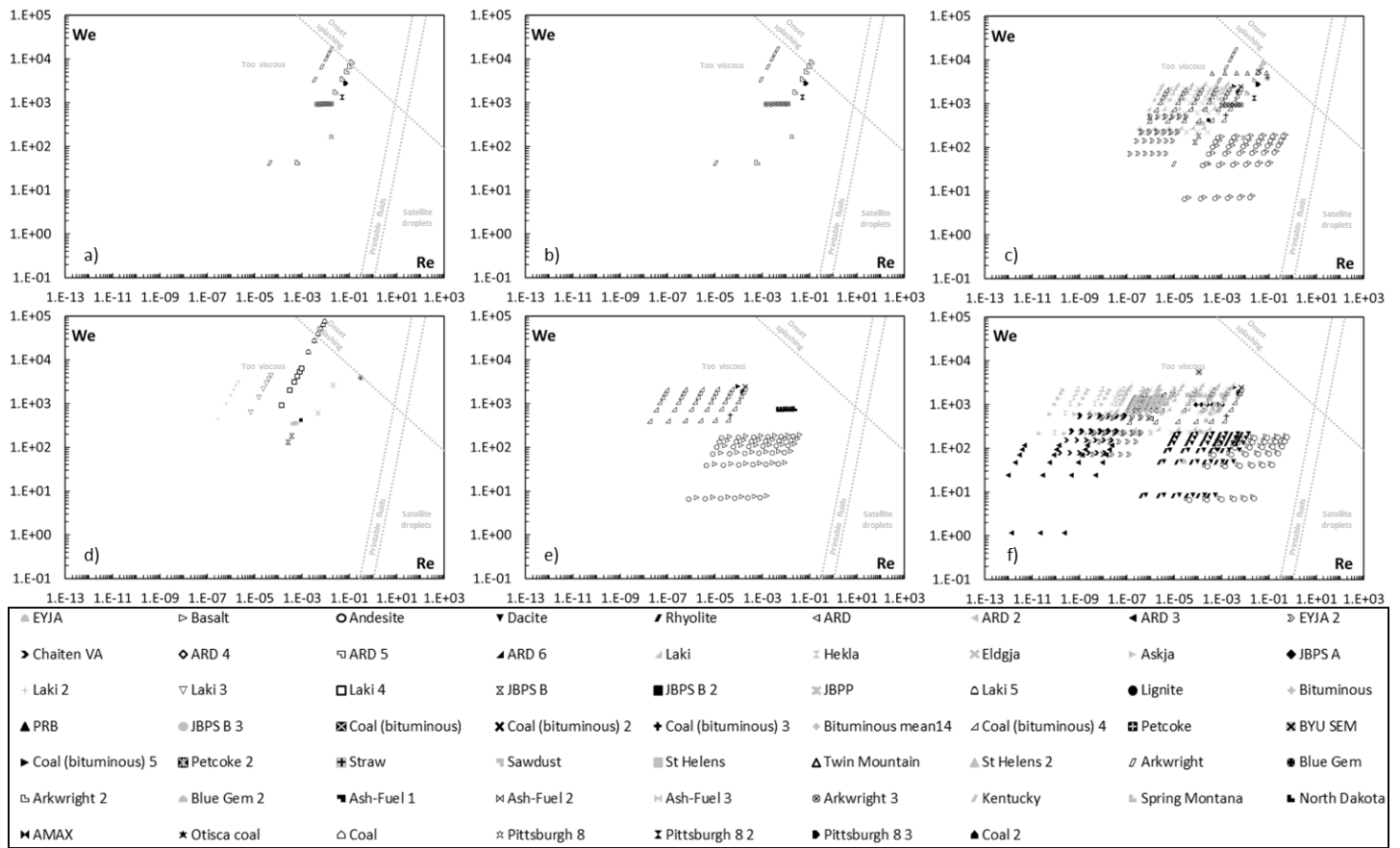


Figure 30 – Particle Weber number as a function of the particle Reynolds number according to viscosity models: a) S^2 , b) WF, c) S&T, d) RRLG, e) SDS and f) GRD. Traced We-Re regions are related to the analysis of printable fluids [19] superimposed

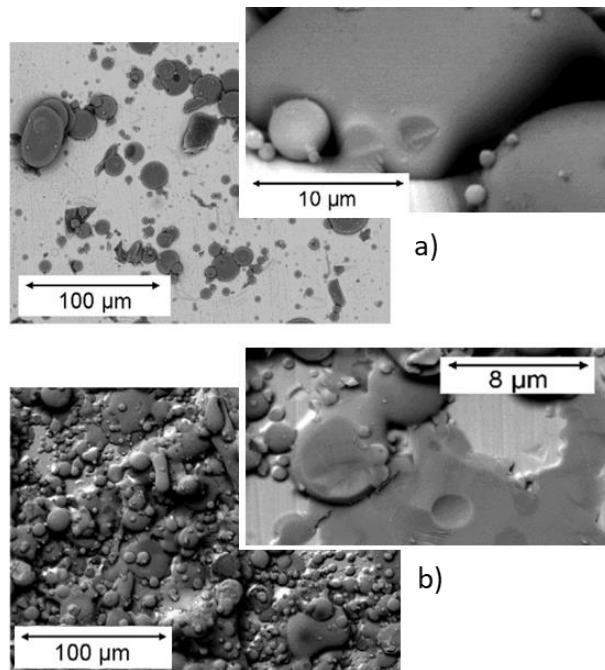


Figure 31 – Deposit layer appearance for the volcanic ash particle tests (10 μm – 70 μm) [143]: a) Laki 2 test ($T = 1043$, $v = 91$ m/s), and b) Laki 4 test ($T = 1295$ K, $v = 127$ m/s)

As mentioned, the We-Re relationship seems to be strongly correlated in the particle deposition phenomena. This result is line with the literature, where it is reported how the contemporary use of Weber number and Reynolds number allows the modeling of both surface and viscous behaviors [15]. Starting from this consideration, non-dimensional parameters allow the definition of the type of regime involved in particle impact. It may happen that molten or quasi-molten particle impacts the blade surface, deforming itself according to Figure 3. Assuming a certain degree of similarity, when a droplet (e.g. semi-molten or molten particle) impacts a wall, it may result in three different conditions: rebound, breakup or adhesion. According to the approach adopted in [15], the rebound condition is promoted by the elastic forces, the breakup condition is due to the break of the interconnection forces and finally, the adhesion condition is reached when the droplet deforms itself (spreading process), generating a sort of film on the surface by a dissipative process due to its viscosity force. Thus, the comprehension of the spreading process assumes paramount importance for particle sticking modeling [16]. In order to do this, particle Ohnesorge number (see Eq. 3) is used coupled with particle Weber number in order to define the particle spreading process [16]. Particle Weber number is related to the force that generates particle spread: at higher We the force is due to particle velocity and particle diameter while at lower We the force is due to surface tension.

Particle Ohnesorge number is related to the force that opposes particle spread: at higher Z the force is due to the viscosity, while at lower Z the force is due to the inertia. Figure 32 shows the chart We-Z defined according to the literature [16], in which the data reported in Tables 4 – 6, are superimposed (the viscosity values are calculated according to the NPL model). Present data belong to the region characterized by highly viscous particle and with the impact-driven particle spread. Therefore, the particle kinetic energy works against the viscous force. In this case, capillary force, and then, surface tension, does not influence the particle spread [16]. At the same time, the region called *Impact driven* puts the attention on phenomena such as satellite droplets and splashing which may influence the particle impact process in a gas turbine. In this case, the first particle impact generates negligible deposits but generates several smaller semi-molten particles with greater capability to stick due to their low energy content. Analogous results can be obtained using the six (6) viscosity models considered (S^2 [70], WF [71], S&T [72], RRLG [73], SDS [74] and GRD [75]) reported in Figure 33.

This analysis allows the comparison between the particles behavior involved in gas turbine fouling and other research fields. The non-dimensional analysis confirms the importance of particle viscosity, but at the same time, highlights the relationship with particle velocity and diameter. Viscous force act related to particle temperature but the particle spread is driven also by particle kinetic energy.

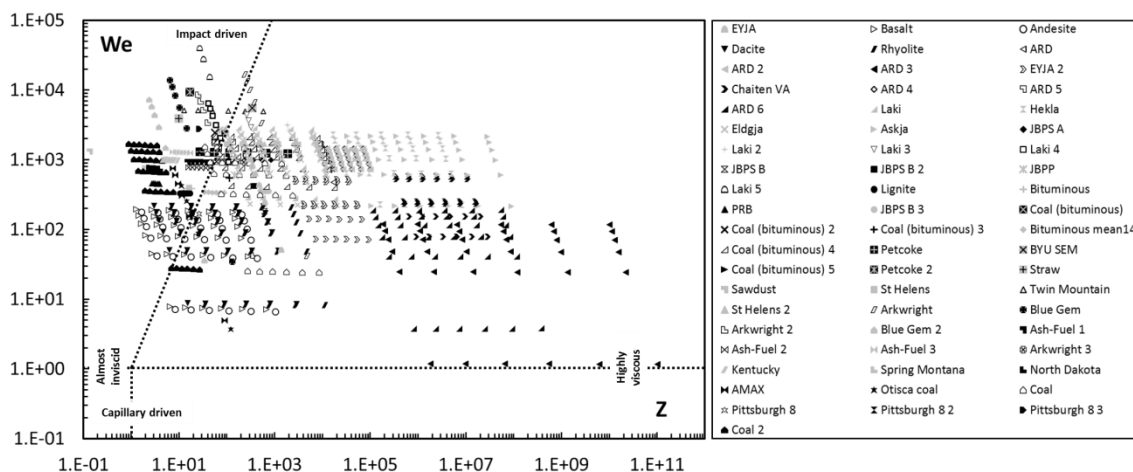


Figure 32 – Definition of the particle spread regime using non-dimensional numbers We-Z (particle viscosity values was obtained using the NPL model)

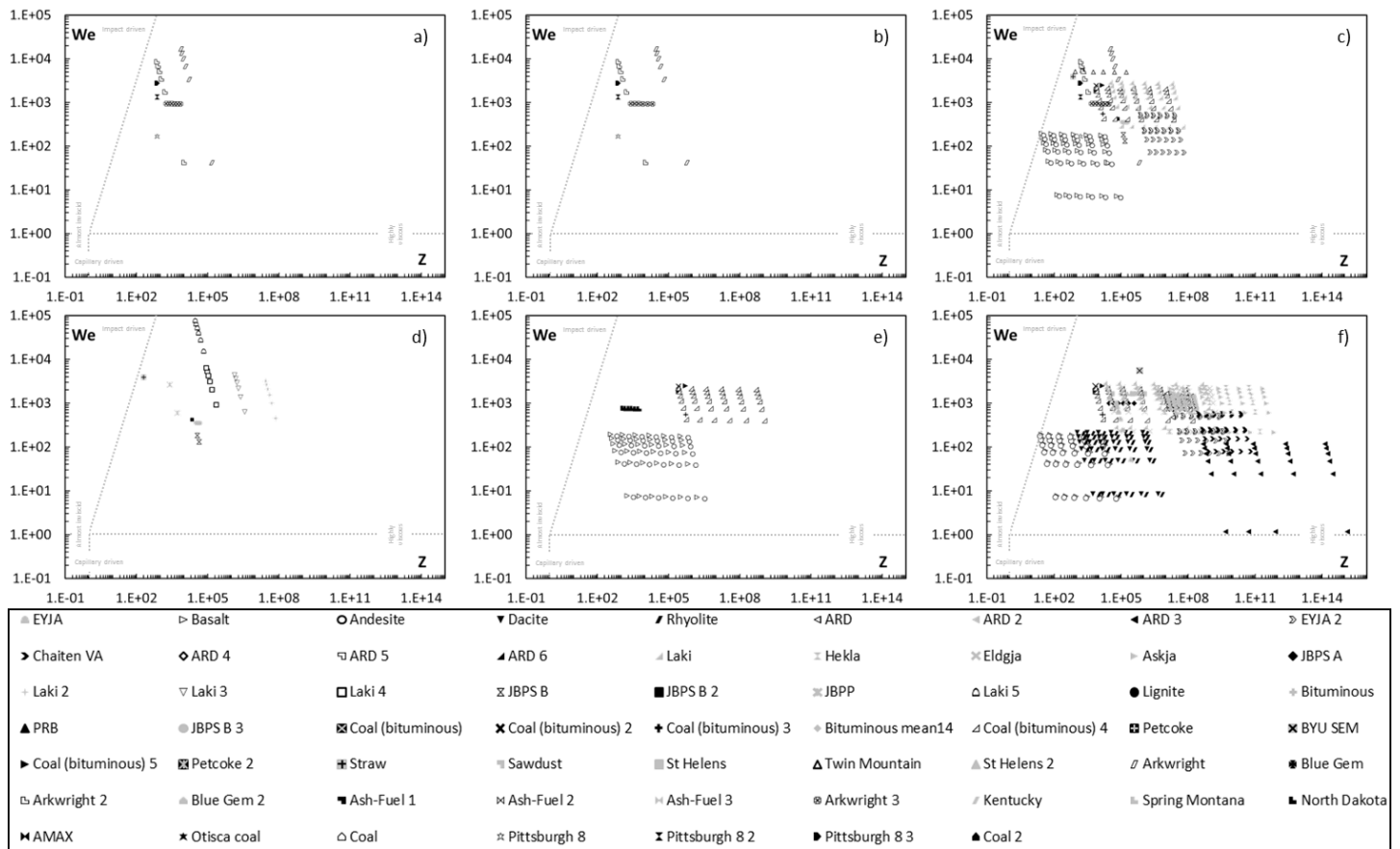


Figure 33 – Definition of the particle spread regime using non-dimensional numbers We-Z according to viscosity models: a) S^2 , b) WF, c) S&T, d) RRLG e) SDS and f) GRD

7. GENERALIZATION OF THE PARTICLE IMPACT BEHAVIOR

Neither the critical viscosity/velocity nor the energy-based methods appear able to predict particle sticking for the overall particle adhesion tests adopting a general approach. The mismatch between the prediction and the actual results of the tests can be explained by two reasons. For a specific test, deposits are generated by a certain combination of particle diameter, temperature, and velocity and therefore, by considering the overall variation of these quantities during tests, some conditions may generate particle rebound. At the same time, particle characteristics such as viscosity and softening temperature are difficult-to-be-represented by a single model able to conceive a wide range of particle chemical compositions.

Summing up, a particle impact test reporting adhesion can be the outcome of multiple superimposed effects in terms of particle size, temperature and impact conditions. In the last part of the present work, the generalization of particle impact behavior in a gas turbine is proposed. Non-dimensional groups listed above (Weber, Reynolds, and Ohnesorge numbers), allow for the generalization of particle impact/deposition data but describe only the effects of the impact into particle spread and no information about sticking phenomenon can be gathered.

In order to give a perspective view regarding particle adhesion, the data reported in Tables 4 – 6 have to be accompanied by experimental results related to the other phenomena related to particulate impact. During gas turbine operation, surface erosion, particle adhesion, and particle splashing could affect hot sections of the machinery. Erosion and fouling are generated by the same type of particles (especially rock-derived particles and coal ashes) and could take place under different or even the same conditions (such as temperature, velocity, size). Therefore, the data related to particle deposition are compared with literature data related to erosion [149], [180], [181], [182] and splashing phenomena [144].

In Table 11, the data associated with erosion tests are collected in the same way as the previous ones. Particle dimensions, density, velocity, temperature, and composition are reported as well as the softening temperature calculated applying Eqs (19 – 23). These tests refer to hot erosion measurements realized using dedicated test benches. It is possible to notice how erosion tests are characterized by lower temperature with respect to those involved in particle deposition tests. In particular, Laki 6 test is very similar to the Laki 5 test (see Table 5) but it is characterized by lower particle temperature.

In Table 12 data associated with splashing tests are collected. These materials are also among the ones reported in Tables 4 – 6 and used for the deposition tests, but in this case, tests and particle dimensions are different. These tests consist of a spherical-pellet of volcanic ash projected at high velocities towards a substrate. Particle splashing is evaluated by checking the digital images taken during the particle impact during the test [144]. In this case, particle splashing is the only effect known and no data related to erosion issues are reported. All materials refer to three different volcanic ashes and the particle size involved in these tests is higher with respect to the previous one. Also, in this case, the softening temperature values are calculated applying Eqs (19 – 23).

Table 11 – Particle erosion data. Material composition in term of weight fraction

Authors	Material	d [μm]	ρ [kg/m^3]	v [m/s]	T [K]	T_{soft} [K]	t	Na ₂ O	K ₂ O	CaO	MgO	SiO ₂	Al ₂ O ₃	TiO ₂	Fe ₂ O ₃
'13 Shinozaki et al. [149]	Laki 6	20–100	2400	115	983	1258	T	1.2	0.1	7.8	3.1	47.2	11.6	3.7	25.2
'92 Tabakoff et al. [180]	Coal ash	15	2900	366	800 – 1089	1288	C	0.0	0.0	0.0	0.9	48.1	21.2	0.0	20.1
'84 Tabakoff [181]	CG&E	38.4	2900	240	422 – 922	1288	C	0.0	0.0	0.0	0.9	48.1	21.2	0.0	20.1
'80 Kotwall and Tabakoff. [182]	CG&E 2	38.4	2900	228	756	1288	C	0.0	0.0	0.0	0.9	48.1	21.2	0.0	20.1
	Kingston	15, 28	2900	228	756	1408	C	0.2	2.1	1.3	1.0	54.4	28.6	0.5	10.1

Table 12 – Particle splashing data. Material composition in term of weight fraction

Authors	Material	d [μm]	ρ [kg/m^3]	v [m/s]	T [K]	T_{soft} [K]	t	Na ₂ O	K ₂ O	CaO	MgO	SiO ₂	Al ₂ O ₃	TiO ₂	Fe ₂ O ₃
2016 Dean et al. [144]	Laki 7	6500	2000	106	1473	1161	C	4.0	1.0	11.0	5.0	50.0	12.0	3.0	14.0
	Hekla 2	6500	1500	106	1473	1290	C	3.0	2.0	3.0	0.0	65.0	15.0	0.5	6.0
	Eldgja 2	6500	1900	106	1473	1161	C	3.0	0.5	11.0	6.0	50.0	13.0	3.0	16.0

The first analysis shows the plane We-Z, Figure 34, populated by the data reported in Tables 4 – 6, Table 11 and Table 12 (the viscosity values are calculated according to the NPL model). Data related to particle deposition, shown in details in Figure 32, are reported using grey dots in order to highlight the differences with the erosion and splashing data.

As shown in Figure 34, splashing data completely belong to the region called *impact driven*, while erosion data belong to the *highly viscous* region characterized by very high values of particle Ohnesorge number. This non-dimensional analysis shows quite different impact regimes involved in particle deposition and particle erosion/splashing. In the latter cases, the particle is characterized by size and/or velocity much more high with respect to the adhesion case. Higher particle Weber number implies a spread regime driven by the dynamic pressure gradient while lower values of particle Ohnesorge number implies a resistance force driven by particle inertia [16]. Erosion data are collected at a lower temperature with respect to the splashing ones, and as shown in Figure 34, viscous effects are much greater and the inertia force is less. Therefore, erosion phenomenon seems to be characterized by a particular combination of particle kinetic energy and viscosity able to determines particle impact with material removal from the target, without adhesion. Even if this distinction appears suitable for adequately representing the erosion occurrences, it is important to note that, especially for higher temperature, erosion issues are related also to the substrate characteristics [181]. The concurrent presence of erosion and deposition has been found also in some numerical analyses performed by the Authors [183].

From this analysis, a quite clear pattern can be recognized: deposition, erosion and splashing data belong to different regions in the We-Z plane, with the particular characteristic that deposition and erosion regions have in common the values of particle Weber number (in this case, the most discerning parameter is the particle viscosity), while deposition and splashing regions have in common the values of particle Ohnesorge number (in this case, the most discerning parameter is the particle velocity). Therefore, the combination of particle kinetic energy and surface tension seems to well describe the deposition, erosion and splashing phenomena.

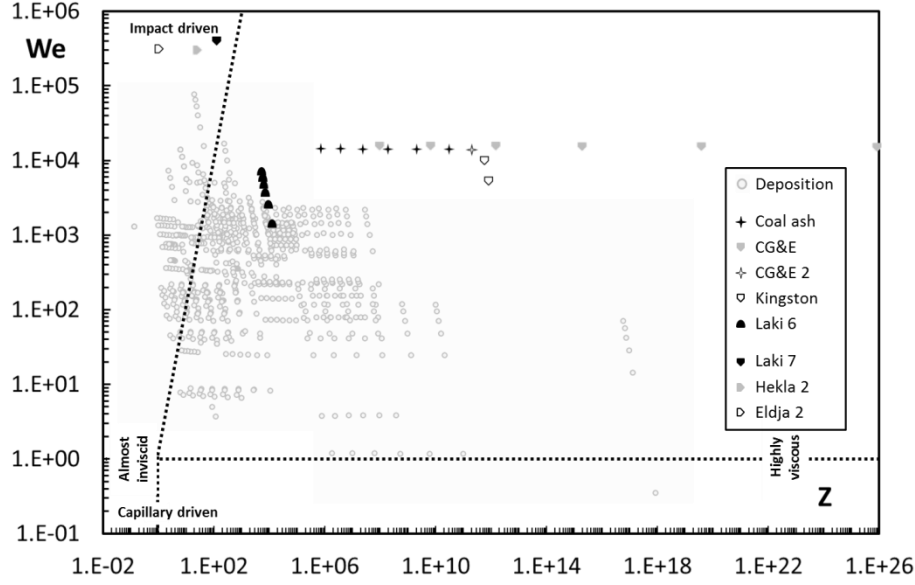


Figure 34 - Particle spread regime using non-dimensional numbers including erosion and splashing tests (particle viscosity values was obtained using the NPL model). Particle deposition data are reported with grey dots.

Starting from these considerations, two (2) new non-dimensional groups are proposed. Based on the Pi Theorem proposed in the previous section, by imposing a proper set of coefficients, the relation between kinetic energy and surface tension are

$$\Pi_3 = \rho_p d_p V^2 \gamma^{-1} \quad (44)$$

and by re-arranging the terms the third non-dimensional group can be expressed as

$$\Pi_3 = (\rho_p d_p^3 V^2) (d_p^{-2} \gamma^{-1}) \quad (45)$$

The first term represents the particle kinetic energy and the second term represents the particle surface energy. As shown above, particle kinetic energy and the surface energy work in the opposite way. If kinetic energy increases, the particle/surface interaction is driven by inertia, while if surface energy increases the particle/surface interaction is driven by surface energy (i.e. capillary forces). Defining the particle kinetic energy as

$$E_{kin} = \frac{1}{2} m v^2 \quad (46)$$

and the particle surface energy as

$$E_{surf} = \gamma A = \gamma 4\pi r^2 \quad (47)$$

the considered non-dimensional group is defined according to the Pi Theorem as

$$K = E_{kin}/E_{surf} \quad (48)$$

The second parameter is related to particle softening. As highlighted above, the viscous force determines how particle dissipates the kinetic energy at the impact. In order to represent this, the non-dimensional group defined as

$$\Theta = T/T_{soft} \quad (49)$$

is chosen. As reported, particle viscosity is directly related to particle temperature via its composition. Each material has proper characteristics and its specific value of softening temperature. This ratio represents how far the particle is from the softening state, overpassing the definition of absolute values of particle viscosity, that, as reported, is difficult-to-be-known. At the same time, the use of Θ ratio “relative” parameter allows the comparison among different conditions. As reported in [84] working with particle temperature “pure” parameter could misalign the actual operating condition with the test operating conditions. As described in [84], glassy volcanic ash softens at temperature values that are considerably lower than those required for crystalline silicates to start to melt and, for this reason, the use of standard materials in laboratory tests (e.g. MIL E 5007C test sand) instead of actual volcanic ash, determines no-reliable particle deposition results.

Softening temperature is already used as a threshold value in the particle sticking model (such as the critical viscosity model) representing the discerning values between sticky and no-sticky particles. As reported in this work, the determination of the softening temperature for a given material is well defined as a standard procedure (such as test devices, atmosphere, thermal gradient, specimen preparation, etc.) that allows the determination of the characteristic temperature (FT, HT, IT and ST) with a specific confidence band (see Figure 5) [21]. With the reference of the previous description, the standard method is affected by a greater inaccuracy than other

ash fusion temperature tests methods (such as the TMA and DSC) but, for the aim of the present investigation, this does not represent a limitation due to the fact that the post-process is based on the particle softening temperature estimation by means of the Yin et al [88] model (see Eqs 19 – 23 for details). By contrast, the definition of a critical viscosity value and its relation with temperature are not discovered in details yet [64]. Differences in viscosity values are detected during tests with constant shear and cooling rates compared with those measured in variable shear rate and stepwise cooling experiments [64] running with standard test conditions [65].

With the present approach, the estimation of the particle behavior according to the temperature variation become easier, more accurate and reproducible rather than the particle viscosity measurement that could be affected by non-univocal test methods [63], [184] and by rheological behavior due to the possible non-Newtonian effects. In fact, silica melts viscosity measurements are affected by three categories of inaccuracy due to (i) device, (ii) material and (iii) fluid behavior [63]. The first one is responsible for inadequate temperature control and geometric misalignment within the viscometer while the second determines several uncertainties related to the inhomogeneity due to evaporation, molecular degradation, improper mixing and phase separation. The latter category introduces several inaccuracies due to flow instability and transient phenomena related to non-Newtonian effects.

Using the non-dimensional groups K - Θ , Figure 35 shows the data collected for particle deposition (Tables 4 – 6), erosion (Table 11) and splashing (Table 12). Data belonging to the three categories are clearly subdivided. Particle erosion data are divided from particle deposition data due to the different values of the ratio Θ . Also splashing data are clearly distinguished and belonging to a region characterized by higher temperature and kinetic energy. In this case, the ratio K discerns the phenomena.

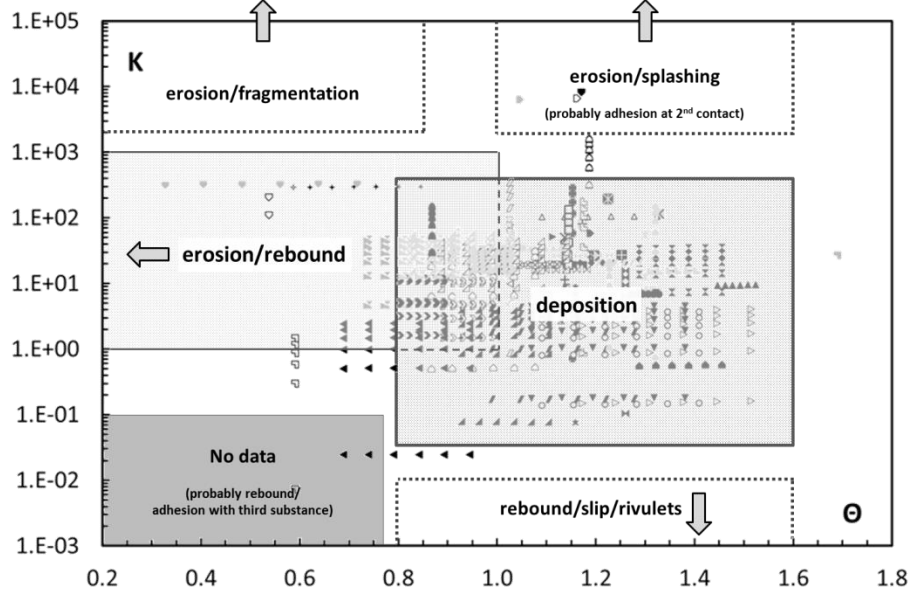


Figure 35 – Impact behavior map using non-dimensional groups $K=E_{kin}/E_{surf}$; $\Theta=T/T_{soft}$

In the light of the present considerations, specific regions can be recognized and they are superimposed on the data collection. In the chart, different impact behaviors are identified as a function of the literature data. With the reference of Figure 35, in the following description, each region will be analyzed in detail:

- *deposition*: this region comprises the data reported in Tables 4 – 6. The combination of particle temperature and softening temperature allows the dissipation of the impact energy by particle deformation determining adhesion. Particles with these characteristics are too soft to cause erosion issues and do not have enough kinetic energy to determine the splashing phenomenon. In fact, when particle temperature is higher than the softening temperature, the ratio K does not allow particle splashing. The erosion phenomenon is related to the strength of the surface that strongly depends on the temperature values [185], [186], [187] and for this reason, a certain superimposition between the deposition/erosion region has to be considered. Beyond this behavior due to the characteristics of the surface, the overlapping region is related to the definition of the temperature ratio Θ (see Eq. 49). As well reported in [87], the melting fraction at the softening temperature could be equal to 60 % depending on the composition of the ash. The correspondence of the melting fraction and the different ash fusion temperature values demonstrate that the sticking process starts in correspondence of lower value of melting fraction. Such experimental evidence confirms that the sticking process could be characterized by lower temperature values (than the softening one) and, the extension of the deposition region reported in Figure 35 seems to be representative of the phenomenon. The last consideration of the present region could be related to the non-Newtonian effects during particle impact. As reported by Giehl [145], for particles characterized by a lower content of silica

dioxide, the highest velocity impact does not determine the particle adhesion but, due to the high value of strain rate, particles bounce off driven by the increased stiffness;

- *erosion/rebound*: in this region, the kinetic energy is high and some particles could rebound determining the associated surface erosion. Particles are characterized by the lower capability to deform itself, and, for this reason, the dissipation of the kinetic energy that characterized the particle upon impact is dissipated through the surface generating dimples and cracks. Kinetic energy associated with the particle dimension and velocity is able to generate surface erosion as a function of the substrate resistance. As reported in the literature [188] the proper prediction of the erosion issue it is possible only when the particle and substrate characteristics are well known as well as the kinematic impact condition such as velocity and incoming angle. Due to this fact, the evaluation of the magnitude of the erosion issue it is not possible with the use of the present approach, even if, it is very useful to identify which impact conditions may be more detrimental (in terms of erosion) than other;
- *erosion/deposition*: in this region, particle viscosity plays a double role. It is still suitable for generating particle adhesion (the particle is sufficiently soft) but at the same time, it can determine erosion issues as well [110]. The particle assumes a viscoelastic property related to a semi-solid state. Experimental tests conducted in this region should consider the double effects of particle deposition and particle erosion. The deposits obtained during these tests are affected by two phenomena and, is not suitable for generating/validate deposition or erosion models. The outcome of such tests may be the result of the simultaneous occurrence of the two effects. Thus erosion might falsify the final deposition since part of the build-up have been removed;
- *erosion and fragmentation*: this region is characterized by a higher value of particle viscosity and higher kinetic energy. Particle deposition does not take place, confirming the role of the particle softening [189] (with the reference of erosion/deposition region explanation). For example, several erosion tests at high temperature (1255 K) using alumina particles are reported. In this case, Θ is equal to 0.54 and K is equal to 40 and no deposition is detected during tests [190]. Increasing the particle kinetic energy, the fragmentation increases as well as the erosion issues [191] and [192]. Fragmentation is due to the part of kinetic energy absorbed by the particle during the impact. This part of the energy is dissipated by the particle through its fragmentation. The amount of energy dissipated during this process is a function of particle velocity and mass, or in other words, of its kinetic energy. Therefore, starting from a certain amount of kinetic energy, the erosion phenomenon is accompanied by fragmentation. This effect occurs for lower values of Θ for which the viscoelastic properties of the particle do not allow sufficient deformation able to dissipate this part of energy;
- *erosion/splashing*: this region is strongly related to the fragmentation one, but the higher values of Θ determine different particle behavior. As shown in the literature [144], tests conducted with high particle temperature (1473 K), impact velocity of 100 m/s and particle diameter equal to few millimeters, generate an impact characterized by breaking up (yet during the flight) and extensive deformation on impact with the substrate. In these tests, the particle kinetic energy is equal to about $1e-2$ J considerably higher than the kinetic energy involved in the particle deposition tests realized with hot gas turbine section. Therefore, even if the viscosity values are suitable for generating particle adhesion, the high values of kinetic energy determine particle break-up (splashing) and limiting particle adhesion, and then, deposits. Particle splashing occurs when the inertia force is higher with respect to the viscous and capillary forces. At the same time, the particle splashing generates a large amount of smaller semi-molten droplet, re-entrained by a flowing gas [193], having lower kinetic energy. In this case, the particle behavior is very similar to the one characteristic of the *deposition* region;
- *rebound/slip/rivulets*: when the kinetic energy diminishes and/or the particle surface energy increases the particle that impacts on the surface rebounds or, in the case with very low kinetic energy particles slip on this. This phenomenon is known as a lotus effect [194], [195] and [196] particle/drop slips/rolls on the surface driven by capillary forces. Elastic phenomena could influence the particle impact or by contrast, the particle has extremely lower energy that the rebound it is not possible;
- *no data*: in this region, no literature data are available but, in the track of the former considerations, some hints can be reported. In this region, the values of the ratio Θ imply the viscoelastic behavior of particle that could promote rebound (and the associated erosion issues), but at the same time, the lower values of the ratio K do not generate surface erosion. Therefore, if particle adhesion occurs, it is probably due to particular conditions or to the presence of a third substance or an attraction force (for example Van der Waals force) that promotes particle sticking. One of the particular condition is described well by Sacco et al. [197]. In this experimental test, the ARD particles impact the surface of the internal cooling holes with very low velocity and significantly low temperature (< 728 K). In these conditions, some particles are trapped in recirculating and stagnation zones and they repeatedly impact the hot surface at low velocity [197]. Regarding the presence of the third substance, experimental results [198] have shown that, in the case of dry conditions, particles are able to stick to the surface if the impact velocity (in the normal direction) is lower than a certain limit. When the values of kinetic energy are lower, due to the smaller particle diameter ($0.1\text{--}1.5$ μm), rather than lower velocities, and if a third substance is present, particle sticking is promoted. This condition is very to that found in the gas turbine compressor sections. Sub-micro-sized solid particles are a class of particles that determine compressor fouling [4], or in other words, these particles stick under cold conditions. As reported in the literature, compressor fouling is promoted by the presence of third substances at the particle surface interface [53], [199] and for these reasons, the adhesion capability that characterizes this region, could be due to the effects of particular surface conditions. Unfortunately, detailed experimental analyses

are not reported in the literature. A small number of contributions (compared to those reported for hot sections) involved particle sticking analysis relate to cold conditions. On-field detections [199], [200] have revealed that only the first stages are affected by deposits and are driven by the presence of liquid water at the particle surface interface. Regarding wind tunnel tests, Kurz et al. [201] reported an experimental investigation which provides experimental data on the amount of foulants in the air that stick to a blade surface under dry and humid conditions. The tests show a higher deposition rate provided by wet surfaces compared to dry ones. Similar results are reported in [202] where glue agents on the blade surface enhance the particle adhesion rate dramatically. In hot sections, glue agents are described with the name of vapor deposition [55], [137], [169], [190], and [203]. This phenomenon, due to the presence of a condensed phase downstream the combustor sections, can increase the adhesion capabilities of nanoparticles (mass mean diameter $< 0.1 \mu\text{m}$) dragged in the vicinity of the surface by diffusion and thermophoresis forces, especially in the presence of film cooling. Vapor particles migrate through the boundary layer toward the cool wall. If the boundary layer temperature is below the dew point, condensation takes place at the wall [204].

8. REMARKS

In this final part, the impact behavior map, early proposed, was checked against several different cases. The first analysis refers to the particle sticking data already used for the map identification, for which a detailed subdivision between the reported results (see Tables 4 – 6) is performed (if possible). In particular, Figure 36 reports the impact behavior map with the superimposition of several different tests divided according to silty (Figure 36a), coal-like (Figure 36b), and volcanic ash particles. Volcanic ashes are reported in both Figure 36c and Figure 36d for improving the readability. Each bounded region represents the covered region on the impact behavior map according to the test conditions, while the solid-colored red-region represent the test condition for which the Authors have reported the most detrimental effects related to particle sticking. The data summarized in Figure 36 are all the available data which have reported the present distinction. Clear visible is the presence of contradictory results in the region named *erosion/deposition* (see the map description early reported) for which, tests conducted with silty and coal-like particles, do not show a high amount of deposits, while tests carried out with volcanic ashes show the greatest sticky conditions. Therefore, even if each test is carried out for studying particle adhesion, not all of the particle impact conditions generate particle sticking, or in a better way, a particular condition could be more detrimental than other. This distinction, carried out in a qualitative way (due to the lack of information that characterizes the test reports), shows how each impact test is characterized by its own peculiarities, and, only by unpacking the impact behavior into its fundamentals, the comparison between different tests can be done.

Looking into the analysis, it is clear how the data is very dispersed, but, at the same time, it can draw two major considerations: (i) particle sticking is greater moving towards high values of Θ while (ii) the relationship between the ratio K and the sticking condition is not univocal. This means that the effects of particle inertia and the interaction between the particle and substrate are not straightforward. For example, the combination of particle size and velocity changes the heating process and may affect the deposition process [145]. For the same velocity, smaller particles (lower values of K) are heated-up quicker than bigger particles (higher values of K) changing the results of the particle impact.

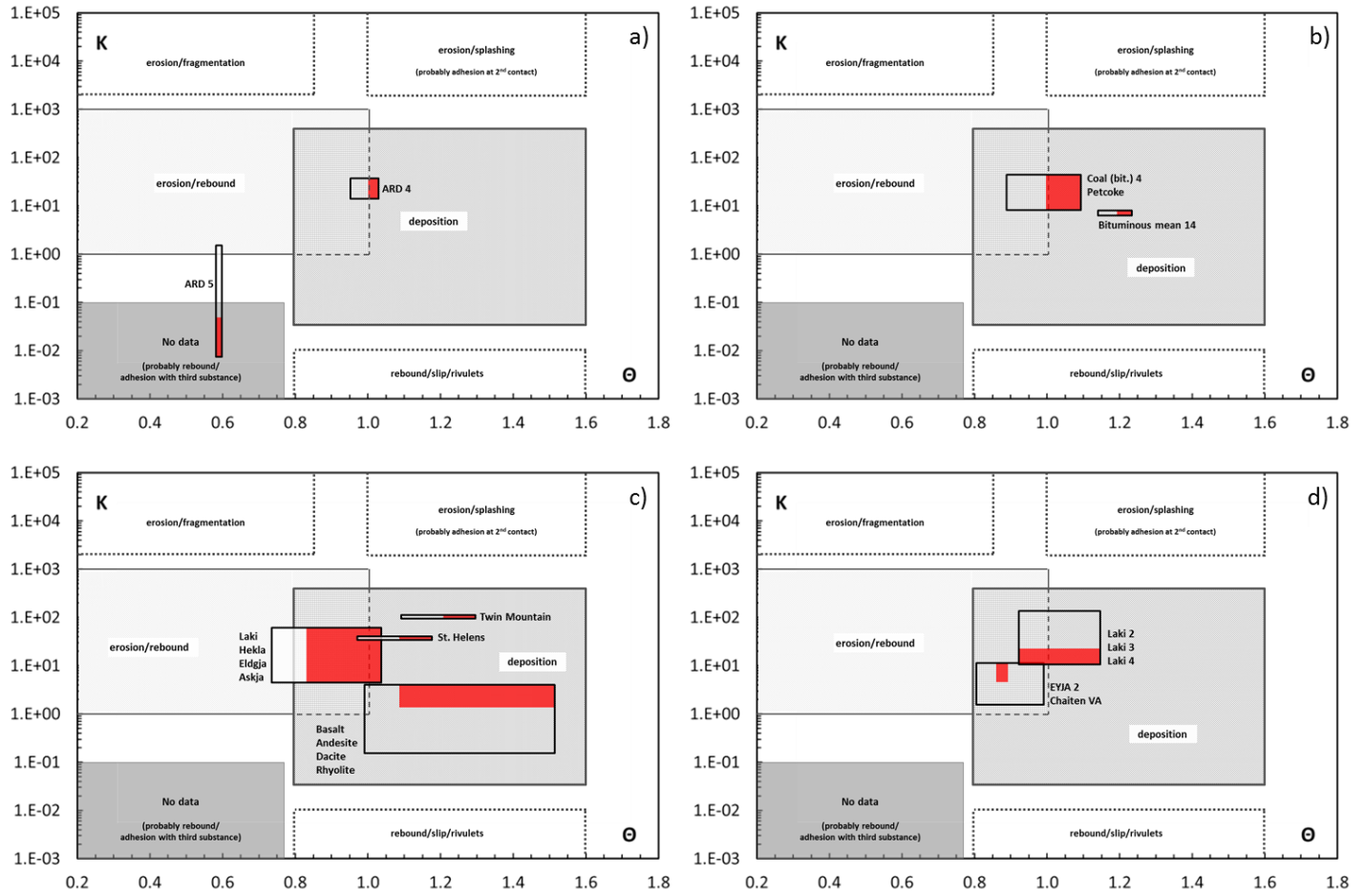


Figure 36 – The impact behavior map with the superimposition of several different tests considering the more detrimental particle sticking regions: a) silty, b) coal-like, c) and d) volcanic ash particles

In the second analysis, K- Θ map presented in Figure 35 is checked against two different cases. The first one is related to experimental tests for measuring the coefficient of restitution (COR) at high temperature [205], [206] and [207]. Tests were performed with ARD and Table 13 reports their characteristics. The second one is related to experimental tests for evaluating the erosion due to droplets impact [208], [209] and [210]. Tests were performed with water and Table 14 reports their characteristics.

Table 13 – Particle rebound characteristics data. Material composition in term of weight fraction

	Authors	Material	d [μm]	ρ [kg/m^3]	v [m/s]	T [K]	T_{soft} [K]	t	Na ₂ O	K ₂ O	CaO	MgO	SiO ₂	Al ₂ O ₃	TiO ₂	Fe ₂ O ₃
2015	Delimont et al., [205], [206]	ARD COR 1	20 – 40	2560	28	873	1366	C	3.0	3.4	3.4	1.5	72.0	12.5	0.8	3.4
		ARD COR 2	20 – 40	2560	28	1073	1366	C	3.0	3.4	3.4	1.5	72.0	12.5	0.8	3.4
		ARD COR 3	20 – 40	2560	70	1073 – 1373	1366	C	3.0	3.4	3.4	1.5	72.0	12.5	0.8	3.4
2014	Reagle et al. [207]	ARD COR 4	20 – 40	2560	47	533	1366	C	3.0	3.4	3.4	1.5	72.0	12.5	0.8	3.4
		ARD COR 5	20 – 40	2560	77	866	1366	C	3.0	3.4	3.4	1.5	72.0	12.5	0.8	3.4
		ARD COR 6	20 – 40	2560	102	1073	1366	C	3.0	3.4	3.4	1.5	72.0	12.5	0.8	3.4

Table 14 – Water droplet erosion characteristics data. Density is assumed equal to 1000 kg/m^3 , surface tension is assumed equal to 0.072 N/m and $\Theta = 1.1$

	Authors	Material	d [μm]	v [m/s]	t	K
2008	Oka et al. [208]	W 1	44	256	C	834
		W 2	50	226	C	739

		W 3	60	191	C	633
		W 4	72	148	C	456
		W 5	95	121	C	402
		W 6	108	105	C	345
		W 7	130	85	C	253
	Ahmad et al. [209]	W 8	90	350 – 580	C	3190 – 8760
		W 9	700	190 – 340	C	7312 – 23414
‘83	Hackworth. [210]	W 10	1800	222 – 290	C	25669 – 43802

Figure 37 shows the superimposition of literature data reported in Table 13 and Table 14 on the K- Θ map. The tests performed with ARD are collocated in the erosion/rebound region. These tests are realized with the aim of measuring the rebound characteristics of ARD particles confirming the region highlighted in the K- Θ map. In particular, ARD COR 3 tests conducted with higher temperature (close to 1373 K) belong to the mixed region erosion/rebound-deposition. Deposition effects are recognized during the tests realized for measuring COR of ARD particles at high temperature [206]. In detail, starting from about 1250 K (corresponding to $\Theta = 0.92$) to about 1370 K (corresponding to $\Theta = 1.01$) particle deposition takes place. A certain number of particles stick to the target surface as well as the remaining particles bounce on the target defining a specific value of COR. This experimental evidence, obtained with an experimental apparatus design for calculating rebound characteristics of micro-sized particles, confirms a particular region characterized by particle rebound/erosion and particle deposition.

The tests performed with water droplet are located in the erosion/splashing region. These tests are realized with the aim of measuring the erosion provided by water droplets. Bigger droplets and/or higher impact velocities are collocated in the upper region, where splashing is higher. The K- Θ map provided also, in this case, a good prediction of the actual behavior even if, the comparison with water droplets over-stresses the hypotheses under which the K- Θ map exists. In fact, across the T_{soft} , all materials considered for the K- Θ map identification, show a continuous trend of the relation μ - T . By contrast, water is characterized by a step function of the μ - T trend across the T_{soft} (that represents ice melting).

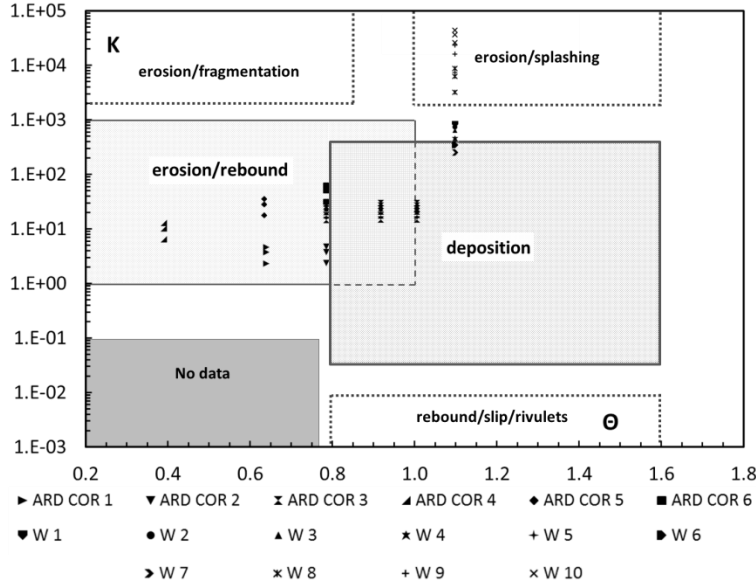


Figure 37 – Tests of ARD rebound and water droplet erosion superimposed on the non-dimensional impact behavior map K- Θ

8.1. Limitations and perspectives

Particle sticking tests, collected in the present review, cover all materials responsible for the gas turbine fouling phenomenon (silty, volcanic ash and coal-like particles). Starting from these tests, an original data post-process based on non-dimensional groups has generated the K- Θ Map, in which several different results of a generic particle impact can be *a priori* determined. The identification of the K- Θ Map by means of several independent experimental results related to the evaluation of restitution coefficients and droplet erosion has confirmed that the adopted approach seems promising for using the K- Θ Map as a predictive tool. The K- Θ prediction is can be considered reliable as the impact conditions (particle chemical composition and substrate characteristics) are similar to those considered in the present literature data collection.

After a detailed analysis of the literature, two main aspects have to be considered for the proper interpretation of the results: (i) the effects of the local temperature variation due to the film cooling on the blade surface and (ii) the effects of mutual interaction between particle and the substrate at a given temperature. Particle thermal characteristic (such as conductivity, specific heat, etc.) and the effects of glue agent due to the particular combination of chemical composition and temperature, could affect the result of a particle impact. These aspects should be considered in the use of K- Θ Map and may represent the basis for further improvements in particle deposition research.

9. CONCLUSIONS

The present analysis is based on literature data related to the experimental tests on particle deposition carried out with hot gas turbine sections-like conditions. Several considerations about particle adhesion were highlighted associated to the physical behavior of particle impact. Analyzing the particle deposition models, it is clear how the modeling of particle deposition is still a challenge. Different analytical models exist, based on experimental evidence or on basic physics principle. The model applied the most is the critical viscosity model. This model is easy to be implemented (also in a computational fluid dynamic model) but at the same time does not consider other influences on particle deposition like surface tension and particle kinetic energy. Regarding other models, for example, the energy balance model, the spread factor parameter seems not to be completely exhaustive of the particle adhesion. Erosion phenomena are characterized by higher values of particle viscosity and particle kinetic energy but, the energy-based model still predicts an adhesion-like behavior. The interaction between particle and surface is driven by the particle characteristics at the impact (e.g. velocity and particle mass) and the characteristics of the surface (e.g. surface tension or the presence of a third substance). At the same time, the sticking models are based on the calculation of particle viscosity that is estimated by means of predictive models accounting for the particle chemical composition. As demonstrated, the estimation of particle viscosity variation according to temperature is not-univocal depending on the test method or the set of materials used for model data regression.

Based on over seventy (70) experimental tests related to gas turbine hot sections reported in the literature, the proposed non-dimensional particle impact behavior map summarizes all the possible effects of particle impact on surfaces. The non-dimensional parameters, used to identify the results of particle impact, are based on the assessment of particle velocity, temperature, mass, surface tension and softening temperature. On this basis, a proper characterization of particle material is required using (i) standard tests (if exist) or (ii) predictive model of particle density, surface tension and softening temperature.

The generalization of the results is provided by using non-dimensional groups able to represent different particle impact behavior. All of the recognized regions (*deposition*, *rebound/slip/rivulets*, *erosion/rebound*, *erosion and fragmentation*, and *erosion/splashing*) are related to specific experimental evidences found in literature which highlight several effects involved in gas turbine fouling.

A particular region named *no data* is also proposed. This region is characterized by lower particle kinetic energy, higher viscosity values, and no available literature data. Therefore, what is the reason for this lack of data for interpretation? Are these particle conditions involved in gas turbine particle deposition? Are these conditions easy to be studied by experimental tests?

These questions are still open and further studies will be devoted to discover particle impact behavior and improve the knowledge about all recognized regions. Therefore, with reference to the sensitivity analysis and data post-process reported in the present work, three main outcomes can be drawn:

- the mutual correlation between the particle sticking predictive model and the model used for estimating particle characteristics (in particular particle viscosity) determine the quality of the sticking prediction. Given this, the selection of the predictive models has to be pondered according to the particle chemical composition and to the hypothesis and data which the predictive model is based on;
- the use of non-dimensional groups may represent the starting point for improving the knowledge of the gas turbine fouling and, in a wider scenario, could represent a valid support for extracting general laws useful for improving the capability of numerical tools, in the particle impact simulation;
- the predictive map can be used for estimating the particle sticking capability as well as the effects of a generic particle impact (such as erosion, splashing, etc.) characterized by specific impact conditions and particle characteristics. This approach could be useful for designing an experimental test (such as the selection of the particle chemical composition, gas temperature, etc.) or, the analysis in greater detail, for characterizing a specific operating condition of the power unit.

Experimental analyses and analytical models have to take into account the effects of the presence of third material (such as water, oily substances, etc.) at the particle/surface interface, implying several difficulties for modeling gas turbine particle deposition. All of these aspects represent the upcoming challenges, considering that both experimental and numerical analyses have to reflect the actual conditions in which the gas turbine operates.

REFERENCES

- [1] Kleinhans U, Wieland C, Flemming J, Spliethoff H. Ash formation and deposition in coal and biomass fired combustion systems: Progress and challenges in the field of ash particle sticking and rebound behavior. *Prog Energy Combust Sci* 2018;68:65-168
- [2] Bons JP, Taylor RP, McClain ST, Rivir RB. The Many Faces of Turbine Surface Roughness. *J Turbomach* 2001;123:739-48.

- [3] Ogiriki EA, Li YG, Nikolaidis T, Isaiah TE, Sule G. Effect of fouling, thermal barrier coating degradation and film cooling holes blockage on gas turbine engine creep life. *Procedia CIRP* 2015;38:228–33.
- [4] Suman A, Morini M, Aldi N, Casari N, Pinelli M, Spina PR. A compressor fouling review based on an historical survey of ASME Turbo Expo papers. *J Turbomach* 2016;139:041005.
- [5] Diakunchak IS. Performance Deterioration in Industrial Gas Turbines. *J Eng Gas Turbines Power* 1992;114:161–8.
- [6] Hepperle N, Therkorn D, Schneider E, Staudacher S. Assessment of Gas Turbine and Combined Cycle Power Plant Performance Degradation. ASME Paper 2011:45375.
- [7] Kurz R, Brun K. Fouling Mechanisms in Axial Compressors. *J Eng Gas Turbines Power* 2011;134:032401.
- [8] Clarkson RJ, Majewicz EJ, Mack P. A reevaluation of the 2010 quantitative understanding of the effects volcanic ash has on gas turbine engines. *Proc Inst Mech Eng G J Aerosp Eng* 2016;0954410015623372.
- [9] Dunn MG. Operation of Gas Turbine Engines in an Environment Contaminated With Volcanic Ash. *J Turbomach* 2012;134:051001.
- [10] De Giorgi MG, Campilongo S, Ficarella A. Predictions of Operational Degradation of the Fan Stage of an Aircraft Engine Due to Particulate Ingestion. *J Eng Gas Turbines Power* 2015;137:052603.
- [11] R. Clarkson, H. Simpson (report NATO) Maximising Airspace Use During Volcanic Eruptions: Matching Engine Durability against Ash Cloud Occurrence
- [12] Webb J, Casaday B, Barker B, Bons JP, Gledhill AD, Padture NP. Coal Ash Deposition on Nozzle Guide Vanes: Part I - Experimental Characteristics of Four Coal Ash Types. *J Turbomach* 2012;135:021033
- [13] Suman A, Casari C, Fabbri E, Pinelli M, di Mare L, Montomoli F. Gas Turbine Fouling Tests: Review, Critical Analysis and Particle Impact Behavior Map. *J. Eng. Gas Turbines Power* 2018;141(3):032601. DOI: 10.1115/1.4041282
- [14] Wang J, Vujanovic M, Sunden B. A Review of Multiphase Flow and Deposition Effects in Film-Cooled Gas Turbines. *J. Therm. Sci* 2018;22:1-17
- [15] Xu H, Liu Y, He P, Wang H. The TAR Model for Calculation of Droplet/Wall Impingement. *J Fluids Eng* 1998;120:593–97.
- [16] Schiaffino S, Sonin AA. Molten Droplet Deposition and Solidification at Low Reynolds Number. *Phys Fluids* 1997;9:3172–87.
- [17] Bai CX, Gosman AD. Development of a Methodology for Spray Impingement Simulation. SAE 1995:950283.
- [18] Stow CD, Hadfield MG. An experimental investigation of fluid-flow resulting from the impact of a water drop with an unyielding dry surface. *Proc R Soc London Ser A* 1981;373:419–41.
- [19] Derby B. Inkjet Printing of Functional and Structural Materials: Fluid Property Requirements, Feature Stability, and Resolution. *Annu Rev Mater Res* 2010;40:395–14.
- [20] Walsh PM, Sayre AN, Loehden DO, Monroe LS, Beér JM, Sarofim AF. Deposition of bituminous coal ash on an isolated heat exchanger tube: Effects of coal properties on deposit growth. *Prog Energy Combust Sci* 1990;16:327–45.
- [21] ASTM D1857-04. Standard test method for fusibility of coal and coke ash. ASTM International, West Conshohocken, PA; 2004.
- [22] Sreedharan SS, Tafti DK. Composition Dependent Model for the Prediction of Syngas Ash Deposition with Application to a Leading Edge Turbine Vane. ASME Paper 2010:GT2010-23655.
- [23] Barker B, Casady P, Shankara P, Ameri A, Bons JP. 2013, “Coal Ash Deposition on Nozzle Guide Vanes: Part II - Computational Modeling. *J Turbomach* 2013;135:011015.
- [24] Birello F, Borello D, Venturini P, Rispoli F. Modelling of Deposit Mechanisms Around the Stator of a Gas Turbine. ASME Paper 2013:GT2010-95688.
- [25] Borello D, D’Angeli L, Salvagni A, Venturini P, Rispoli F. Study of Particles Deposition in Gas Turbine Blades in Presence Of Film Cooling. ASME Paper 2014:GT2014-26250.
- [26] Prenter R, Whitaker SM, Ameri A, Bons JP. The Effects of Slot Film Cooling on Deposition on a Nozzle Guide Vane. ASME Paper 2014:GT2014-27171.
- [27] Zagnoli D, Prenter R, Ameri A, Bons JP. Numerical Study of Deposition in a Full Turbine Stage Using Steady And Unsteady Methods. ASME Paper 2015:GT2015-43613.
- [28] Singh S, Tafti D. Prediction of Sand Transport and Deposition in a Two-Pass Internal Cooling Duct. *J Eng Gas Turbines Power* 2016;138:072606.
- [29] Srinivasachar S, Helble JJ, Boni AA. An Experimental Study of the Inertial Deposition of Ash Under Coal Combustion Conditions. *Proc Combust Inst* 1990;23:1305–12.
- [30] Brach RM, Dunn PF. A Mathematical Model of the Impact and Adhesion of Microspheres. *Aerosol Sci Technol* 1992;16:51–64.
- [31] Gökoğlu SA, Rosner DE. Comparisons of Rational Engineering Correlations of Thermophoretically Augmented Particle Mass Transfer with STAN5-Predictions for Developing Boundary Layers. ASME Paper 1984:84-GT-158.
- [32] El-Batsh H, Haselbacher H. Effect of Turbulence Modeling on Particle Dispersion and Deposition on Compressor and Turbine Blade Surfaces. ASME Paper 2000:2000-GT-519.
- [33] El-Batsh H, Haselbacher H. Numerical Investigation of the Effect of Ash Particle Deposition on the Flow Field Through Turbine Cascades. ASME Paper 2002:GT-2002-30600.
- [34] Johnson KL, Kendall K, Roberts AD. Surface Energy and the Contact of Elastic Solids. *Proc R Soc London, Ser A* 1971;324:301–13.

- [35] El-Batsh H. Modeling Particle Deposition on Compressor and Turbine Blade Surfaces. PhD Thesis, Vienna: Vienna University of Technology; 2001.
- [36] Ai W. Deposition of Particulate from Coal-Derived Syngas on Gas Turbine Blades Near Film Cooling Holes. PhD Thesis, Provo, Utah: Brigham Young University; 2009.
- [37] Bons JP, Prenter R, Whitaker S. A Simple Physics-Based Model for Particle Rebound and Deposition in Turbomachinery. *J Turbomach* 2017;139:081009.
- [38] Prenter R, Ameri A, Bons JP. Computational Simulation of Deposition in a Cooled High-Pressure Turbine Stage With Hot Streaks. *J Turbomach* 2017;139:091005.
- [39] Forsyth P.R., Gillespie D.R.H., McGilvray M. Development and applications of a coupled particle deposition - Dynamic mesh morphing approach for the numerical simulation of gas turbine flows (2018) *Journal of Engineering for Gas Turbines and Power*, 140 (2), art. no. 022603. DOI: 10.1115/1.4037825
- [40] Agati G, Borello D, Rispoli F, Venturini P. An Innovative Approach to Model Temperature Influence on Particle Deposition in Gas Turbines. *ASME Paper* 2016:GT2016-57997.
- [41] Yu, K., Tafti, D. Size and temperature dependent deposition model of micro-sized sand particles (2017) *Proceedings of the ASME Turbo Expo, 2D-2017*. DOI: 10.1115/GT2017-63792.
- [42] Yu, K., Tafti, D. Impact model for micrometer-sized sand particles (2016) *Powder Technology*, 294, pp. 11-21. DOI: 10.1016/j.powtec.2016.02.014.
- [43] Kleinhans U, Wieland C, Babat S, Scheffknecht G, Spliethoff H. Ash particle sticking and rebound behavior: A mechanistic explanation and modeling approach. *Proc Comb Inst* 2016;36:2341–50.
- [44] Ni J, Yu G, Guo Q, Zhou Z, Wang F. Submodel for Predicting Slag Deposition Formation in Slagging Gasification Systems. *Energy and Fuels* 2011;25:1004–09.
- [45] Singh, S, Tafti D. Predicting the Coefficient of Restitution for Particle Wall Collisions in Gas Turbine Components. *ASME Paper* 2013:GT2013-95623.
- [46] Jones, H. Cooling, freezing and substrate impact of droplets formed by rotary atomization (1971) *Journal of Physics D: Applied Physics*, 4 (11), art. no. 206, pp. 1657-1660. DOI: 10.1088/0022-3727/4/11/206
- [47] Pasandideh-Fard M, Qiao YM, Chandra S, Mostaghimi J. Capillary effects during droplet impact on a solid surface. *Phys Fluids* 1996;8:650–59.
- [48] Ukiwe, C., Kwok, D.Y. On the maximum spreading diameter of impacting droplets on well-prepared solid surfaces (2005) *Langmuir*, 21 (2), pp. 666-673. DOI: 10.1021/la0481288
- [49] Chandra, S., Avedisian, C.T. On the collision of a droplet with a solid surface (1991) *Proceedings of the Royal Society A: Mathematical, Physical and Engineering Sciences*, 432 (1884), pp. 13-41. DOI: 10.1098/rspa.1991.0002
- [50] Mao T, Kuhn DCS, Tran H. Spread and Rebound of Liquid Droplets Upon Impact on Flat Surface. *AIChE Journal* 1997;43:2169–79.
- [51] Scheller, B.L., Bousfield, D.W. Newtonian drop impact with a solid surface (1995) *AIChE Journal*, 41 (6), pp. 1357-1367. DOI: 10.1002/aic.690410602
- [52] Mezheritsky AD, Sudarev AV. The Mechanism of Fouling and the Cleaning Technique in Application to Flow Parts of the Power Generation Plant Compressors. *ASME Paper* 1990:90-GT-103.
- [53] Zaba T, Lombardi P. Experience in the Operation of Air Filters in Gas Turbine Installations. *ASME Paper* 1984:84-GT-39.
- [54] Senior CL, Srinivasachar S. Viscosity of Ash Particles in Combustion Systems for Prediction of Particle Sticking. *Energy & Fuels* 1995;9:277–83.
- [55] Ahluwalia RK, Im KH, Chuang CF, Hajduk JC. Particle and Vapor Deposition in Coal-Fired Gas Turbines. *ASME Paper* 1986:86-GT-239
- [56] Ahluwalia RK, Im KH, Wenglarz RA. Flyash Adhesion in Simulated Coal-Fired Gas Turbine Environment. *J Eng Gas Turbines Power* 1989;111:672–78.
- [57] Singh, S., Tafti, D. Particle deposition model for particulate flows at high temperatures in gas turbine components (2015) *International Journal of Heat and Fluid Flow*, 52, pp. 72-83. DOI: 10.1016/j.ijheatfluidflow.2014.11.008
- [58] Jiang LY, Han, Y., Patnaik P. Characteristics of Volcanic Ash in a Gas Turbine Combustor and Nozzle Guide Vanes (2018) *Journal of Engineering for Gas Turbines and Power*, 140(7), art. No. 071502. DOI: 10.1115/1.4038523
- [59] Stronge WJ. *Impact mechanics*, Cambridge University Press, Cambridge, UK., 2000
- [60] Jackson RL, Green I. A finite element study of elasto-plastic hemispherical contact against a rigid flat, *J. Tribol.* 127 (2005) 343–354
- [61] Casari, N., Pinelli, M., Suman, A., di Mare, L., Montomoli, F. An energy-based fouling model for gas turbines: EBFOG (2017) *Journal of Turbomachinery*, 139 (2), art. no. 021002. DOI: 10.1115/1.4034554
- [62] Mysen BO. *Structure and Properties of Silicate Melts*. New York: Elsevier;1988.
- [63] Seetharaman S, Mukai K, Sichen D. Viscosity of Slags – an Overview. *Steel Research Int* 2005;75:267–78.

- [64] Hsieh P, Kwong KS, Bennett J. Correlation between the critical viscosity and ash fusion temperatures of coal gasifier ashes. *Fuel Process Technol* 2016;142:13–26.
- [65] ASTM D 2196-15. Standard Test Methods for Rheological Properties of Non-Newtonian Materials by Rotational Viscometer. ASTM International, West Conshohocken, PA; 2015.
- [66] Mezger 2014 The rheology handbook, 4th Ed., Vincentz Network, Hannover
- [67] ISO 6721-10:2015. Plastics – Determination of dynamic mechanical properties – Part 10: Complex shear viscosity using a parallel-plate oscillatory rheometer. International Organization for Standardization, Geneva, Switzerland; 2015
- [68] Vargas S, Frandsen FJ, Dam-Johansen K. Rheological Properties of High-Temperature Melts of Coal Ashes and Other Silicates. *Prog Energy Combust Sci*. 2001;27:237–429.
- [69] Mills KC, Sridhar S. Viscosities of Ironmaking and Steelmaking Slags. *Ironmaking and Steelmaking* 1999;26:262–68.
- [70] Hoy HR, Roberts AG, Wilkins DM. Behavior of Mineral Matter in Slagging Gasification Process. *I.G.E. Journal* 1965;444–69.
- [71] Watt JD, Fereday F. The Flow Properties of Slags Formed from the Ashes of British Coals: Part 1. Viscosity of Homogeneous Liquid Slags in Relation to Slag Composition. *J Inst Fuel* 1969;42:99–103.
- [72] Sreedharan SS, Tafti DK. Composition Dependent Model for the Prediction of Syngas Ash Deposition in Turbine Gas Hotpath. *Int J Heat Fluid Flow* 2011;32:201–11.
- [73] Riboud PV, Roux Y, Lucas LD, Gaye H. Improvement of Continuous Casting Powders. *Hüttenprax Metalweiterverarb* 1981;19:859–69.
- [74] Streeter RC, Diehl EK, Schobert HH. Measurement and Prediction of Low-Rank Coal Slag Viscosity. *The Chemistry of Low-Rank Coals ACS Symposium Series* 1984;264:195–09.
- [75] Giordano, D., Russell, J.K., Dingwell, D.B. Viscosity of magmatic liquids: A model (2008) *Earth and Planetary Science Letters*, 271 (1-4), pp. 123-134. DOI: 10.1016/j.epsl.2008.03.038.
- [76] Weymann HD. On the whole theory of viscosity, compressibility, and expansivity of liquids. *Kolloid-Zeitschrift und Zeitschrift für Polymere*. April 1962, Volume 181, Issue 2, pp 131–137.
- [77] Vogel H. The law of relation between the viscosity of liquids and the temperature. *Phys. Z* 1921, 22, 645-646.
- [78] Fulcher GS. Analysis of recent measurements of viscosity of glasses. *J. Amer. Ceram. Soc.* 1925, 8, 339-355.
- [79] Tammann G, Hesse W. The dependence of viscosity upon the temperature of supercooled liquids. *Z. Anorg. Allg. Chem.* 1926, 156, 245-257.
- [80] Hansen LA, Frandsen FJ, Dam-Johansen K. Ash fusion quantification by means of thermal analysis. In: Gupta R, Wall T, Baxter L., editors. *Impact of Mineral Impurities in Solid Fuel Combustion*. New York: Kluwer Academic Publishers; 2002, p. 181-193
- [81] Speight JG. *Handbook of coal analysis*. 2nd ed. New York: John Wiley & Sons Inc; 2015.
- [82] Degereji MU, Ingham DB, Pourkashanian M, Williams A. Numerical assessment of coals/blends slagging potential in pulverized coal boilers. *Fuel* 2012;102:345–53.
- [83] Song W, Hess KH, Damby DE, Wadsworth FB, Lavallée Y, Cimorelli C, Dingwell DB. Fusion Characteristics of Volcanic Ash Relevant to Aviation Hazard. *Geophys Res Lett* 2014;41:2326–33.
- [84] Kueppers U, Cimorelli C, Hess K-U, Taddeucci J, Wadsworth FB, Dingwell DB. The thermal stability of Eyjafjallajökull ash versus turbine ingestion test sands. *Journal of Applied Volcanology* 2014;3:1–11.
- [85] Song W, Lavallée Y, Hess KH, Kueppers U, Cimorelli C, Dingwell DB. Volcanic Ash Melting Under Conditions Relevant to Ash Turbine Interactions. *Nat Commun* 2016;7:1–10.
- [86] Gupta SK, Wall TF, Creelman RA, Gupta RP. Ash fusion temperatures and the transformations of coal ash particles to slag. *Fuel Process Technol* 1998;56:33–43.
- [87] Gupta, SK, Gupta RP, Bryant GW, Juniper L, Wall TF. Thermomechanical analysis and alternative ash fusibility temperatures. In: Gupta R, Wall T, Baxter L., editors. *Impact of Mineral Impurities in Solid Fuel Combustion*. New York: Kluwer Academic Publishers; 2002, p. 155-169
- [88] Yin C, Luo Z, Ni M, Cen K. Predicting coal ash fusion temperature with a back-propagation neural network model. *Fuel* 1998;77:1777–82.
- [89] Sukenaga, S., Haruki, S., Nomoto, Y., Saito, N., Nakashima, K.; Density and surface tension of CaO-SiO₂-Al₂O₃-R₂O (R=Li, Na, K) melts (2011) *ISIJ International*, 51 (8), pp. 1285-1289. DOI: 10.2355/isijinternational.51.1285
- [90] Shin, S.N., Gulyaeva, R.I. Density and surface tension of melts of the FeO_x-Al₂O₃-CaO-SiO₂ systems (1998) *Rasplavy*, (4), pp. 33-39.
- [91] Vadasz, P., Havlik, M., Nemecek, K. Density and surface tension of slag melts of the system Fe₂O₃-FeO-CaO-SiO₂ (1995) *Ceramics - Silikaty*, 39 (3), pp. 92-98.
- [92] Nakamoto, M., Kiyose, A., Tanaka, T., Holappa, L., Hämmäläinen, M. Evaluation of the surface tension of ternary silicate melts containing Al₂O₃, CaO, FeO, MgO or MnO (2007) *ISIJ International*, 47 (1), pp. 38-43. DOI: 10.2355/isijinternational.47.38
- [93] Choi, J.-Y., Lee, H.-G. Thermodynamic evaluation of the surface tension of molten CaO-SiO₂-Al₂O₃ ternary slag (2002) *ISIJ International*, 42 (3), pp. 221-228. DOI: 10.2355/isijinternational.42.221

- [94] Melchior, T., Putz, G., Muller, M. Surface tension measurements of coal ash slags under reducing conditions at atmospheric pressure (2009) *Energy and Fuels*, 23 (9), pp. 4540-4546. DOI: 10.1021/ef900449v
- [95] Giehl, C., Brooker, R.A., Marxer, H., Nowak, M., 2016. The Effect of Volcanic Ash Composition and Glass Content on Jet Engine Safety. *European Mineralogical Conference*, Rimini, Italy (09/2016).
- [96] Clarkson, R.J., Majewicz, E.J.E., Mack, P., 2016. A re-evaluation of the 2010 quantitative understanding of the effects volcanic ash has on gas turbine engines. *Proc. Inst. Mech. Eng. G J. Aerosp. Eng.* 230:2274–2291. <http://dx.doi.org/10.1177/0954410015623372>.
- [97] Rezaei HR, Gupta RP, Wall TF, Miyamae S, Makino K. Modelling the initial structure of ash deposits and structure changes due to sintering. In Gupta RP, Wall TF, Baxter L, editors. *Impact of Mineral Impurities in Solid Fuel Combustion*. New York: Kluwer Academic Publishers; 2002, p. 753-766.
- [98] Hanao M, Tanaka T, Kawamoto M, Takatani K. Evaluation of Surface Tension of Molten Slag in Multi-component Systems. *ISIJ International* 2007;47:935–9.
- [99] Wu C, Cheng G, Ma Q. Calculating Models on the Surface Tension of CaO-FeO-SiO₂ Molten Slags. *Research of Materials Science* 2014;3:10–6.
- [100] Grau AE, Masson CR. Densities and molar volumes of silicate melts. *Can Metall Q* 1976;15:367–74.
- [101] Courtial P, Dingwell DB. Nonlinear composition dependence of molar volume of melts in the CaO-Al₂O₃-SiO₂ system. *Geochim Cosmochim Acta* 1995;59:3685–95.
- [102] Persson M, Zhang J, Seetharaman S. A thermodynamic approach to a density model for oxide melts. *Steel Res Int* 2007;78:290–8.
- [103] Bottinga Y, Weill D, Richet P. Density calculations for silicate liquids. I. Revised method for aluminosilicate compositions. *Geochim Cosmochim Acta* 1982;46:909–19.
- [104] Mills KC, Keene BJ. Physical properties of BOS slags. *Int Mater Rev* 1987;32:1–120.
- [105] Allaby M. *A Dictionary of Geology and Earth Sciences*. Oxford, UK: Oxford University Press; 2013.
- [106] ISO 12103-1:2016. Road vehicles -- Test contaminants for filter evaluation – Part 1: Arizona test dust. *International Organization for Standardization*, Geneva, Switzerland; 2016
- [107] ASTM D388-15. *Standard Classification of Coals by Rank*, ASTM International, West Conshohocken, PA; 2015
- [108] Jensen JW, Squire SW, Bons JP, Fletcher TH. Simulated Land-Based Turbine Deposits Generated in an Accelerated Deposition Facility. *J Turbomach* 2004;127:462–70.
- [109] Anderson RJ, Romanowsky CJ, France JE. The Adherence of Ash Particles from the Combustion of Micronized Coal. Morgantown Energy Technology Center, Res. Rep. DOE/METC-85/2007 (DE85008600); October, 1984.
- [110] Ross JS, Anderson RJ, Nagarajan R. Effect of Sodium on Deposition in a Simulated Combustion Gas Turbine Environment. *Energy & Fuels* 1988;2:282–89.
- [111] Anderson RJ, Logan RG, Meyer CT, Dennis RA. A combustion/deposition entrained reactor for high-temperature/pressure studies of coal and coal minerals. *Rev Sci Instrum* 1990;81:1294–302.
- [112] Richards GA, Logan RG, Meyer CT, Anderson RJ. Ash Deposition at Coal-Fired Gas Turbine Conditions: Surface and Combustion Temperature Effects. *J Eng Gas Turbines Power* 1992;114:132–38.
- [113] Weaver MM, Dunn MG, Heffernan T. Experimental Determination of the Influence of Foreign Particle Ingestion on the Behavior of Hot-Section Components Including Lamilloy. *ASME Paper* 1996:96-GT-337.
- [114] Bons JP, Crosby J, Wammack JE, Bentley BI, Fletcher TH. High Pressure Turbine Deposition in Land Based Gas Turbines From Various Synfuels. *J Eng Gas Turbines Power* 2007;129:135–43.
- [115] Wammack JE, Crosby J, Fletcher D, Bons JP, Fletcher TH. Evolution of Surface Deposits on a High Pressure Turbine Blade, Part I: Physical Characteristics. *J Turbomach* 2008;130:021020.
- [116] Crosby JM, Lewis, S, Bons JP, Ai W, Fletcher TH. Effects of Particle Size, Gas Temperature, and Metal Temperature on High Pressure Turbine Deposition in Land Based Gas Turbines from Various Synfuels. *J Eng Gas Turbines Power* 2008;130:051503.
- [117] Ai W, Laycock RG, Rappleye DS, Fletcher TH, Bons JP. Effect of Particle Size and Trench Configuration on Deposition from Fine Coal Flyash Near Film Cooling Holes. *Energy Fuels* 2011;25:1066–76.
- [118] Ai W, Murray N, Fletcher TH, Harding S, Lewis S, Bons JP. Deposition Near Film Cooling Holes on a High Pressure Turbine Vane. *J Turbomach* 2012;134:041013.
- [119] Ai W, Murray N, Fletcher TH, Harding S, Bons JP. Effect of Hole Spacing on Deposition of Fine Coal Flyash Near Film Cooling Holes. *J Turbomach* 2012;134:041021.
- [120] Laycock RG, Fletcher TH. Time-Dependent Deposition Characteristics of Fine Coal Flyash in a Laboratory Gas Turbine Environment. *J Turbomach* 2013;135:021003.
- [121] Laycock R, Fletcher TH. Independent Effects of Surface and Gas Temperature on Coal Flyash Deposition in Gas Turbines at Temperatures Up to 1400°C. *J Eng Gas Turbines Power* 2016;138:2429919. DOI: 10.1115/1.4031318.
- [122] Boulanger A, Patel H, Hutchinson J, DeShong W, Xu W, Ng W, Ekkad S. Preliminary Experimental Investigation of Initial Onset of Sand Deposition in the Turbine Section of Gas Turbines. *ASME Paper* 2016:GT2016-56059.

- [123] Barker B., Hsu K., Varney B., Boulanger A., Hutchinson J., Ng W.F. An experiment-based sticking model for heated sand (2017) Proceedings of the ASME Turbo Expo, 2D-2017. DOI: 10.1115/GT2017-64421.
- [124] Boulanger A., Hutchinson J., Ng W.F., Ekkad S.V., Keefe M.J., Xu W., Barker B., Hsu K. Experimental based empirical model of the initial onset of sand deposits on hastelloy-X from 1000°C to 1100°C using particle tracking (2017) Proceedings of the ASME Turbo Expo, 2D-2017. DOI: 10.1115/GT2017-64480.
- [125] Cohn A. Effect of Gas and Metal Temperatures on Gas Turbine Deposition. ASME Paper 1982:82-JPGC-GT-4.
- [126] Whitlow GA, Lee SY, Mulik PR, Wenglarz RA, Sherlock TP, Cohn A. Combustion Turbine Deposition Observation from Residual and Simulated Residual Oil Studies. J Eng Gas Turbine Power 1983;105:88–96.
- [127] Wenglarz RA, Cohn A. Turbine Deposition Evaluations Using Simplified Tests. ASME Paper 1983:83-GT-115.
- [128] Wenglarz RA. Turbine Disposition, Erosion and Corrosion Evaluations Using a Simplified Test Approach ASME Paper 1987a:87-GT-214.
- [129] Wenglarz RA. Direct Coal-Fueled Combustion Turbines. ASME Paper 1987b:87-GT-269.
- [130] Kimura SG, Spiro CL, Chen CC. Combustion and Deposition in Coal-Fired Turbines. ASME Paper 1987:87-GT-266.
- [131] Spiro CL, Kimura SG, Chen CC. Ash Behavior During Combustion and Deposition in Coal-Fueled Gas Turbines. ASME Paper 1987:87-GT-267.
- [132] Wenglarz RA, Fox Jr RG. Physical Aspects of Deposition from Coal Water Fuels under Gas Turbine Conditions. ASME Paper 1989:89-GT-206.
- [133] Wenglarz RA, Fox Jr RG. Chemical Aspects of Deposition/Corrosion from Coal-Water Fuels under Gas Turbine Conditions. J Eng Gas Turbines Power 1990;112:1–8.
- [134] Wenglarz RA. An Approach for Evaluation of Gas Turbine Deposition. ASME Paper 1991:91-GT-214.
- [135] Chin JS, Lefebvre AH. Influence of Flow Conditions on Deposits From Heated Hydrocarbon Fuels. J Eng Gas Turbines Power 1993;115:433–38.
- [136] Laycock, R.G., Fletcher, T.H. Formation of deposits from heavy fuel oil ash in an accelerated deposition facility at temperatures up to 1219 °C (2018) Fuel Processing Technology, 175, pp. 35–43. DOI: 10.1016/j.fuproc.2018.03.003
- [137] Nagarajan R, Anderson RJ. Effect of Coal Constituents on the Liquid-Assisted Capture of Impacting Ash Particles in Direct Coal-Fired Gas Turbines. ASME Paper 1988:88-GT-192.
- [138] Fackrell JE, Tabberer RJ, Young JB, Fantom IR. Modelling Alkali Salt Vapour Deposition in the British Coal Topping Cycle System. ASME Paper 1994a:94-GT-177.
- [139] Fackrell JE, Brown K, Young JB, Modelling Particle Deposition in Gas Turbines Employed in Advanced Coal-Fired Systems. ASME Paper 1994b:94-GT-467.
- [140] Dunn MG, Padova C, Moeller JE, Adams RM. Performance Deterioration of a Turbofan and a Turbojet Engine Upon Exposure to a Dust Environment. J Eng Gas Turbines Power 1987;109:336–43.
- [141] Kim J, Dunn MG, Baran AJ, Wade DP, Tremba EL. Deposition of Volcanic Materials in the Hot Sections of Two Gas Turbine Engines. J Eng Gas Turbines Power 1993;115:641–51.
- [142] Dunn MG, Baran AJ, Miatech J. Operation of Gas Turbine Engines in Volcanic Ash Clouds. ASME Paper 1994:94-GT-170.
- [143] Taltavull C, Dean J, Clyne TW. Adhesion of Volcanic Ash Particles under Controlled Conditions and Implications for Their Deposition in Gas Turbines. Adv Eng Mater 2016;18:803–13.
- [144] Dean J, Taltavull C, Clyne TW. Influence of the composition and viscosity of volcanic ashes on their adhesion within gas turbine aeroengines. Acta Materialia 2016;109:8–16.
- [145] Giehl, C., Brooker, R.A., Marxer, H., Nowak, M. An experimental simulation of volcanic ash deposition in gas turbines and implications for jet engine safety (2017) Chemical Geology, 461, pp. 160–170. DOI: 10.1016/j.chemgeo.2016.11.024
- [146] Wang XY, Pu J, Yuan RM, Wang JH. Combined Influence of Surface Deposition and Hole-Blockage on Film-Cooling Performances. ASME Paper 2016:GT2016-56902.
- [147] Whitaker S.M., Lundgreen R.K., Bons J.P. Effects of metal surface temperature on deposition-induced flow blockage in a vane leading edge cooling geometry (2017) Proceedings of the ASME Turbo Expo, 2D-2017. DOI: 10.1115/GT2017-64946.
- [148] Wylie S, Bucknell A, Forsyth P, McGilvray M, Gillespie DRH. Reduction in Flow Parameter Resulting From Volcanic Ash Deposition in Engine Representative Cooling Passages. J Turbomach 2017;139:031008.
- [149] Shinozaki M., Roberts K.A., Van De Goor B., William Clyne T. Deposition of ingested volcanic ash on surfaces in the turbine of a small jet engine (2013) Advanced Engineering Materials, 15 (10), pp. 986–994. DOI: 10.1002/adem.201200357.
- [150] Naraparaju, R., Lau, H., Lange, M., Fischer, C., Kramer, D., Schulz, U., Weber, K. Integrated testing approach using a customized micro turbine for a volcanic ash and CMAS related degradation study of thermal barrier coatings (2018) Surface and Coatings Technology, 337, pp. 198–208. DOI: 10.1016/j.surfcoat.2018.01.030
- [151] Casaday B, Prenter R, Bonilla C, Lawrence M, Clum C, Ameri A, Bons JP. Deposition with Hot Streaks in an Uncooled Turbine Vane Passage. J Turbomach 2013;136:041017.
- [152] Smith C, Barker B, Clum C, Bons JP. Deposition in a Turbine Cascade with Combusting Flow. ASME Paper 2010-GT2010-22855.

- [153] Whitaker SM, Peterson B, Miller AF, Bons JP. The Effect of Particle Loading, Size, and Temperature on Deposition in a Vane Leading Edge Impingement Cooling Geometry. ASME Paper 2016:GT2016-57413.
- [154] Lundgreen R, Sacco C, Prenter R, Bons JP. Temperature Effects on Nozzle Guide Vane Deposition in a New Turbine Cascade Rig. ASME Paper 2016:GT2016-57560.
- [155] Raj R. Deposition Results of a Transpiration Air-Cooled Turbine Vane Cascade in a Contaminated Gas Stream. J Eng Power 1983;105:826–33.
- [156] Raj R, Moskowitz S. Experimental Studies of deposition by Electrostatic Charge on Turbine Blades. ASME Paper 1984:84-GT-159.
- [157] Forsyth, P.R., Gillespie, D.R.H., McGilvray, M. Experimental deposition of NaCl particles from turbulent flows at gas turbine temperatures (2019) Journal of Turbomachinery, 141 (2), art. no. 021001; DOI: 10.1115/1.4041036.
- [158] Libertowski, N.D., Plewacki, N.A., Bons, J.P. The Effect of Temperature and Melting Relative to Particle Deposition in Gas Turbines (2019) AIAA SciTech 2019 Forum 7-11 January 2019, San Diego, California. DOI: 10.2514/6.2019-1951
- [159] Whitaker SM, Prenter R, Bons JP. The Effect of Free-Stream Turbulence on Deposition for Nozzle Guide Vanes. J Turbomach 2015;137:121001.
- [160] Bons JP, Wammack JE, Crosby J, Fletcher D, Fletcher TH. Evolution of Surface Deposits on a High Pressure Turbine Blade, Part I: Convective Heat Transfer. J Turbomach 2008;130:021021.
- [161] Lawson SA, Thole KA. The Effects of Simulated Particle Deposition on Film Cooling. ASME Paper 2009:GT2009-59109.
- [162] Wood EJ, Ng WF, Vandsburger U, LePera S. Simulated Syngas Ash Deposits a Flat Plate Using Teflon and PVC Particles. ASME Paper 2010:GT2010-22445.
- [163] Lawson TB, Thole KA. Simulations of Multi-Phase Particle Deposition on Endwall Film-Cooling. J Turbomach 2012;134:011003.
- [164] Liu, Z., Liu, Z., Zhang, F., Liu, Y. An Experimental Study on the Effects of a Film Cooling Configuration and Mainstream Temperature on Depositing (2019) Journal of Thermal Science. DOI: <https://doi.org/10.1007/s11630-019-1087-7>
- [165] Bell I.H., Wronski J., Quoilin S., Lemort V. Pure and pseudo-pure fluid thermophysical property evaluation and the open-source thermophysical property library CoolProp (2014) Industrial & Engineering Chemistry Research; 53(6), pp. 2498–508. DOI: 10.1021/ie4033999.
- [166] Kline SJ, McClintock FA. Describing Uncertainties in Single-Sample Experiments. Mech Eng 1953:3.
- [167] Coleman HW, Steele WG. Experimentation and Uncertainty Analysis for Engineers. 2nd ed. New Jersey: Wiley Interscience; 1999.
- [168] Laycock, R.G., Fletcher, T.H. Erratum: “Erratum: ‘Time-Dependent Deposition Characteristics of Fine Coal Fly Ash in a Laboratory Gas Turbine Environment’ [ASME J. Turbomach., 2012, 135(2), p. 021003; DOI:10.1115/1.4006639]” [ASME. J.Turbomach., 2017, 139(12), p. 127001; DOI: 10.1115/1.4037911]
- [169] Lee, B.E., Fletcher, C.A.J., Shin, S.H., Kwon, S.B. Computational study of fouling deposit due to surface-coated particles in coal-fired power utility boilers (2002) Fuel, 81 (15), pp. 2001–2008. DOI: 10.1016/S0016-2361(02)00127-8
- [170] Verein Deutscher Eisenhüttenleute. Slag Atlas. 2nd Edition. Dusseldorf. Verlag Stahleisen GmbH 1995 ISBN: 3514004579 9783514004573.
- [171] Bandyopadhyay, R., Gupta, S., Lindblom, B., Jonsson, S., French, D., Sahajwalla, V. Assessment of ash deposition tendency in a rotary kiln using Thermo-mechanical analysis and Experimental Combustion Furnace (2014) Fuel, 135, pp. 301–307. DOI: 10.1016/j.fuel.2014.06.064
- [172] Ciprian D, Grigore B. Classification and Characterization of Basalts of Branisca and Dobra – Romania, for Capitalization. Recent Advances in Industrial and Manufacturing Technologies 2009:64–69 (ISBN: 978-1-61804-186-9).
- [173] Taylor HE, Lichte FE. Chemical Composition of Mount St. Helens Volcanic Ash. Geophysical Research Letters 1980;7:949–52.
- [174] Song W, Lavallée Y, Wadsworth FB, Hess KH, Dingwell DB. Wetting and Spreading of Molten Volcanic Ash in Jet Engines. J Phys Chem Lett 2017;8:1878–84.
- [175] Portnikov, D., Kalman, H. Determination of elastic properties of particles using single particle compression test (2014) Powder Technology, 268, pp. 244–252. DOI: 10.1016/j.powtec.2014.08.011
- [176] Bas M.J.L., Maitre R.W.L., Streckeisen A., Zanettin B. A chemical classification of volcanic rocks based on the total alkali-silica diagram (1986) Journal of Petrology, 27 (3), pp. 745–750. DOI: 10.1093/petrology/27.3.745.
- [177] Ravi V, Jog MA, Manglik RM. (2010) Effects of Interfacial and Viscous Properties of Liquids on Drop Spread Dynamics. ILASS Americas, 22nd Annual Conference on Liquid Atomization and Spray Systems, Cincinnati, OH, May 2010.
- [178] Madejski, J. Solidification of droplets on a cold surface. (1976) International Journal of Heat and Mass Transfer, 19 (9), pp. 1009–1013. DOI: 10.1016/0017-9310(76)90183-6.
- [179] Buckingham, E.. (1914). On Physically Similar Systems; Illustrations of the Use of Dimensional Equations. Physical Review, 4, pp. 345–376.

- [180] Tabakoff W, Hamed A, Metwally M, Pasin M. High-Temperature Erosion Resistance of Coatings for Gas Turbine. *J Eng Gas Turbines Power* 1992;114:242–9.
- [181] Tabakoff W. Review-Turbomachinery Performance Deterioration Exposed to Solid Particulates Environment. *J Fluids* 1984;106:125–34.
- [182] Kotwal R, Tabakoff W. A New Approach for Erosion Prediction Due to Fly Ash. ASME Paper 1980:800-GT-96.
- [183] Casari N, Pinelli M, Suman A, di Mare L, Montomoli F. EBFOG: Deposition, Erosion, and Detachment on High-Pressure Turbine Vanes. *ASME. J. Turbomach.* 2018;140(6):061001-061001-9. doi:10.1115/1.4039181
- [184] Mills KC, Hayashi M, Wang L, Watanabe T. The structure and properties of silicate slags. In: Seetharaman S, McLean A, Guthrie R, editors. *Treatise on process metallurgy, Volume 1: Process fundamentals*, Amsterdam: Elsevier Ltd; 2014, p. 149–286.
- [185] Singh T., Sundararajan G. The erosion behavior of 304 stainless steel at elevated temperatures (1990) *Metallurgical Transactions A*, 21 (12), pp. 3187–3199. DOI: 10.1007/BF02647314.
- [186] Sundararajan G., Roy M. Solid particle erosion behaviour of metallic materials at room and elevated temperatures (1997) *Tribology International*, 30 (5), pp. 339–359. DOI: 10.1016/S0301-679X(96)00064-3.
- [187] Wellman R.G., Nicholls J.R. High temperature erosion-oxidation mechanisms, maps and models (2004) *Wear*, 256 (9-10), pp. 907–917. DOI: 10.1016/j.wear.2003.04.003.
- [188] Finnie, I. Erosion of surfaces by solid particles (1960) *Wear*, 3 (2), pp. 87-103. DOI: 10.1016/0043-1648(60)90055-7
- [189] Hamed A, Tabakoff W. Erosion and Deposition in Turbomachinery. *J Propul Power* 2006;22:350–60.
- [190] Shin D, Hamed A. Advanced High Temperature Erosion Tunnel for Testing TBC and New Turbine Blade Materials. ASME Paper 2016:GT2016-57922. DOI: 10.1115/GT2016-57922
- [191] Goodwin JE, Sage W, Tilly GP. Study of erosion by solid particles. *Proc Instn Mech Engrs* 1969;184:279–92.
- [192] Bitter JGA. A Study of Erosion Phenomena, Part I. *Wear* 1963;6:5–21.
- [193] Henry C, Minier JP. Progress in particle resuspension from rough surfaces by turbulent flows. *Prog Energy Combust Sci*, 2014;45:1–53.
- [194] Wenzel RN. Resistance of Solid Surfaces to Wetting by Water *Ind Eng Chem* 1936;8:988–94.
- [195] Cassie ABD, Baxter S. Wettability of Porous Surfaces. *Trans. Faraday Soc* 1944;40:546–51.
- [196] Blossey R. Self-Cleaning Surfaces – Virtual Realities. *Nat Mater* 2003;2:301–6.
- [197] Sacco C., Bowen C., Lundgreen R., Bons J.P., Ruggiero E., Allen J., Bailey J. Dynamic similarity in turbine deposition testing and the role of pressure (2017) *Proceedings of the ASME Turbo Expo*, 2D-2017. DOI: 10.1115/GT2017-64961.
- [198] Poppe T, Blum J, Henning T. Analogous experiments on the stickiness of micron-sized preplanetary dust. *The Astrophysical Journal* 2000;533:454–71.
- [199] Tarabrin A.P., Schurovsky V.A., Bodrov A.I., Stalder J.-P. Influence of axial compressor fouling on gas turbine unit performance based on different schemes and with different initial parameters (1998) *Proceedings of the ASME Turbo Expo*, 4. DOI: 10.1115/98-GT-416
- [200] Syverud E., Brekke O., Bakken L.E. Axial compressor deterioration caused by saltwater ingestion. (2007) *Journal of Turbomachinery*, 129 (1), pp. 119–126. DOI: 10.1115/1.2219763.
- [201] Kurz R., Musgrove G., Brun K. Experimental evaluation of compressor blade fouling. (2017) *Journal of Engineering for Gas Turbines and Power*, 139 (3), art. no. 032601, DOI: 10.1115/1.4034501.
- [202] Vigueras Zuniga M. O., Analysis of Gas Turbine Compressor Fouling and Washing on Line (2007) Ph.D. thesis, Cranfield University, Cranfield, UK.
- [203] Carpenter LK, Crouse Jr. FW, Halow JS. Coal-Fueled Turbines: Deposition Research. ASME Paper 1985:85-GT-213.
- [204] Freeman, A. and Kaufman, E., “Considerations When Burning Ash-Bearing Fuels in Heavy-Duty Gas-Turbines,” GE Power Systems report 3764, Schenectady, NY, May 1993.
- [205] Delimont JM, Murdock MK, Ng WF, Ekkad SV. Effect of Temperature on Microparticle Rebound Characteristics at Constant Impact Velocity—Part I. *J Eng Gas Turbines Power* 2015;137:112603.
- [206] Delimont JM, Murdock MK, Ng WF, Ekkad SV. Effect of Temperature on Microparticle Rebound Characteristics at Constant Impact Velocity—Part II. *J Eng Gas Turbines Power* 2015;137:112604.
- [207] Reagle CJ, Delimont JM, Ng WF, Ekkad SV. Study of Microparticle Rebound Characteristics Under High Temperature Conditions. *J Eng Gas Turbines Power* 2014;136:011501.
- [208] Oka YI, Miyata H. Erosion behaviour of ceramic bulk and coating materials caused by water droplet impingement. *Wear* 2009;267:1804–10.
- [209] Ahmad M, Casey M, Surken N. Experimental assessment of droplet impact erosion resistance of steam turbine blade materials. *Wear* 2009;267:1605–18.
- [210] Hackworth JV. Damage of infrared-transparent materials exposed to rain environments at high velocities. *Proc. SPIE* 1983;0362:123–36.
- [211] Duffy JA, Ingram MD. Optical basicity—IV: Influence of electronegativity on the Lewis basicity and solvent properties of molten oxyanion salts and glasses. *J Inorg Nucl Chem* 1975;37:1203–6.

- 1977 [212] Zhang GH, Chou KC. Simple Method for Estimating the Electrical Conductivity of Oxide Melts with Optical Basicity. Metall
1978 Mater Trans B 2010;41:131–6.
- 1979 [213] Urbain G, Cambier F, Deletter M, Anseau MR. Viscosity of Silicate Melts. Trans J Br Ceram Soc 1981;80:139–41.
- 1980 [214] Senior CL, Srinivasachar S. Viscosity of Ash Particles in Combustion Systems for the Prediction of Particle Sticking. Energy
1981 Fuels 1995;9:277–83.
- 1982 [215] Casaday BP, Ameri AA, Bons JP. Numerical Investigation of Ash Deposition on Nozzle Guide Vane Endwalls. ASME J. Eng.
1983 Gas Turbines Power, 2013;135:032001.
- 1984 [216] Borello D, Cardillo L, Corsini A, Delibra G, Rispoli G, Salvagni A, Sheard G, Venturini P. Modelling of Particle Transport,
1985 Erosion and Deposition in Power Plant Gas Paths. ASME Paper2016:GT2016-57984.
- 1986

Appendix A

In the present Appendix, the constitutive equations of the seven (7) viscosity methods with all model coefficients and applicability limits are reported. In the following equations, viscosity values are expressed in [Pa s] while temperature values are expressed in [K].

A.1. NPL model

The first method, called the NPL model (National Physical Laboratory) [69], is based on the optical basicity. The optical basicity is a quantity related to the mole fraction χ and number of oxygen atoms n in the melt and is used to classify oxides on a scale of acidity referred to the same O^{2-} base. Optical Basicity of glasses and slags is derived from the Lewis acidity/basicity concept. The expression of the Non-Corrected (NC) optical basicity Λ^{NC} is

$$\Lambda^{NC} = \frac{\sum \chi_i n_i \Lambda_i}{\sum \chi_i n_i} \quad (A1)$$

where the values of the theoretical optical basicity Λ are listed in Table A1.

Table A1 – Values of the theoretical basicity Λ

K ₂ O	Na ₂ O	CaO	MgO	Al ₂ O ₃	TiO ₂	SiO ₂	Fe ₂ O ₃
1.40	1.15	1.00	0.78	0.60	0.61	0.48	0.75

Optical basicity can be corrected for the cations required for the charge balance of the aluminum oxide according to the correction proposed by Duffy and Ingram [211], used in [212], the Corrected (C) optical basicity Λ^C is calculated as

$$\chi_{CaO} \geq \chi_{Al_2O_3}$$

$$\Lambda^C = \frac{1 \Lambda_{CaO} (\chi_{CaO} - \chi_{Al_2O_3}) + 2 \Lambda_{SiO_2} \chi_{SiO_2} + 3 \Lambda_{Al_2O_3} \chi_{Al_2O_3} + 1 \Lambda_{MgO} \chi_{MgO} + 3 \Lambda_{Fe_2O_3} \chi_{Fe_2O_3} + 1 \Lambda_{Na_2O} \chi_{Na_2O} + 1 \Lambda_{K_2O} \chi_{K_2O} + 2 \Lambda_{TiO_2} \chi_{TiO_2}}{1(\chi_{CaO} - \chi_{Al_2O_3}) + 2 \chi_{SiO_2} + 3 \chi_{Al_2O_3} + 1 \chi_{MgO} + 3 \chi_{Fe_2O_3} + 1 \chi_{Na_2O} + 1 \chi_{K_2O} + 2 \chi_{TiO_2}} \quad (A2)$$

$$\Lambda^C = \frac{1 \Lambda_{MgO} \Lambda_{CaO} (\chi_{CaO} + \chi_{MgO} - \chi_{Al_2O_3}) + 2 \Lambda_{SiO_2} \chi_{SiO_2} + 3 \Lambda_{Al_2O_3} \chi_{Al_2O_3} + 3 \Lambda_{Fe_2O_3} \chi_{Fe_2O_3} + 1 \Lambda_{Na_2O} \chi_{Na_2O} + 1 \Lambda_{K_2O} \chi_{K_2O} + 2 \Lambda_{TiO_2} \chi_{TiO_2}}{1(\chi_{CaO} + \chi_{MgO} - \chi_{Al_2O_3}) + 2 \chi_{SiO_2} + 3 \chi_{Al_2O_3} + 3 \chi_{Fe_2O_3} + 1 \chi_{Na_2O} + 1 \chi_{K_2O} + 2 \chi_{TiO_2}} \quad (A3)$$

The correction for optical basicity is not required when $\chi_{CaO} + \chi_{MgO} \leq \chi_{Al_2O_3}$ because at this condition, the aluminum oxide will behave as basic oxide and the Al^{3+} ions will not incorporated into the Si^{4+} chain or rig. In this case, the Eq (A1) is applied as is, without correction.

The NPL method can be applied to all of the materials considered in the present work estimates the viscosity according to

$$\ln \mu = \ln A_{NPL} + \frac{B_{NPL}}{T} \quad (A4)$$

This model is generally applicable and not limited to slag of a certain composition. The coefficients A and B can be calculated according to the expressions

$$\ln \frac{B_{NPL}}{1000} = -1.77 + \frac{2.88}{(\Lambda^C \text{ or } \Lambda^{NC})} \quad (A5)$$

$$\ln A_{NPL} = -232.69(\Lambda^C \text{ or } \Lambda^{NC})^2 + 357.32(\Lambda^C \text{ or } \Lambda^{NC}) - 144.17 \quad (A6)$$

The accuracy of the present method is not reported in the original work [69]. However, by using the data proposed by Duffy and Ingram [211], it is possible to estimate the deviations between the theoretical and the experimental optical basicity values. The data refers to glassy materials and they are reported in Figure A1. The confidence band is ± 8.7 % wide and it is representative of the maximum deviation between theoretical and experimental values (dashed lines in the graph).

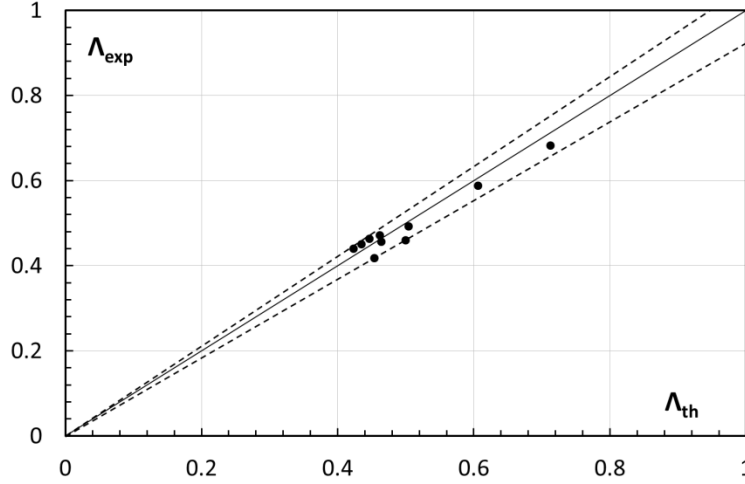


Figure A1 – Deviations between the theoretical and the experimental optical basicity values taken from Duffy and Ingram [211]

A.2. Modified silica ratio model

The second method is the modified silica ratio S^2 model [70]. The S^2 is based on studies of coal ash slags, containing silicon, aluminum, iron, calcium and magnesium as major components. The model relates the viscosity-temperature characteristics of liquid slags with their chemical composition, and it is based on a recalculation of the compositional analysis of the slag in which all ferrous is assumed in the presence of Fe_2O_3 according to the weight fraction

$$SiO_2 + Al_2O_3 + \text{Equiv. } Fe_2O_3 + CaO + MgO = 100 \% \quad (A7)$$

The silica ratio ζ is calculated on a weight basis

$$\zeta = \frac{100 SiO_2}{SiO_2 + \text{Equiv. } Fe_2O_3 + CaO + MgO} \quad (A8)$$

and the viscosity value can be calculated using

$$\log \mu = 4.468 \left(\frac{\zeta}{100} \right)^2 + 1.265 \frac{10^4}{T} - 8.44 \quad (A9)$$

As reported in [70], the model coefficients reported in Eq. (A9) were calculated by data regression of the temperature-viscosity trends based on sixty-two (62) samples of slags that covered the range of chemical composition in term of weight fraction listed below:

- $SiO_2 = (31 - 59) \text{ wt\%};$
- $CaO = (1 - 37) \text{ wt\%};$
- $Al_2O_3 = (19 - 37) \text{ wt\%};$
- $Fe_2O_3 = (0 - 38) \text{ wt\%};$
- $MgO = (1 - 12) \text{ wt\%};$
- $Na_2O+K_2O = (1 - 5) \text{ wt\%}.$

In addition, the model is valid when the silica ratio value is in the range of 45 – 75 and the value of the ratio SiO_2/Al_2O_3 is in the range of 1.2 – 2.3. These values represent the applicability limits of the present model. The model will be applied only for the gas turbine contaminants which chemical composition match with the listed limits.

This model is the oldest considered in the present review. Its accuracy is estimated in [70] and in [68] by considering the predicted temperature correspondent to a determined viscosity value. In both cases, the model underpredicts the temperature values. In particular, Hoy et al. [70] estimated an accuracy band of 44 K while Vargas et al. [68] estimated an accuracy band of 66 K. All the predicted points correspond to a lower temperature than the experimental data. This means that for a given temperature, the S^2 predict a lower value of particle viscosity.

A.3. Slope and intercept model

The third method is based on the slope and intercept model, usually called Watt and Fereday (WF) model [71]. The basis of the model is a recalculation of the composition identical to that of the S^2 model, reported in the Eq.(A7). The viscosity can be calculated according to

$$\log \mu = \frac{m_{WF} 10^7}{(T - 423)^2} + c_{WF} \quad (A10)$$

The two parameters, m_{WF} and c_{WF} , should be calculated from the species concentrations recalculated in weight percent according to the following expressions

$$m_{WF} = 0.00835 \text{ SiO}_2 + 0.00601 \text{ Al}_2\text{O}_3 - 0.109 \quad (\text{A11})$$

$$c_{WF} = 0.0415 \text{ SiO}_2 + 0.0192 \text{ Al}_2\text{O}_3 + 0.0276 \text{ Fe}_2\text{O}_3 + 0.0160 \text{ CaO} - 3.92 \quad (\text{A12})$$

The correlation was derived by data regression of British coal ashes on the basis of measurements on one hundred and thirteen (113) ashes samples that covered the range of chemical composition in terms of weight fraction listed below:

- $\text{SiO}_2 = (30 - 60) \text{ wt\%}$;
- $\text{CaO} = (2 - 30) \text{ wt\%}$;
- $\text{Al}_2\text{O}_3 = (15 - 35) \text{ wt\%}$;
- $\text{Fe}_2\text{O}_3 = (0 - 30) \text{ wt\%}$;
- $\text{MgO} = (1 - 10) \text{ wt\%}$.

In addition, the model is valid when the silica ratio value is in the range of 40 – 80 and the value of the ratio $\text{SiO}_2/\text{Al}_2\text{O}_3$ is in the range of 1.4 – 2.4. These values represent the applicability limits of the present model. The model will be applied only for the gas turbine contaminants which chemical composition match with the listed limits.

As mentioned, this model is based on the S^2 model, and in the same way, underpredicts the temperature for a determined viscosity value. In particular, for a viscosity equal to 25 Pa s this model underpredicts the temperature values up to 180 K [68]. In the work of Watt and Fereday [71] there is a detailed description of the uncertainty related to three sources (instrumental error, analytical error, and error due to irregularities in the behavior of the slag). A confidence band equal to $\pm 0.29 \log$ unit in Poise at 95 % is also indicated by the Authors [71].

A.4. Urbain model

The fourth method is based on Urbain's formulation [213] used for the viscosity estimation of silicate and aluminosilicates melts at high temperature. An improved physical model of this formulation is proposed by Senior and Srinivasachar [214] extending the validity of the equation to low temperature. The same temperature-composition correlation is applied by Sreedharan and Tafti (S&T) [72]. Starting from this formulation, the particle viscosity is calculated with adjusted coefficients reported in [68] obtained for predicting the viscosity of ash particles in combustion systems up to 10^9 Pa s. This model is used to predict particle viscosity in several studies related to particle impact/deposition on gas turbine hot sections [23], [28], [215] and [216]. This model is able to predict the particle viscosity with the following limits:

- $\text{SiO}_2 = (0 - 60) \text{ wt\%}$;
- $\text{Al}_2\text{O}_3 = (0 - 60) \text{ wt\%}$;
- $\text{Fe}_2\text{O}_3 = (0 - 30) \text{ wt\%}$;

Particle viscosity can be calculated according to the expression

$$\log \left(\frac{\mu}{T} \right) = A_{S\&T} + \frac{10^3 B_{S\&T}}{T} \quad (\text{A13})$$

The terms $A_{S\&T}$ and $B_{S\&T}$ vary based on ash composition. The parameter describing this compositional dependence in terms $A_{S\&T}$ and $B_{S\&T}$ are referred to by the acronym NBO/T which stands for non-bridging oxygen to tetrahedral oxygen where the oxides are considered with their mole fraction values.

$$\frac{NBO}{T} = \frac{\chi_{\text{CaO}} + \chi_{\text{MgO}} + \chi_{\text{FeO}} + \chi_{\text{Na}_2\text{O}} + \chi_{\text{K}_2\text{O}} - \chi_{\text{Al}_2\text{O}_3} - \chi_{\text{Fe}_2\text{O}_3}}{\frac{\chi_{\text{SiO}_2} + \chi_{\text{TiO}_2}}{2} + \chi_{\text{Al}_2\text{O}_3} + \chi_{\text{Fe}_2\text{O}_3}} \quad (\text{A14})$$

The model constant $A_{S\&T}$ and $B_{S\&T}$ depend on the value of NBO/T. In particular

$$A_{S\&T} = -3.81629 - 0.46341 B_{S\&T} - 0.35342 \frac{NBO}{T} \quad (\text{A15})$$

where $B_{S\&T}$ is defined according to the expression

$$B_{S\&T} = b_0 + \alpha b_1 + \alpha^2 b_2 + N(b_3 + \alpha b_4 + \alpha^2 b_5) + N^2(b_6 + \alpha b_7 + \alpha^2 b_8) + N^3(b_9 + \alpha b_{10} + \alpha^2 b_{11}) \quad (\text{A16})$$

where N is the molar fraction of the silica dioxide χ_{SiO_2} and α is defined according to

$$\alpha = \frac{\chi_{\text{CaO}}}{\chi_{\text{CaO}} + \chi_{\text{Al}_2\text{O}_3}} \quad (\text{A17})$$

The coefficients b_i are defined according to the values reported in Table A2.

Table A2 – Coefficients of $B_{S\&T}$ according to the S&T model [72]

b_0	-224.98	b_4	-2398.32	b_8	-2551.71
b_1	636.67	b_5	1650.56	b_9	387.32
b_2	-418.7	b_6	-957.94	b_{10}	-1722.24
b_3	823.89	b_7	3366.61	b_{11}	1432.08

In order to evaluate the accuracy of this model, it is necessary to make reference to the earlier model proposed by Urbain et al. [213]. With the isothermal deformation method, the uncertainty related to the viscosity values is equal to $\pm 10\%$ [68]. By considering the prediction of temperature values for a given viscosity, the confidence band is ± 4.5 K wide for temperature values higher than 1873 K, while is ± 10 K wide for temperature values lower than 1875 K.

A.5. RRLG method

The fifth method proposed by Riboud et al. (RRLG) [73] is based on Urbain's model [213]. The viscosity is calculated according to the expression

$$\log\left(\frac{\mu}{T}\right) = A_{\text{RRLG}} + \frac{10^3 B_{\text{RRLG}}}{T} \quad (\text{A18})$$

The model coefficients A_{RRLG} and B_{RRLG} can be calculated using the molar fractions of the materials components using the following expressions

$$\ln A_{\text{RRLG}} = -35.76 \chi_{\text{Al}_2\text{O}_3} + 1.73(\chi_{\text{CaO}} + \chi_{\text{MgO}}) + 7.02(\chi_{\text{Na}_2\text{O}} + \chi_{\text{K}_2\text{O}}) - 19.81 \quad (\text{A19})$$

$$B_{\text{RRLG}} = 68.833 \chi_{\text{Al}_2\text{O}_3} - 23.896(\chi_{\text{CaO}} + \chi_{\text{MgO}}) - 39.159(\chi_{\text{Na}_2\text{O}} + \chi_{\text{K}_2\text{O}}) - 31.14 \quad (\text{A20})$$

This model was obtained by considering twenty-two (22) industrial continuous casting slag samples and the applicability limits of this model in terms of weight fraction is listed below:

- $\text{SiO}_2 = (27 - 56)$ wt%;
- $\text{CaO} = (8 - 46)$ wt%;
- $\text{Al}_2\text{O}_3 = (0 - 12)$ wt%;
- $\text{Na}_2\text{O} = (0 - 22)$ wt%.

As reported in [73] the accuracy of the present model is related to the third term of the Eq. (A20). In their work, the Authors showed a relative difference with a maximum deviation equal to 2.9 % for a viscosity value lower than 2 Pa s.

A.6. SDS method

The sixth method proposed by Streeter, Diehl, and Schobert (SDS) [74] is based on Urbain's model [213] by considering three (3) different categories according to the silica content. The Authors in [74] proposed a correction term based on viscosity measurement of seventeen (17) Western US lignite and sub-bituminous coal slags belonging to low-rank coal over the temperature range of (1423 – 1753) K. The viscosity is calculated according to the expression

$$\ln\left(\frac{\mu}{T}\right) = \ln A_U + \frac{10^3 B_U}{T} - \Delta \quad (\text{A21})$$

where the model coefficients A_U and B_U are defined according to Urbain's model [213] as

$$-\ln A_U = 0.2693 B_U + 11.6725 \quad (\text{A22})$$

$$B_U = b_{0,U} + \chi_{\text{SiO}_2} b_{1,U} + \chi_{\text{SiO}_2}^2 b_{2,U} + \chi_{\text{SiO}_2}^3 b_{3,U} \quad (\text{A23})$$

where the model coefficient $b_{i,U}$ are defined according to the following expressions

$$b_{0,U} = 13.8 + 39.9355\alpha - 44.049\alpha^2 \quad (\text{A24})$$

$$b_{1,U} = 30.481 - 117.1505\alpha - 129.9978\alpha^2 \quad (\text{A25})$$

$$b_{2,U} = -40.9429 - 234.0486\alpha - 300.04\alpha^2 \quad (\text{A26})$$

$$b_{3,U} = 60.7619 - 1539276\alpha - 211.1616\alpha^2 \quad (\text{A27})$$

where α is defined according to the Eq. (A17). The value of Δ is dependent on the silica content of the melt

$$\Delta = T m_{\text{SDS}} + c_{\text{SDS}} \quad (\text{A28})$$

Therefore, starting with these definitions, in the case of $B_U > 28$ the model coefficients of SDS are

$$10^3 m = -1.7264 F + 8.4404 \quad (\text{A29})$$

$$c = -1.7137(10^3 m) + 0.0509 \quad (\text{A30})$$

$$F = \frac{\chi_{\text{SiO}_2}}{\chi_{\text{CaO}} + \chi_{\text{MgO}} + \chi_{\text{Na}_2\text{O}} + \chi_{\text{K}_2\text{O}}} \quad (\text{A31})$$

In the case of $B_U < 28$ and $B_U > 24$ the model coefficients of SDS are

$$10^3 m = -1.3101 F + 9.9279 \quad (\text{A32})$$

$$c = -2.0356(10^3 m) + 1.1094 \quad (\text{A33})$$

$$F = B_U(\chi_{\text{Al}_2\text{O}_3} + \chi_{\text{FeO}}) \quad (\text{A34})$$

while in the case of $B_U < 24$ the model coefficients of SDS are

$$10^3 m = -55.3649 F + 37.9186 \quad (\text{A35})$$

$$c = -1.8244(10^3 m) + 0.9416 \quad (\text{A36})$$

$$F = \frac{\chi_{\text{CaO}}}{\chi_{\text{CaO}} + \chi_{\text{MgO}} + \chi_{\text{Na}_2\text{O}} + \chi_{\text{K}_2\text{O}}} \quad (\text{A37})$$

The compositions of the seventeen (17) coal slags are listed below in terms of molar fractions:

- $\chi_{\text{SiO}_2} = 0.25 - 0.70$;
- $\chi_{\text{CaO}} = 0.08 - 0.33$;
- $\chi_{\text{Al}_2\text{O}_3} = 0.08 - 0.27$;
- $\chi_{\text{Na}_2\text{O}} = 0.00 - 0.11$;
- $\chi_{\text{MgO}} = 0.04 - 0.13$;
- $\chi_{\text{Fe}_2\text{O}_3} = 0.00 - 0.09$.

and represent the limits of applicability of the SDS model. In addition, the weight percentage of the minor constituent (K_2O , TiO_2) has to be lower than 5 %. The Authors [74] have reported a detailed explanation of the correlation coefficient for each category defined according to the silica content ranging from 0.870 to 0.999.

A.7. GRD Model

The last viscosity model is the model proposed by Giordano et al. [75] which is used to calculate the volcanic ashes viscosity according to the following procedure. The former relation is

$$\ln \mu = \ln A_{\text{GRD}} + \frac{B_{\text{GRD}}}{T - C_{\text{GRD}}} \quad (\text{A38})$$

where the temperature is expressed in Kelvin and the particle viscosity in Pa s. The model coefficient A_{GRD} is equal to -4.55 while the coefficients B_{GRD} and C_{GRD} are calculated according to the mol% fraction χ of constituent oxides

$$B_{\text{GRD}} = 159.6(\chi_{\text{SiO}_2} + \chi_{\text{TiO}_2}) - 173.3\chi_{\text{Al}_2\text{O}_3} + 72.1\chi_{\text{Fe}_2\text{O}_3} + 75.7\chi_{\text{MgO}} - 39.0\chi_{\text{CaO}} - 84.1\chi_{\text{Na}_2\text{O}} - 2.43(\chi_{\text{SiO}_2} + \chi_{\text{TiO}_2})(\chi_{\text{Fe}_2\text{O}_3} + \chi_{\text{MgO}}) - 0.91(\chi_{\text{SiO}_2} + \chi_{\text{TiO}_2} + \chi_{\text{Al}_2\text{O}_3})(\chi_{\text{Na}_2\text{O}} + \chi_{\text{K}_2\text{O}}) + 17.6\chi_{\text{Al}_2\text{O}_3}(\chi_{\text{Na}_2\text{O}} + \chi_{\text{K}_2\text{O}}) \quad (\text{A39})$$

$$C_{\text{GRD}} = 2.75\chi_{\text{SiO}_2} + 15.7(\chi_{\text{TiO}_2} + \chi_{\text{Al}_2\text{O}_3}) + 8.3(\chi_{\text{Fe}_2\text{O}_3} + \chi_{\text{MgO}}) + 10.2\chi_{\text{CaO}} - 12.3(\chi_{\text{Na}_2\text{O}} + \chi_{\text{K}_2\text{O}}) + 0.3(\chi_{\text{Al}_2\text{O}_3} + \chi_{\text{Fe}_2\text{O}_3} + \chi_{\text{MgO}} + \chi_{\text{CaO}})(\chi_{\text{Na}_2\text{O}} + \chi_{\text{K}_2\text{O}}) \quad (\text{A40})$$

According to Giordano et al. [75] the model is calibrated by means of 1774 experimentally measured pairs of values of temperature-viscosity on silicate melts of known composition within the following ranges:

- $\text{SiO}_2 = (41 - 79) \text{ wt\%}$;
- $\text{CaO} = (0 - 26) \text{ wt\%}$;
- $\text{Al}_2\text{O}_3 = (0 - 23) \text{ wt\%}$;
- $\text{Fe}_2\text{O}_3 = (0 - 12) \text{ wt\%}$;
- $\text{MgO} = (0 - 32) \text{ wt\%}$;
- $\text{Na}_2\text{O} = (0 - 11) \text{ wt\%}$;
- $\text{K}_2\text{O} = (0.3 - 9) \text{ wt\%}$;
- $\text{Ti}_2\text{O} = (0 - 3) \text{ wt\%}$.

In [75] a detailed description of the accuracy of the model coefficient A_{GRD} is reported. In addition, the data comparison reported by the Authors showed a root-mean-square-error equal to 0.4 log unit.

Table A3 summarizes the constitutive equations and the applicability limits of all viscosity models.

Table A3 – Constitutive equations and the applicability limits of the viscosity models

	Constitutive equations		SiO_2	CaO	Al_2O_3	Fe_2O_3	MgO	Na_2O	K_2O
NPL [69]	$\ln \mu = \ln A_{\text{NPL}} + \frac{B_{\text{NPL}}}{T}$		-	-	-	-	-	-	-
S²* [70]	$\log \mu = 4.468 \left(\frac{\zeta}{100} \right)^2 + 1.265 \frac{10^4}{T} - 8.44$	wt%	31 – 59	1 – 37	19 – 37	0 – 38	1 – 12	-	-
WF²* [71]	$\log \mu = \frac{m_{\text{WF}} 10^7}{(T - 423)^2} + c_{\text{WF}}$	wt%	30 – 60	2 – 30	15 – 35	0 – 30	1 – 10	-	-
S&T [72]	$\log \left(\frac{\mu}{T} \right) = A_{\text{S\&T}} + \frac{10^3 B_{\text{S\&T}}}{T}$	wt%	< 60	-	< 60	< 15	-	-	-
RRLG [73]	$\log \left(\frac{\mu}{T} \right) = A_{\text{RRLG}} + \frac{10^3 B_{\text{RRLG}}}{T}$	wt%	27 – 56	8 – 46	0 – 12	-	-	0 – 22	-
SDS³* [74]	$\ln \left(\frac{\mu}{T} \right) = \ln A_{\text{U}} + \frac{10^3 B_{\text{U}}}{T} - \Delta$	χ	0.25 – 0.70	0.08 – 0.33	0.08 – 0.27	0.00 – 0.09	0.04 – 0.13	0.00 – 0.11	-
GRD [75]	$\ln \mu = \ln A_{\text{GRD}} + \frac{B_{\text{GRD}}}{T - C_{\text{GRD}}}$	wt%	41 – 79	0 – 26	0 – 23	0 – 12	0 – 32	0 – 11	0.3 – 9

* The model is valid if $45 \leq \zeta \leq 75$; $1.2 \leq \text{SiO}_2/\text{Al}_2\text{O}_3 \leq 2.3$; $1 \leq \text{Na}_2\text{O} + \text{K}_2\text{O} \leq 6$ in terms of wt%

²* The model is valid if $40 \leq \zeta \leq 80$; $1.4 \leq \text{SiO}_2/\text{Al}_2\text{O}_3 \leq 2.4$ in terms of wt%

³* The model is valid if $\text{K}_2\text{O} \leq 5$; $\text{TiO}_2 \leq 5$ in terms of wt%

Appendix B

The particle deposition tests collected in Tables 4 – 6 are reported in this Appendix with the reference of particle Stokes number and particle relaxation time values. For each test, the geometric features of the target are included in the related reference. Particle Stokes number is calculated according to

$$St = \frac{\rho d^2 v}{18 \mu_g L} \quad (B1)$$

where the characteristic target length L is affected by inaccuracy as reported below. Particle relaxation time is not affected by these inaccuracies and is calculated according to

$$\tau = \frac{\rho d^2}{18 \mu_g} \quad (B2)$$

In the presence of a certain variability range of particle diameter and temperature, a single average value is assumed as representative of the entire test. The values of the former variables of Stokes number and particle relaxation time are reported in Tables B1 – B3 as well as the type of target and its shape. In several cases, the geometric characteristics of the target are not reported in detail and for this reason, they are estimated using sketches and figures reported in the correspondent reference with unavoidable inaccuracies. In these cases, the target dimensions reported in Tables B1 – B3 are marked with a cross.

According to the type of target, the characteristic length L is calculated according to the following rules:

- tests performed on a full-scale gas turbine (T): a representative chord equal to 50 mm was assumed as characteristic length L for all the tests, excluding the tests called EYJA (Naraparaju *et al.* [150]) and Laki 5 (Shinozaki *et al.* [149]) for which the chord of the first nozzle was estimated using the sketch reported in the reference;
- tests performed on wind tunnels provided with cascade or single blade targets (B): the airfoil chord was assumed as characteristic length L ;
- tests performed using a coupon (C): the diameter (if circular) or the hydraulic diameter (if rectangular) of the coupon holder were assumed as the characteristic length L ;
- tests performed in order to discover particle deposition inside the internal cooling hole (I): the diameter of the circular holes was assumed as characteristic length L .

The dynamic viscosity of the carrier gas is assumed equal to that of pure air at the same temperature and calculated according to CoolProp library [165] for a reference pressure (absolute) equal to 2 bar. In some tests, the carrier gas came from a combustion chamber in which natural gas or other types of fuels (syngas or heavy fuels) were burned.

For all of these reasons, the Stokes number and particle relaxation time, as well as the characteristics length L reported in Tables B1 – B3, are only useful for an order of magnitude analysis.

Table B1 – Dynamic characteristics of the silty particle impacts: Stokes number and particle relaxation time

	Authors	Material	d [μm]	ρ [kg/m ³]	v [m/s]	T [K]	$\mu \times 10^5$ [Pa s]	TT	Target	L [m]	St	τ [s]
2017	Barker <i>et al.</i> [123]	ARD	22.5	2560	80	1373	5.32	C	(63.5 × 38.1) mm	0.048	2.27	1.4e-3
	Boulanger <i>et al.</i> [124]	ARD 2	30.0	2560	70	1323	5.19	C	(63.5 × 38.1) mm	0.048	3.62	2.5e-3
	Whitaker <i>et al.</i> [147]	ARD 3	5.0	2560	40	1091	4.58	I	0.635 mm	0.001	4.89	7.8e-5
2016	Boulanger <i>et al.</i> [122]	ARD 4	30.0	2560	70	1323	5.19	C	(63.5 × 38.1) mm	0.048	3.62	2.5e-3
	Whitaker <i>et al.</i> [153]	ARD 5	10.0	2560	21	866	3.94	I	0.635 mm	0.001	11.94	3.6e-4
	Lundgreen <i>et al.</i> [154]	ARD 6	2.5	2560	70	1493	5.62	B	42 mm +	0.042	0.03	1.6e-5

+ Estimated by sketches and pictures

Table B2 – Dynamic characteristics of the volcanic particle impacts: Stokes number and particle relaxation time

	Authors	Material	d [μm]	ρ [kg/m ³]	v [m/s]	T [K]	$\mu \times 10^5$ [Pa s]	TT	Target	L [m]	St	τ [s]
‘18	Naraparaju <i>et al.</i> [150]	EYJA	5.3	849	200	1773	6.29		10.0 mm +	0.010	0.41	2.1e-5
2017	Giehl <i>et al.</i> [145]	Basalt	65.0	2800	15	1573	5.81	C	(20 × 30) mm +	0.024	7.07	1.1e-2
		Andesite	65.0	2600	15	1573	5.81	C	(20 × 30) mm +	0.024	6.56	1.1e-2
		Dacite	65.0	2700	15	1573	5.81	C	(20 × 30) mm +	0.024	6.82	1.1e-2
		Rhyolite	65.0	2500	15	1573	5.81	C	(20 × 30) mm +	0.024	6.31	1.0e-2
		EYJA 2	19.9	849	80	1228	4.95	I	0.675 mm (averaged among 3 tests)	0.001	44.52	3.8e-4
	Wylie <i>et al.</i> [148]	Chaiten VA	19.9	849	80	1228	4.95	I	0.675 mm (averaged among 3 tests)	0.001	44.52	3.8e-4
2018	Dean <i>et al.</i> [144]	Laki	27.5	2400	106	1169	4.79	C	(50 × 30) mm	0.038	5.95	2.1e-3

		Hekla	27.5	1500	106	1169	4.79	C	(50 × 30) mm	0.038	3.72	1.3e-3
		Eldgja	27.5	1900	106	1169	4.79	C	(50 × 30) mm	0.038	4.71	1.7e-3
		Askja	27.5	1400	106	1169	4.79	C	(50 × 30) mm	0.038	3.47	1.2e-3
		Laki 2	40.0	2400	91	1043	4.45	C	(50 × 30) mm ⁺	0.038	11.64	4.8e-3
	Taltavull <i>et al.</i> [143]	Laki 3	40.0	2400	106	1160	4.77	C	(50 × 30) mm ⁺	0.038	12.65	4.5e-3
		Laki 4	40.0	2400	127	1265	5.12	C	(50 × 30) mm ⁺	0.038	14.11	4.2e-3
‘13	Shinozaki <i>et al.</i> [149]	Laki 5	60	2400	365	1343	5.24	T	15 mm ⁺	0.015	223	9.2e-3
		St Helens	23.0	2700	100	1421	5.44	T	50 mm ⁺⁺	0.050	2.92	1.5e-3
‘96	Dunn <i>et al.</i> [142]	Twin Mountain	73.0	2730	100	1421	5.44	T	50 mm ⁺⁺	0.050	29.73	1.5e-2
‘93	Kim <i>et al.</i> [141]	St Helens 2	23.0	2700	100	1444	5.50	T	50 mm ⁺⁺	0.050	2.89	1.4e-3

⁺ Estimated by sketches and pictures

⁺⁺ Assumed as a representative chord of the first turbine section nozzle

Table B3 – Dynamic characteristics of the coal particle impacts: Stokes number and particle relaxation time

	Authors	Material	d [μm]	ρ [kg/m ³]	v [m/s]	T [K]	$\mu \times 10^5$ [Pa s]	TT	Target	L [m]	St	τ [s]
‘16	Laycock and Fletcher [121]	JBPS A	4.0	2330	200	1598	5.87	C	(75 × 75) mm ⁺	0.075	0.09	3.5e-5
‘15	Whitaker <i>et al.</i> [159]	JBPS B	5.6	2320	70	1353	5.27	B	42 mm ⁺	0.042	0.13	7.5e-5
‘14	Prenter <i>et al.</i> [26]	JBPS B	6.5	2320	70	1353	5.27	B	42 mm ⁺	0.042	0.17	1.0e-4
2013	Casaday <i>et al.</i> [151]	JBPS B 2	11.6	2320	79	1366	5.30	B	42 mm ⁺	0.042	0.62	3.3e-4
	Laycock and Fletcher [120]	JBPP	8.0	1980	200	1523	5.69	C	(75 × 75) mm ⁺	0.075	0.33	1.2e-4
2012	Webb <i>et al.</i> [12]	Lignite	12.5	2818	70	1343	5.24	B	42 mm ⁺	0.042	0.78	4.7e-4
		Bituminous	14.1	1980	70	1353	5.27	B	42 mm ⁺	0.042	0.69	4.2e-4
		PRB	18.3	2989	70	1350	5.26	B	42 mm ⁺	0.042	1.76	1.1e-3
		JBPS B 3	12.5	2320	70	1330	5.21	B	42 mm ⁺	0.042	0.64	3.9e-4
	Ai <i>et al.</i> [119]	Coal(bit.)	13.4	1980	170	1456	5.53	C	31.8 mm	0.032	1.91	3.6e-4
	Ai <i>et al.</i> [118]	Coal(bit.) 2	16.0	1980	180	1453	5.52	C	31.8 mm	0.032	2.89	5.1e-4
‘11	Ai <i>et al.</i> [117]	Coal(bit.) 3	9.0	1980	170	1453	5.52	C	31.8 mm	0.032	0.86	1.6e-4
‘10	Smith <i>et al.</i> [152]	Bituminous mean14	14.0	1980	70	1227	4.94	B	42 mm ⁺	0.042	0.73	4.4e-4
2008	Crosby <i>et al.</i> [116]	Coal(bit.) 4	9.6	1980	170	1295	5.12	C	31.8 mm	0.032	1.05	2.0e-4
		Petcoke	6.3	2900	170	1295	5.12	C	31.8 mm	0.032	0.67	1.2e-4
	Wammack <i>et al.</i> [115]	BYU SEM	16.0	2500	220	1423	5.44	C	31.8 mm	0.032	4.52	6.5e-4
2007	Bons <i>et al.</i> [114]	Coal (bit.) 5	13.3	1980	200	1423	5.44	C	31.8 mm	0.032	2.47	3.6e-4
		Petcoke 2	33.0	2900	200	1423	5.44	C	31.8 mm	0.032	22.27	3.2e-3
		Straw	17.6	1680	200	1423	5.44	C	31.8 mm	0.032	3.34	5.3e-4
		Sawdust	19.7	960	200	1423	5.44	C	31.8 mm	0.032	2.39	3.8e-4
‘05	Jensen <i>et al.</i> [108]	BYU SEM	16.0	2500	220	1423	5.44	C	31.8 mm	0.032	4.52	6.5e-4
1992	Richards <i>et al.</i> [112]	Arkwright	20.0	1980	300	1373	5.32	C	12.7 mm	0.013	19.54	8.3e-4
		Blue Gem	20.0	1980	300	1373	5.32	C	12.7 mm	0.013	19.54	8.3e-4
		Arkwright 2	10.0	1980	300	1573	5.81	C	12.7 mm	0.013	4.47	1.9e-4
		Blue Gem 2	10.0	1980	300	1573	5.81	C	12.7 mm	0.013	4.47	1.9e-4
1990	Anderson <i>et al.</i> [111]	Arkwright	20.0	1980	300	1373	5.32	C	12.7 mm	0.013	19.54	8.3e-4
		Blue Gem	20.0	1980	300	1373	5.32	C	12.7 mm	0.013	19.54	8.3e-4
		Arkwright 2	10.0	1980	300	1573	5.81	C	12.7 mm	0.013	4.47	1.9e-4
		Blue Gem 2	10.0	1980	300	1573	5.81	C	12.7 mm	0.013	4.47	1.9e-4
	Wenglarz and Fox [132], [133]	Ash-fuel 1	10.2	1900	150	1313	5.17	C	(20 × 150) mm ⁺	0.035	0.90	2.1e-4
		Ash-fuel 2	8.5	1900	150	1313	5.17	C	(20 × 150) mm ⁺	0.035	0.63	1.5e-4
1989	Ahluwalia <i>et al.</i> [56]	Ash-fuel 3	14.5	1900	150	1313	5.17	C	(20 × 150) mm ⁺	0.035	1.83	4.3e-4
		Ash-fuel 1	10.2	1900	150	1313	5.17	C	(20 × 150) mm ⁺	0.035	0.90	2.1e-4
		Ash-fuel 2	8.5	1900	150	1313	5.17	C	(20 × 150) mm ⁺	0.035	0.63	1.5e-4
199	Ross <i>et al.</i> [110]	Arkwright3	20.0	1980	100	1450	5.51	C	8 mm	0.008	9.98	8.0e-4

		Kentucky	20.0	1980	100	1450	5.51	C	8 mm	0.008	9.98	8.0e-4
		Spring	20.0	1980	100	1450	5.51	C	8 mm	0.008	9.98	8.0e-4
		Montana	20.0	1980	100	1450	5.51	C	8 mm	0.008	9.98	8.0e-4
		North Dakota	20.0	1980	100	1450	5.51	C	8 mm	0.008	9.98	8.0e-4
1987	Spiro <i>et al.</i> [131]	AMAX	7.5	1900	100	1366	5.30	B	50 mm ⁺⁺	0.050	0.22	1.1e-4
		Otisca coal	5.8	1900	100	1366	5.30	B	50 mm ⁺⁺	0.050	0.13	6.6e-5
	Wenglarz [129]	Ash-fuel 1	10.2	1900	150	1313	5.17	C	(20 × 150) mm ⁺	0.035	0.90	2.1e-4
		Ash-fuel 2	8.5	1900	150	1313	5.17	C	(20 × 150) mm ⁺	0.035	0.63	1.5e-4
		Ash-fuel 3	14.5	1900	150	1313	5.17	C	(20 × 150) mm ⁺	0.035	1.83	4.3e-4
	Kimura <i>et al.</i> [130]	Otisca coal	5.8	1900	100	1366	5.30	B	50 mm ⁺⁺	0.050	0.13	6.6e-5
1984	Raj and Moskowitz [156]	Coal	3.0	1900	244	1283	5.09	B	16 mm	0.016	0.28	1.9e-5
		Pittsburg	7.0	2500	53	1590	5.85	C	8 mm	0.008	0.77	1.2e-4
	Anderson <i>et al.</i> [109]	Pittsburg 2	7.0	2500	149	1590	5.85	C	8 mm	0.008	2.17	1.2e-4
		Pittsburg 3	7.0	2500	215	1590	5.85	C	8 mm	0.008	3.13	1.2e-4
'83	Raj [155]	Coal 2	3.0	1900	244	1811	6.37	B	50 mm ⁺⁺	0.050	0.07	1.5e-5

⁺ Estimated by sketches and pictures

⁺⁺ Assumed as a representative chord of the first turbine section nozzle

Appendix C

In this Appendix, the molar fraction values for the materials collected in Tables 4 – 6 are reported. Since the correspondence of weight fraction and the molar fraction values are based on the specific chemical composition, Tables C1 – C3 complete the information of particle chemical composition used in the present work.

Table C1 – Molar fraction values divided according to by the deposition test (silty particles)

	Authors	Material	Na ₂ O	K ₂ O	CaO	MgO	SiO ₂	Al ₂ O ₃	TiO ₂	Fe ₂ O ₃
2017	Barker <i>et al.</i> [123]	ARD	0.024	0.023	0.044	0.021	0.794	0.069	0.002	0.022
	Boulanger <i>et al.</i> [124]	ARD 2	0.024	0.023	0.044	0.021	0.794	0.069	0.002	0.022
	Whitaker <i>et al.</i> [147]	ARD 3	0.024	0.023	0.044	0.021	0.794	0.069	0.002	0.022
2016	Boulanger <i>et al.</i> [122]	ARD 4	0.024	0.023	0.044	0.021	0.794	0.069	0.002	0.022
	Whitaker <i>et al.</i> [153]	ARD 5	0	0	0.037	0	0.893	0.061	0	0.008
	Lundgreen <i>et al.</i> [154]	ARD 6	0	0	0.034	0	0.896	0.062	0	0.008

Table C2 – Molar fraction values divided according to by the deposition test (volcanic particles)

	Authors	Material	Na ₂ O	K ₂ O	CaO	MgO	SiO ₂	Al ₂ O ₃	TiO ₂	Fe ₂ O ₃
'18	Naraparaju <i>et al.</i> [150]	EYJA	0.037	0.018	0.018	0.021	0.831	0.070	0.002	0.003
2017	Giehl <i>et al.</i> [145]	Basalt	0.033	0.004	0.122	0.098	0.582	0.086	0.024	0.052
		Andesite	0.039	0.005	0.105	0.092	0.598	0.122	0.009	0.031
		Dacite	0.050	0.018	0.046	0.014	0.739	0.092	0.007	0.034
		Rhyolite	0.066	0.016	0.033	0.016	0.777	0.074	0.007	0.011
	Wylie <i>et al.</i> [148]	EYJA 2	0.045	0.018	0.069	0	0.715	0.090	0.015	0.050
		Chaiten VA	0.044	0.020	0.019	0	0.817	0.091	0.002	0.007
2016	Dean <i>et al.</i> [144]	Laki	0.065	0.002	0.071	0.130	0.552	0.116	0.011	0.053
		Hekla	0.076	0.008	0.023	0.023	0.730	0.115	0	0.024
		Eldgja	0.071	0.002	0.070	0.112	0.536	0.124	0.019	0.065
		Askja	0.058	0.010	0.020	0.029	0.768	0.098	0	0.018
	Taltavull <i>et al.</i> [143]	Laki 2	0.013	0.001	0.091	0.049	0.512	0.074	0.030	0.229
		Laki 3	0.013	0.001	0.091	0.049	0.512	0.074	0.030	0.229
		Laki 4	0.013	0.001	0.091	0.049	0.512	0.074	0.030	0.229
'13	Shinozaki <i>et al.</i> [149]	Laki 5	0.013	0.001	0.091	0.049	0.512	0.074	0.030	0.229
'96	Dunn <i>et al.</i> [142]	St Helens	0.050	0.012	0.055	0.027	0.724	0.111	0.005	0.017
		Twin Mountain	0.006	0.033	0.139	0.027	0.613	0.095	0.017	0.070
'93	Kim <i>et al.</i> [141]	St Helens 2	0.050	0.012	0.055	0.027	0.724	0.111	0.005	0.017

Table C3 – Molar fraction values divided according to by the deposition test (coal particle)

	Authors	Material	Na ₂ O	K ₂ O	CaO	MgO	SiO ₂	Al ₂ O ₃	TiO ₂	Fe ₂ O ₃
'16	Laycock and Fletcher [121]	JBPS A	0.028	0.007	0.062	0.027	0.732	0.117	0.009	0.018
'15	Whitaker <i>et al.</i> [159]	JBPS B	0.044	0.013	0.123	0.031	0.611	0.083	0.028	0.067
'14	Prenter <i>et al.</i> [26]	JBPS B	0.044	0.013	0.123	0.031	0.611	0.083	0.028	0.067
'13	Casaday <i>et al.</i> [151]	JBPS B 2	0.044	0.013	0.123	0.031	0.611	0.083	0.028	0.067
	Laycock and Fletcher [120]	JBPP	0.044	0.012	0.123	0.031	0.612	0.083	0.028	0.067
2012	Webb <i>et al.</i> [12]	Lignite	0.009	0.007	0.388	0.061	0.375	0.096	0.022	0.042
		Bituminous	0.005	0.022	0.043	0.015	0.436	0.112	0.025	0.342
		PRB	0.019	0.004	0.503	0.115	0.246	0.069	0.018	0.026
		JBPS B 3	0.044	0.013	0.123	0.031	0.611	0.083	0.028	0.067
	Ai <i>et al.</i> [119]	Coal(bit.)	0.079	0.020	0.110	0.063	0.561	0.124	0.014	0.028
	Ai <i>et al.</i> [118]	Coal(bit.) 2	0.079	0.020	0.110	0.063	0.561	0.124	0.014	0.028
'11	Ai <i>et al.</i> [117]	Coal(bit.) 3	0.079	0.020	0.110	0.063	0.561	0.124	0.014	0.028
'10	Smith <i>et al.</i> [152]	Bituminous mean14	0.005	0.022	0.043	0.015	0.436	0.112	0.025	0.342
'00	Crosby <i>et al.</i> [116]	Coal(bit.) 4	0.079	0.020	0.110	0.063	0.561	0.124	0.014	0.028

		Petcoke	0.057	0.022	0.110	0.045	0.524	0.117	0.008	0.118
	Wammack <i>et al.</i> [115]	BYU SEM	0	0.054	0.170	0	0.698	0.031	0	0.047
2007	Bons <i>et al.</i> [114]	Coal (bit.) 5	0.079	0.020	0.110	0.063	0.561	0.124	0.014	0.028
		Petcoke 2	0.057	0.022	0.110	0.045	0.524	0.117	0.008	0.118
		Straw	0.021	0.186	0.104	0.047	0.605	0.013	0	0.023
		Sawdust	0.062	0.073	0.494	0.199	0.125	0.032	0.011	0.004
‘05	Jensen <i>et al.</i> [108]	BYU SEM	0	0.054	0.170	0	0.698	0.031	0	0.047
1992	Richards <i>et al.</i> [112]	Arkwright	0.011	0.010	0.080	0.024	0.620	0.190	0.012	0.053
		Blue Gem	0.027	0.006	0.135	0.066	0.302	0.240	0.026	0.199
		Arkwright 2	0.011	0.010	0.080	0.024	0.620	0.190	0.012	0.053
		Blue Gem 2	0.027	0.006	0.135	0.066	0.302	0.240	0.026	0.199
1990	Anderson <i>et al.</i> [111]	Arkwright	0.011	0.010	0.080	0.024	0.620	0.190	0.012	0.053
		Blue Gem	0.027	0.006	0.135	0.066	0.302	0.240	0.026	0.199
		Arkwright 2	0.011	0.010	0.080	0.024	0.620	0.190	0.012	0.053
		Blue Gem 2	0.027	0.006	0.135	0.066	0.302	0.240	0.026	0.199
	Wenglarz and Fox [132], [133]	Ash-fuel 1	0.016	0.022	0.120	0.001	0.352	0.246	0.018	0.225
		Ash-fuel 2	0.021	0.019	0.108	0.001	0.342	0.245	0.019	0.246
		Ash-fuel 3	0.032	0.018	0.169	0.002	0.250	0.215	0.025	0.290
1989	Ahluwalia <i>et al.</i> [56]	Ash-fuel 1	0.016	0.022	0.120	0.001	0.352	0.246	0.018	0.225
		Ash-fuel 2	0.021	0.019	0.108	0.001	0.342	0.245	0.019	0.246
		Ash-fuel 3	0.032	0.018	0.169	0.002	0.250	0.215	0.025	0.290
1988	Ross <i>et al.</i> [110]	Arkwright3	0.011	0.010	0.080	0.024	0.620	0.190	0.012	0.053
		Kentucky	0.143	0.003	0.022	0.014	0.394	0.145	0.090	0.188
		Spring Montana	0.158	0.001	0.354	0.121	0.232	0.099	0.012	0.022
		North Dakota	0.107	0.003	0.328	0.133	0.269	0.088	0.005	0.066
1987	Spiro <i>et al.</i> [131]	AMAX	0.119	0.068	0.064	0	0.0328	0.124	0.039	0.259
		Otisca coal	0.008	0.006	0.229	0	0.295	0.252	0.015	0.195
	Wenglarz [129]	Ash-fuel 1	0.016	0.022	0.120	0.001	0.352	0.246	0.018	0.225
		Ash-fuel 2	0.021	0.019	0.108	0.001	0.342	0.245	0.019	0.246
		Ash-fuel 3	0.032	0.018	0.169	0.002	0.250	0.215	0.025	0.290
	Kimura <i>et al.</i> [130]	Otisca coal	0.008	0.006	0.229	0	0.295	0.252	0.015	0.195
1984	Raj and Moskowitz [156]	Coal	0.034	0.028	0.005	0.026	0.459	0.275	0.020	0.153
		Pittsburg	0.011	0.010	0.080	0.024	0.620	0.190	0.012	0.053
	Anderson <i>et al.</i> [109]	Pittsburg 2	0.011	0.010	0.080	0.024	0.620	0.190	0.012	0.053
		Pittsburg 3	0.011	0.010	0.080	0.024	0.620	0.190	0.012	0.053
‘83	Raj [155]	Coal 2	0.034	0.028	0.005	0.026	0.459	0.275	0.020	0.153

2193
2194

Appendix D

In this Appendix, the data related to the particle viscosity are reported. Figure D1 and D2 show the viscosity-temperature trend, while in Table D1 – D3 the viscosity critical values are reported according to the viscosity model. Finally, in these tables, several data related to the source of contamination, typology, and material characteristics are also reported.

Figure D1 reports the variation of the particle viscosity as a function of the temperature, according to the NPL model. For a given temperature, the viscosity variation is almost six (6) orders of magnitude for lower temperatures and three (3) orders of magnitude for higher temperatures while the majority of the data is localized in the range of $(1 - 10^4)$ Pa s. Figure D1 reports the viscosity prediction according to the different models (S^2 [70], WF [71], S&T [72], RRLG [73], SDS [74] and GRD [75]). Each model is applied within its validity limits and, in order to highlight the differences, the viscosity prediction obtained with the NPL model are reported in red. Therefore, the shape and grey-scale color (empty with black bound, solid black and grey) represent the model predictions according to the chart label, while the red-scale (empty with red bound, solid red and pale red) represent the NPL predictions. Considering all predictions, the viscosity values vary in a sixteen-orders-of-magnitude-wide range. The trends are very similar to each other, even if the predictions provided by the WF model show a different trend. The values reported in Figure D2 and Figure D3, in conjunction with those reported in Figure 11 and Figure 12, represent the comprehensive analysis of the viscosity behavior of the considered particle materials.

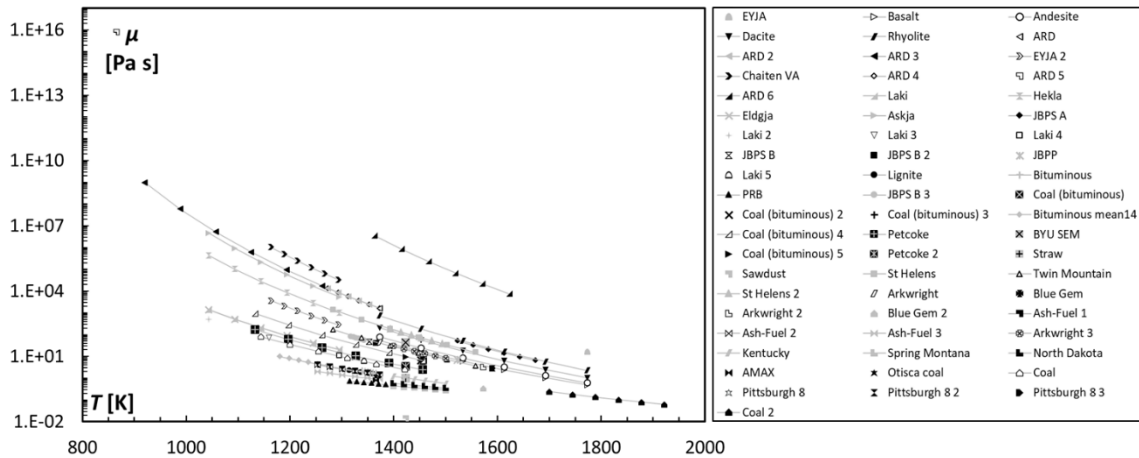


Figure D1 – Viscosity values as a function of the temperature calculated according to the NPL model

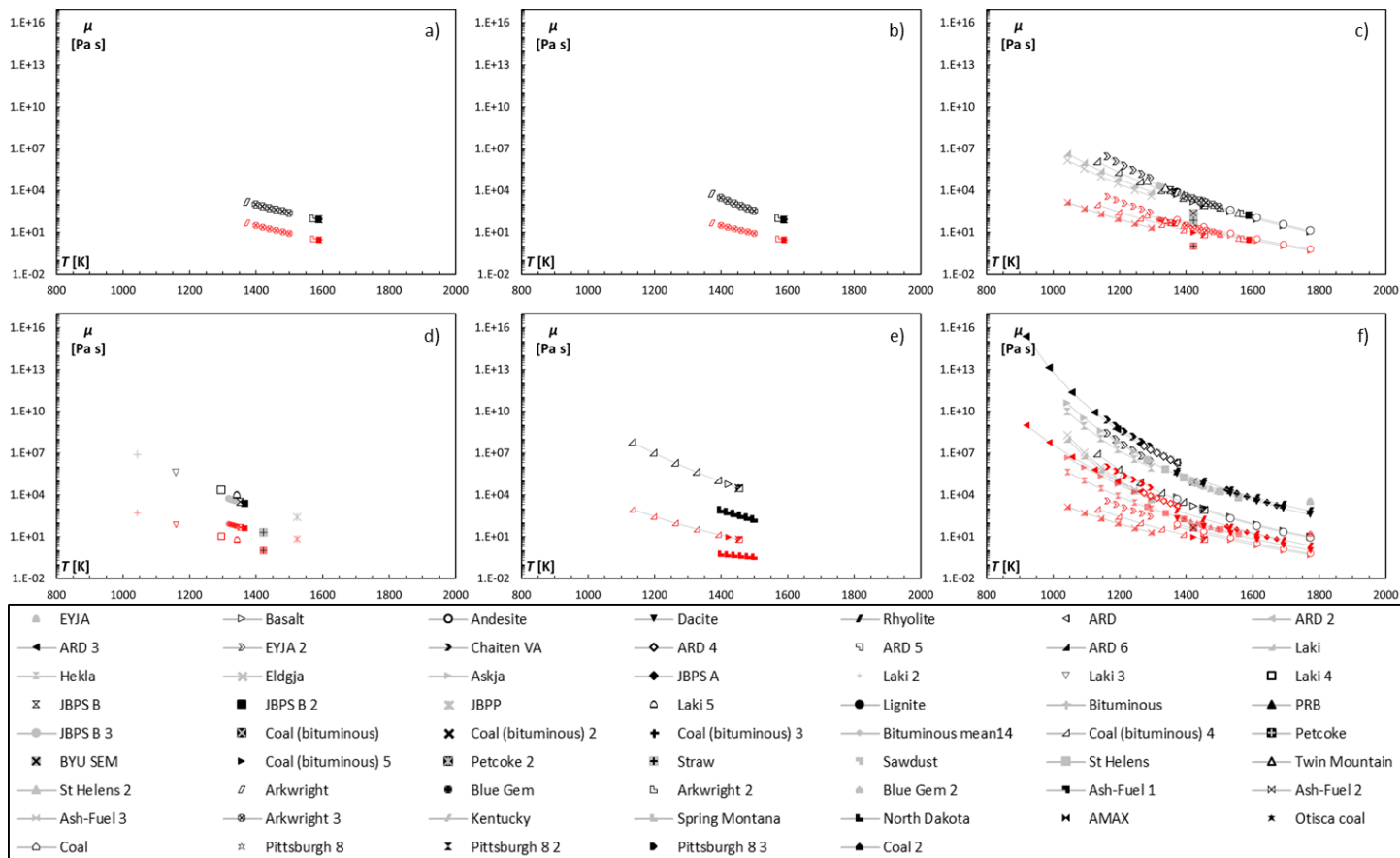


Figure D2 – Viscosity values as a function of the temperature: a) S^2 , b) WF, c) S&T, d) RRLG e) SDS and f) GRD

Table D1 – Critical viscosity values according to the viscosity model contaminant characteristics (silty particles)

Material	NPL	S^2	WF	S&T	RRLG	SDS	GRD	Source and preparation data
ARD, 2, 3, 4	3.32e3	-	-	-	-	-	5.04e6	Powder Technologies Inc.
ARD 5	1.88e5	-	-	-	-	-	-	Powder Technologies Inc.
ARD 6	2.12e5	-	-	-	-	-	-	Powder Technologies Inc.

Table D2 – Critical viscosity values according to the viscosity model contaminant characteristics (volcanic particles)

Material	NPL	S^2	WF	S&T	RRLG	SDS	GRD	Source and preparation data
EYJA	3.73e3	-	-	-	-	-	7.71e5	Volcanic ash collected (from ground) 4 km from the source
Basalt	1.92e3	-	-	6.03e5	-	1.49e7	4.25e6	Prepared from volcanic rock. Crystalline rock and homogenous glasses are specifically added
Andesite	5.76e2	-	-	9.76e4	-	3.65e6	1.09e5	Prepared from volcanic rock. Crystalline rock and homogenous glasses are specifically added
Dacite	1.02e3	-	-	-	-	-	3.32e6	Prepared from volcanic rock. Crystalline rock and homogenous glasses are specifically added
Rhyolite	5.73e2	-	-	-	-	-	3.44e5	Prepared from volcanic rock. Crystalline rock and homogenous glasses are specifically added
EYJA 2	2.29e2	-	-	5.67e4	-	-	1.96e6	Volcanic ash collected (from ground) sampled close to the source a couple of weeks after each eruption
Chaiten VA	1.28e3	-	-	-	-	-	6.26e5	Volcanic ash collected (from ground) sampled close to the source a couple of weeks after each eruption
Laki	3.45e1	-	-	1.65e4	-	-	1.20e4	Volcanic ash collected in the proximity of the eruption
Hekla	1.38e2	-	-	-	-	-	6.04e4	Volcanic ash collected in the proximity of the eruption
Eldgja	2.99e1	-	-	6.61e3	-	-	1.21e4	Volcanic ash collected in the proximity of the eruption
Askja	4.90e2	-	-	-	-	-	1.40e5	Volcanic ash collected in the proximity of the eruption

Laki 2, 3, 4, 5	1.09e2	-	-	-	7.24e5	-	-	Volcanic ash collected in the proximity of the eruption
St Helens, 2	6.37e2	-	-	-	-	-	9.90e5	Volcanic ash collected from ground
Twin Mountain	1.21e3	-	-	7.80e5	-	-	-	Volcanic ash collected from ground

Table D3 – Critical viscosity values according to the viscosity model contaminant characteristics (coal particle)

Material	NPL	S ²	WF	S&T	RRLG	SDS	GRD	Source and preparation data
JBPS A	1.44e3	-	-	-	-	-	2.52e6	Subbituminuos coal fly ash (collected from power plant)
JBPS B, 2, 3	6.76e2	-	-	4.05e5	5.05e4	-	-	Subbituminuos coal fly ash
JBPP	1.98e3	-	-	8.11e5	8.61e4	-	-	Subbituminuos coal fly ash
Lignite	5.46e1	-	-	-	-	-	-	Lignite ash
Bituminous	6.69e1	-	-	-	-	-	-	Bituminous coal fly ash
PRB	1.98e1	-	-	-	-	-	-	Subbituminuos coal fly ash
Coal(bit.), 2, 3, 4, 5	7.32e1	-	-	2.88e4	-	1.32e6	4.90e4	Subbituminuos coal fly ash
Bit. mean14	6.69e1	-	-	-	-	-	-	Bituminous coal fly ash
Petcoke, 2	1.05e2	-	-	-	-	-	-	Subbituminuos coal fly ash (blend of 55% petcoke and 45% coal)
BYU SEM	4.23e4	-	-	2.03e5	-	-	1.20e10	Atmosphere soot
Straw	6.11e0	-	-	1.66e3	1.97e2	-	-	Straw ash (collected biomass and burned/treated in a furnace)
Sawdust	1.95e-1	-	-	-	-	-	-	Sawdust ash (collected biomass and burned/treated in a furnace)
Arkwright, 2, 3	7.70e1	2.44e3	1.51e4	1.27e4	-	-	-	Bituminous ash coal (obtained after cobustion process of dry uncleaned coal with almost 7 percent ash)
Blue Gem, 2	6.84e0	-	-	-	-	-	-	Bituminous ash coal (obtained after cobustion process of dry cleaned coal with almost 0.56 % ash).
Ash-fuel 1	1.03e1	-	-	-	-	-	-	Coal fuel composition (before the combustion process)
Ash-fuel 2	1.03e1	-	-	-	-	-	-	Coal fuel composition (before the combustion process)
Ash-fuel 3	6.44e0	-	-	-	-	-	-	Coal fuel composition (before the combustion process)
Kentucky	1.14e1	-	-	-	-	-	-	Coal ash (obated after a combustion process inournace)
Spring Montana	3.67e0	-	-	-	-	-	-	Coal ash (obated after a combustion process inournace)
North Dakota	1.03e1	-	-	-	-	1.72e6	-	Coal ash (obated after a combustion process inournace)
AMAX	6.74e0	-	-	-	-	-	-	Coal ash (obtained from combustion of coal-water mixtures at 50 % and ash content of 0.8 %)
Otisca coal	6.18e0	-	-	-	-	-	-	Coal ash (obtained from combustion of coal-water mixtures at 50 % and ash content of 0.8 %)
Coal, 2	7.57e0	-	-	-	-	-	-	Fly ash removed from a coalfired boiler
Pittsburg, 2, 3	7.69e1	2.44e3	1.52e4	1.28e4	-	-	-	Coal ash